Master's thesis

NTNU
Norwegian University of Science and Technology
Faculty of Engineering
Department of Civil and Environmental Engineering

Khaled Damdam

A Combined Breakwater System

A Wave Attenuation Study on the Combination of Submerged and Floating Breakwaters using REEF3D

Master's thesis in Coastal and Marine Engineering and Management
Supervisor: Dr. Hans Bihs
August 2019

NTNU
Norwegian University of
Science and Technology

Khaled Damdam

A Combined Breakwater System

A Wave Attenuation Study on the Combination of Submerged and Floating Breakwaters using REEF3D

Master's thesis in Coastal and Marine Engineering and Management
Supervisor: Dr. Hans Bihs
August 2019

Norwegian University of Science and Technology
Faculty of Engineering
Department of Civil and Environmental Engineering

NTNU
Norwegian University of
Science and Technology

ERASMUS +: ERASMUS MUNDUS MOBILITY PROGRAMME

Master of Science in

COASTAL AND MARINE ENGINEERING AND MANAGEMENT

CoMEM

A COMBINED BREAKWATERS SYSTEM: A WAVE ATTENUATION STUDY ON THE COMBINATION OF SUBMERGED AND FLOATING BREAKWATERS USING REEF3D

Norwegian University of Science and Technology
11 August 2019

Khaled Damdam

The Erasmus+: Erasmus Mundus MSc in Coastal and Marine Engineering and Management is an integrated programme including mobility organized by five European partner institutions, coordinated by Norwegian University of Science and Technology (NTNU).

The joint study programme of 120 ECTS credits (two years full-time) has been obtained at two or three of the five CoMEM partner institutions:

- Norges Teknisk- Naturvitenskapelige Universitet (NTNU) Trondheim, Norway
- Technische Universiteit (TU) Delft, The Netherlands
- Universitat Politècnica de Catalunya (UPC). BarcelonaTech. Barcelona, Spain
- University of Southampton, Southampton, Great Britain
- City University London, London, Great Britain

During the first three semesters of the programme, students study at two or three different universities depending on their track of study. In the fourth and final semester an MSc project and thesis has to be completed. The two-year CoMEM programme leads to a multiple set of officially recognized MSc diploma certificates. These will be issued by the universities that have been attended by the student. The transcripts issued with the MSc Diploma Certificate of each university include grades/marks and credits for each subject.

Information regarding the CoMEM programme can be obtained from the programme coordinator:

Øivind A. Arntsen, Dr.ing.
Associate professor in Marine Civil Engineering
Department of Civil and Environmental Engineering
NTNU Norway
Mob.: +4792650455 Fax: + 4773597021
Email: oivind.arntsen@ntnu.no

CoMEM URL: https://www.ntnu.edu/studies/mscomem

CoMEM Thesis

This thesis was completed by:
Khaled Ahmed Ali Hag Damdam

Under supervision of:
Dr. Hans Bihs, Norwegian University of Science and Technology
Dr. Arun Kamath, Norwegian University of Science and Technology
Mr. Athul Sasikumar, Norconsult

As a requirement to attend the degree of
Erasmus+: Erasmus Mundus Master in Coastal and Marine Engineering and Management (CoMEM)

Taught at the following educational institutions:

Norges Teknisk- Naturvitenskapelige Universitet (NTNU)
Trondheim, Norway

Technische Universiteit (TU) Delft
Delft, The Netherlands

At which the student has studied from August 2017 to August 2019.

A Combined Breakwaters System: A Wave Attenuation Study on the Combination of Submerged and Floating Breakwaters using REEF3D

A Thesis
submitted to the Faculty of Civil Engineering
at the Norwegian University of Science and Technology
in partial fulfillment of the requirements for the degree of

Master of Science

by

Khaled Damdam

Abstract

Coastal zones have been a dynamic area and most favoured locations utilized for living, leisure, recreational activities, tourism, commerce and many other human activities. Submerged and floating breakwaters have been used as effective systems to protect these zones from wave attack. However, they are only effectively functional if the incident wave height is relatively low. Under such condition, these systems can reduce the wave transmission with signicant wave dissipation and hence achieving a desirable tranquillity in designated areas. Therefore, the focus of this research is mainly to investigate the possibility of using a combination of a submerged porous breakwater (SBW) with a floating breakwater (FBW) as an innovative coastal protection system that can provide adequate calm conditions in the coastal zones with minimum visual impact. This study utilizes the open-source CFD model, REEF3D to simulate such wave-structure interaction. This CFD model is based on the RANS equations coupled with the level set method and the $k-\omega$ turbulence model

In the present study, the first section deals with the simulation of irregular wave breaking over an irregular bed profile with the use of wave reconstruction method to generate irregular waves. An excellent agreement between the computed results and the experimental data is obtained showing that REEF3D model is capable of capturing the dominant features of the evolution of the wave breaking process, both in the shoaling region and the surf zone.

The second section deals with the simulation of regular wave interaction with the SBW. The simulation is conducted using the VRANS method to resolve the porous flow. The wave interaction with the SBW is validated by comparison with experimental data. An impressive agreement between the numerical results and the experimental data is achieved with very small RMSE values. Finally, the validated model is then used to simulate the combination of the SBW and the FBW. Three different cases are investigated with three different spacing between these structures. For each case, five different configurations related to the geometry of the FBW are simulated. It is found out that an effective reduction of more than 90%, on average, of the incident wave height, can be achieved for this combined breakwaters system.

This means that a transmission coefficient (K_t) of less than 10% is calculated across this combination. Besides, it is found out that 1.75 FBW length to wavelength (L/λ) ratio produces a very low transmission coefficient (K_t). Further, an effective distance of 1-2 wavelength between the SBW and the FBW subsystems can also result in lower transmission coefficients (K_t).

Acknowledgments

This thesis work is done according to the requirement as a graduate student in the two-year mobility Erasmus Mundus Masters Course: Coastal and Marine Engineering and Management (CoMEM).

First and foremost, I would like to thank God Almighty for giving me the strength, knowledge, ability and opportunity to undertake this wonderful program and to persevere and complete it satisfactorily.

First, I must express my very profound gratitude to my parents and especially to my wife, Viny for providing me with unfailing support and continuous encouragement throughout my years of study. I dedicate this thesis to her for her endless love and priceless support.

I would like to express my deep and sincere gratitude to my main supervisor, Dr.Hans Bihs for the opportunity he gave me to join his group and contribute to this exciting topic and to my co-supervisor Dr.Arun Kamath, for his technical advice, his patience, and the thoughtful support of my thesis work. I wish to extend my thanks to my other co-supervisor Athul Sasikumarl for all the assistance he provided during the execution of this thesis.

I would also like to express my sincere gratitude to Prof.Øivind Arnsten, Sonja Hammer and Dr.Raed Lubbad for their endless support through the two years of the COMEM MSc program. I would like to thank my CoMEM classmates for their support and most importantly, friendship throughout the last two years, to all the professors who have educated me during my two-year COMEM program at NTNU and TU Delft.

Last but not least, this master's thesis research was supported in part by computational resources provided by the Norwegian Metacenter for Computational Science, NOTUR under project number NN2620K.

Contents

List of Figures

Chapter 1

Introduction

1.1 General

Throughout history, coastal zones have been a dynamic area and most favoured locations utilized for living, leisure, recreational activities, tourism, commerce and many other human activities. These interfacial zones between land and sea have witnessed not only increasing population growth but also an extensive infrastructure and property development due to their prominent significance in terms of social, environmental and economic aspects. Therefore, coastal engineering plays an important role in both developing the coastal zone and protecting it .

Globally, breakwaters have been used as an effective system to protect a coastal zone from wave attack. It is mainly used to protect engineering structures and ships in a harbour area and/or reduce coastal erosion. Many configurations of the breakwater are used from the rubble-mound breakwater to hemispherical shape of artificial reefs and from emerged to submerged breakwaters [1]. Hence, the breakwaters have been undergoing a lot of changes from serving certain needs to facing sea level rise and to provide environmental-friendly solutions.

Around the world, most of the shore protection systems are Emerged Rubble Mound Breakwaters (RMBWs). These RMBWs are traditionally bottom-fixed structures that rest on the seabed with the crest rising above the mean sea level. They have armour layers made either from stones or concrete blocks. However, despite their efficiency in protecting coastal zones and their facilities, their inherent disadvantages such as high cost and low environmental and aesthetic aspects nearshore are often criticized. Therefore, there has been a worldwide interest in those aspects that leads to a preference of Submerged Breakwaters (SBWs) over the conventional breakwaters (RMBKs). This inclination towards employing submerged breakwaters in coastal zones stems from their advantages in fulfilling the protective function without spoiling the landscape, particularly in recreational and residential coastal developments [1]. Besides, these systems are excellent in enhancing water circulation between their lee side and seaside. This will maintain good water quality, reduce coastal erosion and preserve and enhance marine lives habitat. However, SBWs only partially attenuate the incident wave conditions which can be a disadvantageous especially if the absolute tranquillity is required, under extreme conditions, in crucial areas like harbour basins or a sanctuary for marine habitats. In addition, when the water depth becomes deep, the cost of the bottom-fixed breakwaters including SBWs and RBWs becomes high and the construction becomes difficult [2].

Under this scenario, Floating Breakwaters (FBWs) become a viable alternative and one of the key technologies of harbour construction projects around the world. In general, floating breakwater can be adapted in deep waters and to certain locations where a bed foundation is poor and water circulation is a strict requirement. However, FBWs cannot completely stop the incident wave height; instead, they attenuate the waves by partially dissipating, partially transmitting and partially reflecting. Therefore, FBWs can only reduce the wave transmission with adequate wave dissipation, transmission and reflection, if the incident wave is of a relatively low height.

1.2 Motivation

As described in the above section that each breakwater system has its advantages and disadvantages which are closely related to their site conditions. Further, a general deduction for the SBW system and the FBW system can be made as such; both systems are only effectively functional if the incident wave height is relatively low. Under such condition, these systems can reduce the wave transmission with signicant wave dissipation and hence achieving a desirable tranquillity in designated areas.

In modern times, coastal protection is faced with a lot of challenges and considerations under the pressure of the increased high-valued developments in coastal regions. Such challenges may include the environmental and in particular, the aesthetic value of the nearshore landscape. Therefore, new approaches to coastal protection employing innovative coastal protection systems that can provide adequate tranquil conditions in the coastal zones with minimum visual impact, are being researched and developed.

One of the innovative solutions is a combined system consisting of a submerged breakwater and a floating breakwater. Theoretical and experimental studies on wave interaction with submerged structures and wave interaction with floating breakwater have been carried out by many investigators. A review of some of these works can be found in [3] (for submerged breakwater) and [13] for the floating breakwaters.

To the best of the researchers' knowledge, very limited studies have been performed in such combination. In fact, only one experimental study by [4] has been investigated on such system. In this study, a floating breakwater consists of plastic pipes in combination with two submerged bars on the seaside. This study confirms the possibility of employing such a combination for shore protection. However, this study did not unravel some of the configurations of such combination such as the optimal distances between bars and floating breakwaters, size of bars and length of the floating breakwaters with respect to wavelength.

Unlike bars, breakwaters are mostly used on coastal zones for shore protection. A newly numerical study, conducted by kamath2018numerical using REEF3D, employed a combination of a submerged breakwater and floating breakwater. This study confirms the possibility of using such a system with a significant wave reduction behind the combined system. This current study is an extension for that study. In this study, however, many configurations will be used to determine the optimal configuration and spacing of such system using REEF3D, as well.

1.3 Objectives of the study

The main goal of this thesis is to utilize the open-source CFD model, REEF3D in order to simulate wave-structure interactions. This will be achieved by performing numerical simulations and validation for the following objectives:

- Validate the wave hydrodynamics in REEF3D by simulating the behaviour of irregular wave breaking on natural irregular topography with experimental data.
- Literature review on flow through porous media and implementation of VRANS in REEF3D
- Validate the wave interaction with a submerged porous breakwater with experimental data using REEF3D.
- The validated model of the objective 3 is used to simulate the wave interaction with a combination of a submerged porous breakwater and a floating breakwater.

1.4 Background

1.4.1 Porous Media: Literature review

1.4.1.1 Flow through porous media

Flow through a granular media such as sand, pebbles or stones is called porous flow. The presence of grains and voids within these granular materials act as resistance that leads to energy dissipation. Darcy (1856) and Forchheimer (1901) were the first to experimentally formulate a solution for flow in porous media [5]. The former derived ,through an experiment, a formulation that is only applicable for laminar flow (Eq. 1.1), while the latter introduced a formulation that combines laminar and turbulent flow by including friction terms [12] which, in turn, influenced by the Reynolds number (Re) as expressed in Eq. 1.2.

$$I = -au_f \tag{1.1}$$

$$I = -au_f + bu_f|u_f| \tag{1.2}$$

where, where I = hydraulic gradient; and a, b, and c are dimensional coefficients related to the porous flow.

In the classical Forchheimer equation (Eq. 1.2), a laminar part and a turbulent part can be discerned. Although the relation formulated by Forchheimer was based on experimental work, the flow in a porous medium can also be derived from the Navier-Stokes (NS) equations which are written in the Reynolds form in the x-direction [5] as follows:

$$\frac{\partial u}{\partial t} + u\frac{\partial u}{\partial x} + w\frac{\partial u}{\partial z} = -\frac{1}{p}\frac{\partial p}{\partial x} + v\frac{\partial^2 u}{\partial z^2} - \frac{\partial \overline{u'^2}}{\partial x} - \frac{\partial \overline{u'w'}}{\partial z} \tag{1.3}$$

inertia press. visc. Reynolds stresses

←-------------------------------→ ←---------------→

mean values turb. fluctuations

where, the LHS represents inertia terms (local and convective) and RHS contains pressure gradient, viscous shear and Reynolds stresses. Moreover, in order to reach a practical solution for the flow in a porous medium, an averaging procedure will be followed for each term to reach a practical solution. However, before averaging takes place, the real velocity (u) in the porous medium has to be substituted by an average velocity which can be expressed as:

$$u_f = \frac{1}{A}\int\int_A u dA = n.u \quad with \left(n = \frac{V_P}{V_T}\right) \tag{1.4}$$

This is average velocity is called filter velocity which is the actual pore velocity averaged over the pores as shown in Figure 1.1. In the above formulation, n is the porosity while u is the real velocity in the pores. The porosity (n) is usually defined as the pore volume, (V_P) divided by the total volume (V_T).

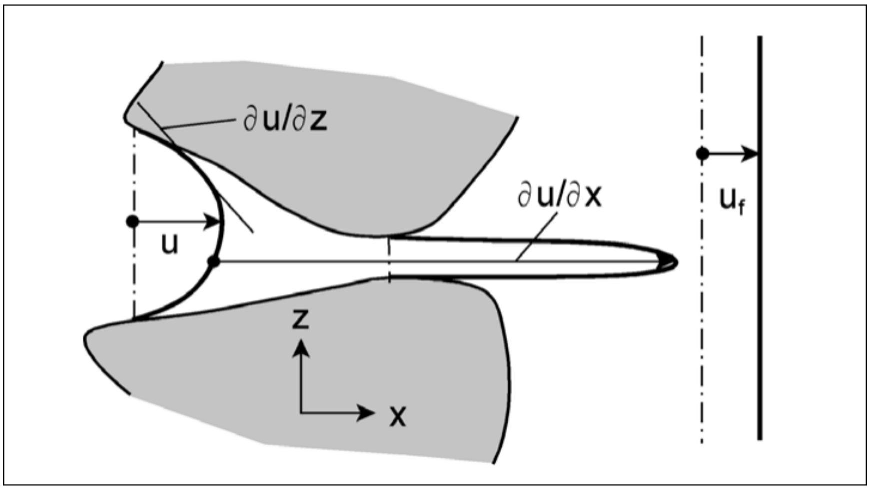

Figure 1.1: Velocities, gradients and averaging [5]

The second step, according to Van Gent (1993) [6], is to combine all square inertia and turbulence terms of the NS equations (Eq 1.3) in one quadratic friction term and to replace the (linear) viscous gradient with a linear friction term resulting in an extended Forchheimer equation formulated as:

$$I = au_f + bu_f|u_f| + c\frac{\partial u_f}{\partial t} \tag{1.5}$$

Where I hydraulic gradient, u_f filter velocity and a, b, and c are dimensional coefficients related to the porous flow [6]. In case of stationary flow, $(\frac{\partial u}{\partial t} = 0)$ then Eq. 1.5 reduces to the classical Forchheimer equation (Eq 1.2).

The first, a (s/m), and the second, b (s^2/m^2), terms in Eq. 1.5 represent the resistance coefficients derived theoretically by Van Gent (1993) [6] and are expressed by Eq. 1.6 and Eq. 1.7 as follows:

$$a = \alpha\frac{(1-n)^2}{n^3}\frac{\upsilon}{g(d_{n50})^2} \tag{1.6}$$

$$b = \beta\Big(1 + \frac{7.5}{KC}\Big)\frac{(1-n)}{n^3}\frac{1}{d_{n50}} \tag{1.7}$$

where d_{n50} is the grain diameter, KC is the Keulegan-Carpenter which is the ratio of the influence of the turbulent term and the influence of inertia, while the dimensionless coefficients α and β which are dependent on the grading, the shape of the grains, the Reynolds number and permeability have to be determined experimentally [5].

The third dimensional coefficient term (s^2/m) is also derived theoretically by Van Gent (1993) [6] which is applied only in case of local accelerations. In porous media, an extra momentum is needed in order to accelerate a certain volume of water compared to a non-porous medium [7]. The expression for c is given in Eq. 1.8:

$$c = \frac{1 + \gamma_F \frac{1-n}{n}}{g} \tag{1.8}$$

where γ_F is the nondimensional virtual mass coefficient. More details about these coefficients can be found in the experimental study by van Gent (1993) [6].

1.4.1.2 Numerical Modelling of Flow in Porous Media

In the last few decades, there has been extensive research on the idea of mathematically resolving the complexity of porous media flow by many coastal researchers [8]. As mentioned earlier that porous media has grains and voids that are characterized by irregular shapes and sizes. These characteristics make modelling of the flow through porous media highly complex. Nonetheless, almost all the existing approaches make use of the Navier-Stokes (NS) equations as their stepping point to simulate the flow through porous media. According to [8], all the different approaches can be categorized into two main groups namely microscopic and macroscopic.

The microscopic approach is a recent one that represents every physical element in the porous media. This detailed representation makes it quite challenging task in coastal engineering applications for several reasons: firstly, there is no technique to ease the use of the actual details of the internal geometry of the physical domain (i.e. rubble mound breakwater layers), secondly, from the computational resources point of view, meshing the whole physical domain is not possible, last but not least, understanding the mean behaviour of the flow in the porous media is more important in coastal engineering than resolving the real geometry of such medium in order to obtain an accurate solution at the pore scale [8].

The second approach, namely microscopic, is quite common as it deals with the concept of obtaining the mean flow behaviour and averaging their properties thus eliminating the need for the actual description of the internal geometry. Microscopic uses a set of spatially averaged Reynolds Averaged Navier Stokes (RANS) equations proposed by Jensen et al. (2014) [9]. The RANS equations formulated with the continuity equation (Eq. 1.9) and the momentum equation (Eq. 1.10) is first averaged based on the volume averaging theorem [10] as follows:

$$\frac{\partial u_i}{\partial x_i} \tag{1.9}$$

$$\frac{\partial \rho u_i}{\partial t} + \frac{\partial \rho u_i u_j}{\partial x_j} = \frac{\partial p}{x_i} + g_j x_j \frac{\partial p}{x_i} + \frac{\partial}{\partial x_i} \mu \left(\frac{\partial u_i}{\partial x_j} + \frac{\partial u_j}{\partial x_i} \right) \tag{1.10}$$

Before this averaging of RANS equations, the work by Sollitt and Cross (1972) [11] were the first to incorporate NS equations for gravity wave-induced flow in porous structures [8]. They also proposed the use of the seepage velocity concept instead of the actual one and they also split the instantaneous velocity into a volume-averaged seepage velocity, a temporal and a spatial perturbation as give by [9] in Eq. 1.11.

$$u_i = \left\langle \bar{u}^f \right\rangle + u' + u'' \tag{1.11}$$

With the volume- averaging approach, additional terms can be discerned in addition to the RANS equations resulting in a volume-averaged Reynolds-averaged Navier-Stokes (VRANS) form that is capable of solving the porous flow in the permeable coastal structures. For a more detailed and elaborate explanation of the mathematical derivation of the VRANS, the reader can refer to the studies of del Jesus et al. (2012) [12] and Jensen et al. (2014) [9].

1.4.1.3 VRANS (Volume Averaged Reynolds Averaged Navier-Stokes)

As mentioned earlier, the incompressible NS equations are the starting point for obtaining a set of equations that are able to model porous media. The hydrodynamic model of this study (REEF3D) uses the RANS equations (Eq. 1.9 and Eq. 1.10) which describes the conservation of mass and momentum, in a Volume-Averaged (VRANS) form that accounts for permeable coastal structures proposed by Jensen et al. (2014) [9].

To solve these set of equations (Eq. 1.9 and Eq. 1.10), the porous medium is first considered to be a continuous medium characterized by its macroscopic properties in order to eliminate the need for a detailed description of its complex internal geometry [8]. Then, Eq. 1.9 and Eq. 1.10 are averaged over a finite volume that is larger than the length scales of the pore size and much smaller than the scale of the spatial variation of the physical variables in the flow domain [9]. It is thus a spatial filter that results in the averaged flow behaviour inside porous zones. This averaged flow inside the pours medium result in a so-called filter velocity. This process is depicted in Figure 1.2.

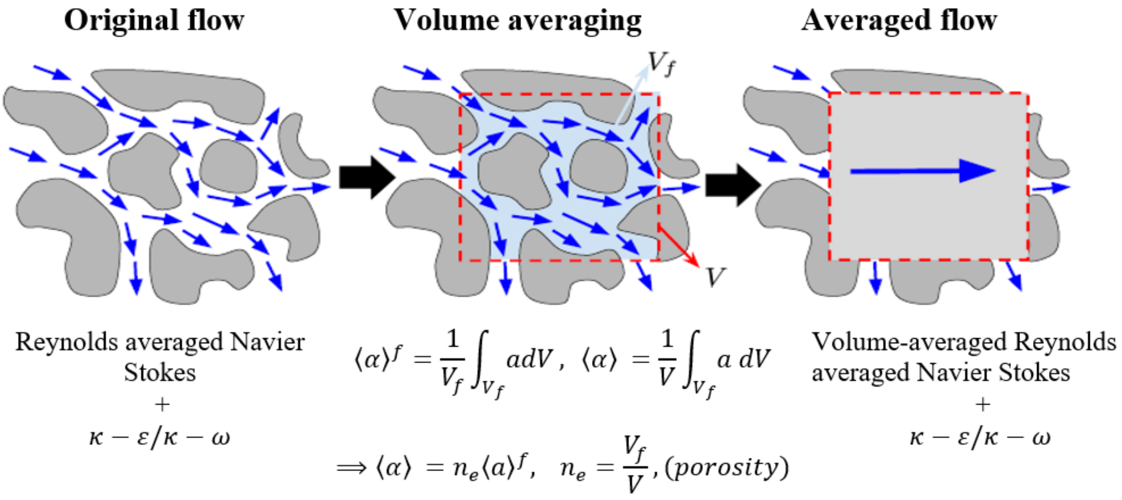

Figure 1.2: VRANS process for resolution of the porous flow [9]

As a result of this averaging, the VRANS equations obtained from the work of Jensen et al. (2014) [9] are presented as follows:

$$\frac{\partial \langle \bar{u}_i \rangle}{\partial x_i} \tag{1.12}$$

$$(1 + C_m) \frac{\partial}{\partial t} \frac{\rho \langle \bar{u}_i \rangle}{n} + \frac{1}{n} \frac{\partial}{\partial x_j} \frac{\partial \rho \bar{u}_i \bar{u}_j}{n} = - \frac{\partial \langle \bar{p} \rangle^f}{\partial x_j} + g_j x_j \frac{\partial \rho}{\partial x_i} + \frac{1}{n} \frac{\partial}{\partial x_j} \mu \left(\frac{\partial \bar{u}_i}{\partial x_j} + \frac{\partial \bar{u}_j}{\partial x_i} \right) + F_i \tag{1.13}$$

Where Eq. 1.12 represents the continuity equation with $\bar{u}_i$ as the volume averaged velocity over the total control volume, whereas Eq. 1.13 represents the formulation of the momentum equation that is based on the filter velocity. This filter velocity is divided by the porosity to correct for the use of filter velocity instead of the real pore velocity and thus correcting the momentum contributions.

Moreover, C_m in Eq. 1.13 is the added mass coefficient that account for the interaction between water and grains. This coefficient is formulated by Van Gent (1993) [6] as seen in Eq. 1.14. Furthermore the term F_i ,on the RHS, represents resistance force exerted by the porous media. This resisting force ,expressed by Eq. 1.15, is modeled by the extended Forchheimer equation (Eq. 1.5) discussed earlier. Here, a and b are the resistance coefficients and are defined and discussed earlier by Eq. 1.6 and Eq. 1.7.

$$C_m = \gamma_p \frac{1-n}{n} \tag{1.14}$$

$$F_i = -a\rho\langle\overline{u_i}\rangle - b\rho\sqrt{\langle\overline{u_j}\rangle\langle\overline{u_j}\rangle\langle\overline{u_i}\rangle} \tag{1.15}$$

1.5 Floating Breakwater: Literature Review

Historically, FBWs have been envisioned as wave attenuation structures that come with many types: rigid, flexible, porous, etc [13]. Their efficiency is often quantified by its transmission coefficients. Hence, the focus of all research is to obtain transmission coefficients that are as small as possible [13]. The transmission coefficient is defined ratio between the incident and transmitted wave height.

In literature, some researchers have concluded from various theoretical, experimental and numerical studies that FBWs are effective in attenuating waves by partially transmitting, partially reflecting, and partially dissipating the incident wave to an acceptable level in a limited wave frequency range [14]. However, FBWs are often criticized for their ineffectiveness in attenuating long waves [13]. This is due to the fact that their designs require a very large length to achieve a small wave transmission coefficient. This makes the construction cost uneconomical. Similarly, the FBWs system is prone to damage under severe wave conditions. Therefore, the application of FBWs is often limited to deep waters where short waves occur [13].

Technically, the FBW performance, in scenario of breakwater length much shorter than the incoming wavelength, is found to be ineffective in wave attenuation [13]. Therefore, the ratio of FBW length to wavelength (L/λ) is investigated. A common conclusion from all the previous studies is that the FBWs are only effective when the length in the wave direction (L) is greater than the wavelength (λ) [5]. According to Figure 1.3, larger L/λ ratio (i.e., > 2) is required to achieve small wave transmission coefficients behind the FBWs (i.e., $K_t < 0.5$) [5].

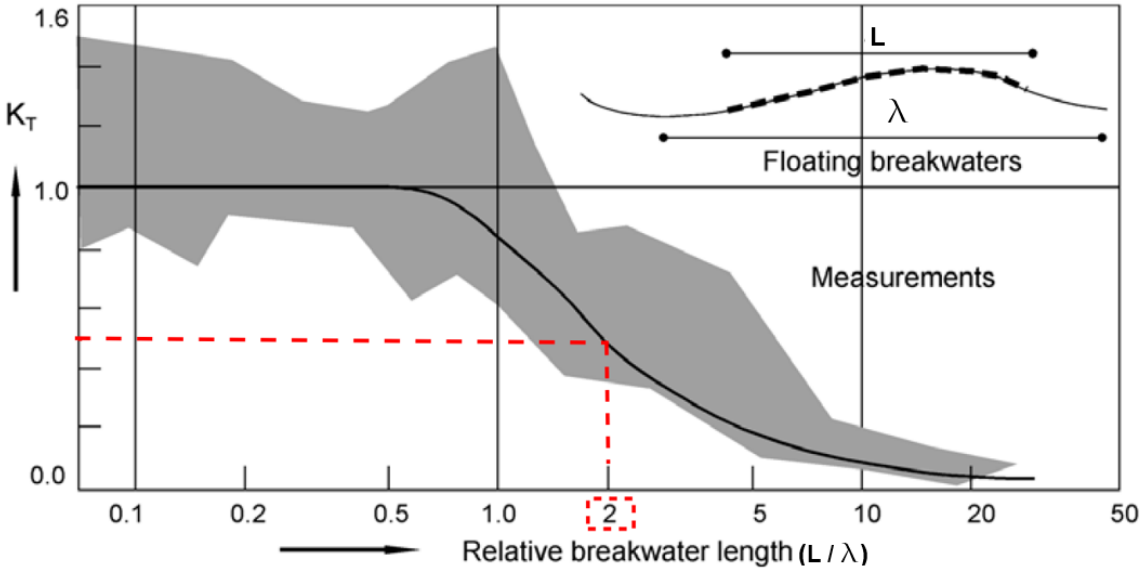

Figure 1.3: Transmission vs. relative floating breakwater length [5].

Chapter 2

Numerical Model and Wave Tank

2.1 Numerical Model

Increasing fluid problems in the field of coastal and marine engineering have encouraged the computational resources of organisation and companies to resolve the incredible large flow problems. The competition was done to develop a series of computational Fluid Dynamics (CFD) simulation with reasonable cost and high performance. The best common applied tools for engineering solutions, for fluid flows with or without solid interaction, is CFD.

REEF3D is an open-source CFD model developed at the Department of Civil and Environmental Engineering at NTNU that is used for a wide range of applications including the topic of wave-structure interactions. REEF3D has been previously used to study various problems in the field of hydraulic, ocean and offshore engineering such as wave decomposition [15], sloshing [16], pier scour [17], seawall scour [18], pipeline scour [19], extreme wave impact [20], irregular breaking wave forces [21], and submerged and floating coastal structures [22] [23] [24] [25] [10].

In the present study, REEF3D is used to investigate the behaviour of breaking waves and capturing their evolution over natural bed topography and man-made coastal structure. REEF3D is based on the RANS equations coupled with the level set method and the $k - \omega$ turbulence model [26]. In the following sections, the basic concepts of CFD and the computational methods applied in REEF3D are briefly described. Thus, for further information about this model, the reader can refer to [26].

2.1.1 Governing Equations

The incompressible fluid flow is described by the three-dimensional Reynolds-Averaged Navier–Stokes equations (RANS). These RANS equations are the most governing equations used for any CFD model. REEF3D model uses RANS equations that are solved together with the continuity equation (Eq. 2.1) to describe momentum and mass conservation and thus modelling the fluid flow accurately. The final form of the equations can be expressed as:

$$\frac{\partial u_i}{\partial x_i} = 0 \tag{2.1}$$

$$\frac{\partial u_i}{\partial t} + u_j \frac{\partial u_i}{\partial x_j} = -\frac{1}{\rho}\frac{\partial p}{\partial x_i} + \frac{\partial}{\partial x_j}\left[(\nu + \nu_t)\left(\frac{\partial u_i}{\partial x_j} + \frac{\partial u_j}{\partial x_i}\right)\right] + g_i \tag{2.2}$$

where, u is the velocity averaged over time t, ρ is the fluid density, p is the pressure, ν is the kinematic viscosity, ν_t is the eddy viscosity (often called viscosity by turbulent), g is the acceleration due to gravity and i, j indices refer to the three dimensions.

2.1.2 Discretization Method

The RANS equations are partial differential equations (PDEs). Analytically, most of the PDEs equations cannot be solved directly due to the due to non-linearity of coefficients, time-dependence of the coefficients or the higher-order of the equations. Therefore, numerical methods are used. Three numerical methods used to solve these PDEs namely: finite difference methods, finite volume methods and finite element methods.

The most common method used to solve partial differential equations is the finite element method which was first used by and [27] and [28]in the solid mechanics of the rigid bodies. The numerical model in this study uses this method with a high order temporal and spatial discretization. Finite volume method and finite difference method will not be used in this study and hence will not be further discussed.

REEF3D uses the finite difference method to solve the RANS equations. This numerical method allows the transition from a continuous representation to a set of discrete equations. This means that the domain is divided into points forming a grid. Then a linear combination of function values at grid points is used as an approximation for the PDEs. In REEF3D, a staggered Cartesian grid is used. This means that the unknown variables like velocity and pressure are located at different grid points and not at the same points. Using the staggered grid arrangement has been proven to be an efficient technique to avoid odd-even decoupling between the pressure and velocity and thus, leading to tight pressure-velocity coupling. Decoupling is referred to as a discretization error that can occur on collocated grids [29]. Three quantitative properties of the numerical solution need to be satisfied for applicability to a particular problem:

- Consistency: a finite difference method is consistent if the numerical scheme converges to the original PDE. It is often checked by a truncation error. A consistent scheme simply has a truncation error that vanishes as grid spacing and time step tend to zero. This means that $\Delta x, \Delta t \rightarrow 0$.
- Stability: a finite difference approximation is stable if the error caused by a small perturbation in the numerical solution remains bounded and does not diverge with time.
- Convergence: the solution of the finite difference equations should converge to the real solution of the PDEs for $\Delta x, \Delta t \rightarrow 0$. Convergence is checked by the consistency and stability of the numerical scheme and thus if the numerical scheme is consistent and stable then the scheme is convergent.

Besides, accuracy and computational efficiency are also important properties for the numerical solution. The former refers to a solution with not too much numerical damping thus the implementation of higher-order schemes ensures that the numerical solution will converge to the real solution. The latter, however, refers to the need of the numerical scheme to be computationally efficient and fast. Luckily, parallel computations are available and hence high efficiency of the scheme can be achieved.

2.1.3 Convective Discretization

The RANS equation mentioned in section 2.1.1 consist of the convective terms that need to be discretized before solving the equation. In literature, there are several discretization schemes using finite dierence method which can be implemented in REEF3D. However, in this study, the RANS equation and the requirements in section 2.1.2 are satised by the implementation of the fifth-order Weighted Essentially Non-Oscillatory Scheme (WENO) [30] in the conservative finite difference framework for the convection discretization of the flow velocities and by the Hamilton-Jacobi version of the WENO scheme for the level set function ϕ (see section 2.2) [31]. This method is proved to be capable of producing a stable calculation with minimum risk and thus achieving robust solutions in complex smooth regions or with strong discontinuities. The convection term is approximated in x-direction as follows:

$$u_i \frac{\partial u_i}{\partial x_i} \approx \frac{1}{\Delta x}\left(\bar{u}_{i+1/2}\, u_{i+1/2} \; - \; \bar{u}_{i-1/2}\, u_{i-1/2}\right) \tag{2.3}$$

where $\bar{u}$ is the convection velocity that is obtained at the cell faces through simple interpolation. Subscript $i + 1/2, i - 1/2$ represent the cell faces and $u_{i+1/2}$ is reconstructed with the WENO scheme based on the weighted sum of three Essentially Non-Oscillatory (ENO) stencils:

$$U^{\pm}_{i+1/2} = w_1^{\pm} U^{1\pm}_{i+1/2} + w_2^{\pm} U^{2\pm}_{i+1/2} + w_3^{\pm} U^{3\pm}_{i+1/2} \tag{2.4}$$

where ± sign indicates the upwind direction, while U^1, U^2 and U^3 represent the three possible ENO stencils. For the upwind direction in the positive i-direction is given by the following expressions:

$$\begin{aligned} U^{1\pm}_{i+1/2} &= \frac{1}{3}u_{i-2} - \frac{6}{7}u_{i-1} + \frac{11}{6}u_i \\ U^{2\pm}_{i+1/2} &= -\frac{1}{6}u_{i-1} + \frac{5}{6}u_i + \frac{1}{3}u_{i+1} \\ U^{3\pm}_{i+1/2} &= -\frac{1}{3}u_i + \frac{5}{6}u_{i+1} - \frac{1}{6}u_{i+2} \end{aligned} \tag{2.5}$$

For each ENO stencil, the non-linear weights $w_n^{\pm}$ is measured based on the smoothness indicators IS [30] [31]. The WENO stencil with the smoothest solution will be assigned the largest weight w_n. For stencils with larger gradients, the weights will be smaller. Thus, the WENO scheme is able to handle large gradients right up to the shock with high accuracy. In the worst case, the accuracy will be of the third order. However, for a smooth solution, the WENO scheme delivers 5th-order accurate results. Further, the WENO scheme does not smear out gradients and maintain its sharpness.

2.1.4 Time Discretization and Adaptive Time stepping

For the time discretization, REEF3D has different schemes including Adams-Bashforth, second, third and fourth-order Total Variation Diminishing (TVD) Runge-Kutta. In this study, the third Order Total Variance Diminishing (TVD) Runge Kutta Scheme is implemented. This scheme consists of three Eularian steps (see Eq. 2.6) which are widely used for the momentum equations, level set function and all the transport equations. Considering a generic variable ϕ, the equations of the third-order Runge-Kutta scheme as given by [32] are expressed as:

$$\begin{aligned}\phi^{(1)} &= \phi^n + \Delta t L(\phi^n)\\ \phi^{(2)} &= \frac{3}{4}\phi^n + \frac{1}{4}\phi^{(1)} + \Delta t L(\phi^{(1)})\\ \phi^{n+1} &= \frac{1}{3}\phi^n + \frac{2}{3}\phi^{(2)} + \Delta t L(\phi^{(2)})\end{aligned} \tag{2.6}$$

This scheme diminishes spurious oscillations by suppressing the local extrema [33]. Also, this scheme expresses good numerical stability for the CFL values lesser than one [32]. Therefore, in order to maintain the numerical stability of this scheme, an adaptive time stepping approach is implemented and is expressed as:

$$\Delta t \leq 2\left(\left(\frac{|u|_{max}}{dx} + D\right) + \sqrt{\left(\frac{|u|_{max}}{dx} + D\right)^2 + \frac{4\,|S_{max}|}{dx}}\right)^{-1} \tag{2.7}$$

This CFL condition was proposed by [34] where the D term defines the contribution to the diffusion and is expressed as follows:

$$D = max(\nu + \nu_t)\left(\frac{2}{(dx)^2} + \frac{2}{(dy)^2} + \frac{2}{(dz)^2}\right) \tag{2.8}$$

where v_t is the turbulent viscosity, v kinematic viscosity, dx, dy and are the magnitudes of the spatial discretization units.

The current numerical model has been removed from CFL, and the diusion part of the RANS equation is treated implicitly. Therefore, TVD Runge−Kutta scheme is used for all transport equations except the turbulence model in REEF3D.

2.1.5 Turbulence Model

The RANS equation (2.2) that is implemented in REEF3D includes the eddy viscosity or viscosity by turbulent term. This turbulent eddy viscosity ν_t in the RANS equations is determined using the two-equation $k-\omega$ model proposed by [35]. These two equations are based on energy transport equations and they are referred to as transport equations. The first equation is the turbulent kinetic energy (k) , while the second equation is the specific turbulent dissipation (ω). Their solutions are found by solving the following equations:

$$\frac{\partial k}{\partial t} + u_j\frac{\partial k}{\partial x_j} = \frac{\partial}{\partial x_j}\left(\left(\nu + \frac{\nu_t}{\sigma_k}\right)\frac{\partial k}{\partial x_j}\right) + P_k - \beta_k k\omega \tag{2.9}$$

$$\frac{\partial \omega}{\partial t} + u_j \frac{\partial \omega}{\partial x_j} = \frac{\partial}{\partial x_j} \left[\left(\nu + \frac{\nu_t}{\sigma_\omega} \right) \frac{\partial \omega}{\partial x_j} \right] + \frac{\omega}{k} \alpha P_k - \beta \omega^2 \tag{2.10}$$

where P_k is the turbulent production rate, while the closure coefficients are: $\sigma_k = 2$, $\sigma_\omega = 2$, $\alpha = 5/9$, $\beta_k = 0.09$ and $\beta = 3/40$.

The turbulent eddy viscosity ν_t in the RANS equations is mostly controlled by the Eq. 2.11 to avoid excessive turbulence beyond the boundary layer in a highly strained [36]. The limiting equation is expressed as:

$$\nu_t = min \left(\frac{k}{\omega}, \sqrt{\frac{2}{3}} \frac{k}{|S|} \right) \tag{2.11}$$

where $|S|$ is the mean strain rate. In the oscillatory wave motion, the rate of strain (S) can be large around the interface between water and air in a numerical wave tank. In this case, the eddy viscosity limiter in Eq. 2.11 is not effective and hence additional turbulent damping at the free surface is required. The specific turbulent dissipation, given by [37], is given by the following expression:

$$\omega_s = \frac{C_\mu^{-\frac{1}{4}}}{k} k^{1/2} . \left(\frac{1}{y'} + \frac{1}{y^*} \right) \tag{2.12}$$

where $c\mu = 0.07$ and $k = 0.4$ are constants. y' stands for the turbulent length scale and it is being empirically found to be 0.07 times the mean water depth [37], while y^* represents the distance from the nearest wall to ensure a smooth transition to the wall value of ω. Finally, the specific turbulent dissipation term ω_s is activated around the interface of thickness ϵ by multiplying it with the Dirac delta function $\delta t(\phi)$ as follows:

$$\delta t(\phi) = \begin{cases} \frac{1}{2\epsilon} \left(1 + cos \left(\frac{\pi \phi}{\epsilon} \right) \right) & if\ |\phi| < \epsilon \\ 0 & else \end{cases} \tag{2.13}$$

2.1.6 Solution to Navier-Stokes equation

Besides space and time discretization, the non-hydrostatic pressure term must be fully obtained in order to obtain a complete solution for RANS equations present in Eq. 1.9. The direct solution for this term is not possible because of the involvement of nonlinear terms which make the solution computationally very expensive and thus implicit methods need to be used. In that regard, REEF3D offers different solvers for the pressure including Pressure implicit with the split operator (PISO), Semi Implicit Method for Pressure Linked Equation (SIMPLE) and Projection Method (PJM).

PJM which was developed by Chorin [36] is the most commonly used of the three methods presented. Therefore, this method is adopted in this thesis. The idea behind this method is that the velocity and pressure fields are separated. firstly, the momentum equation is solved with an intermediate velocity field u_i^*ignoring the pressure term as such:

$$\frac{\partial u_i^*}{\partial t} + u_j^n \frac{\partial u_i^n}{\partial x_j} = \frac{\partial}{\partial x_j} \left[(\nu + \nu_t) \left(\frac{\partial u_i^n}{\partial x_j} + \frac{\partial u_j^n}{\partial x_i} \right) \right] + g_i \tag{2.14}$$

The intermediate velocity field u_i^* does not satisfy the continuity equation. So, the second step is to use the projection step where u_i^* is corrected to obtain the solution of the time-step u_i^{n+1} with the pressure term added:

$$u_i^{n+1} = u_i^* - \frac{\Delta t}{\rho(\phi^n)} \frac{\partial p^{n+1}}{\partial x_i} \tag{2.15}$$

the pressure term in the above equation (p^{n+1}) is unknown. To solve this, the divergence operator (u_i^{n+1}) in Eq. 2.15 should be zero. This results in an equation called Poisson pressure equation:

$$\frac{\partial}{\partial x_i} \left(\frac{1}{\rho(\phi^n)} \frac{\partial p^{n+1}}{\partial x_i} \right) = \frac{1}{\Delta t} \frac{\partial u_i^*}{\partial x_i} \tag{2.16}$$

For this present study, Poisson pressure equation is solved, in REEF3D, using the iterative Bi Conjugate Gradient Stabilized (BiCGstab) method from the HYPRE solver library which contains high-performance preconditioners for solutions of large and sparse linear systems on parallel computers [38]. BiCGstab algorithm is developed by van der Vorst (1992) [39] and it ensures a faster convergence with a fast and scalable solution to the Poisson equation.

2.2 Free Surface Model

The most challenging task for engineering on fluid dynamics is solving the interface between two different fluid interfaces (i.g. air and water). This is because of the large difference in densities. Therefore, the free surface should be modelled to track the flow between two phases water and air. There are several methods such as Marker and cell approach (MAC), Volume of fluid (VOF) method, particle level set method, and level set method (LSM), have been developed to solve the problem of the interface between between two different media.

The free surface treatment in REEF3D is obtained with the level set method with an Eulerian approach [26]. In this method, the level set function gives the closest distance to the interface Γ where each face is identified with a different sign according to the following expressions:

$$\phi(\vec{x},t)\begin{cases} >0 & \text{if } \vec{x} \in phase\ 1 \\ =0 & \text{if } \vec{x} \in \Gamma \\ <0 & \text{if } \vec{x} \in phase\ 2 \end{cases} \tag{2.17}$$

When the level set function evolves during its convection, it could misplace its signed distance property. To avoid this problem, the function is reinitialized at the beginning of each time step. The reinitialization is based on the following PDE [40]:

$$\frac{\partial \phi}{\partial t} + S(\phi)\left(\left|\frac{\partial \phi}{\partial x_j}\right| - 1\right) = 0 \tag{2.18}$$

where $S(\phi)$is the smooth signed function by [41] as such:

$$S(\phi) = \frac{\phi}{\sqrt{\phi^2 + \left|\frac{\partial \phi}{\partial x_j}\right|^2 \Delta x^2}} \tag{2.19}$$

2.3 Numerical Wave Tank

Computational Fluid Dynamics (CFD) normally uses Numerical Wave Tank (NWT) to study the propagation of waves, wave kinematics and forces. However, the results from the NWT can only be a viable engineering source if they are validated experimentally for each wave phenomenon such as regular waves, irregular breaking waves, breaking waves, wave-structure interactions, etc. With the advanced computing capabilities with supercomputers nowadays, there is a rapid growth in the availability and capabilities of numerical wave tank models. Many methods are used in the numerical wave tank set-up including RANS with VOF approach, and RANS with the level set method (LSM) and RANS with Potential theory.

In this study, RANS (see section 2.1.1) with LSM (see section 2.2) is used in the open-source CFD model,REEF3D, which have been thoroughly discussed in the previous sections. The spatial domain in the NWT is divided into three zones: the wave generation zone, the wave tank and the numerical beach zone (see Fig 2.1). Furthermore, the numerical wave tank consists of 6 boundaries: inlet, outlet, atmosphere, bottom and front and back. In the following sections, Wave Generation and Absorption methods and Wave Theories that are used in this study are briefly discussed.

2.3.1 Wave Generation and Absorption

NWT is an essential part of a numerical model which is established with a wave generation, on the left boundary, a wave absorption zone, on the right boundary and working zone as shown in Figure 2.1. REEF3D implements various wave types following different wave theories such as small-amplitude wave, Stokes, Cnoidal, solitary, irregular and focused waves with different orders and also newly developed technique for the irregular waves called wave reconstruction method [42].

During this study, two waves types are used namely irregular waves and 5th order Stokes waves in which they are respectively imposed by mainly two methods; Dirichlet and Relaxation Methods. According to [26], both relaxation methods dissipate the wave energy by ramping the free surface down to the still water level, the velocity to the zero and the pressure to its hydrostatic still water conditions. Moreover, the length of the dissipating zone should be in order of two wavelengths. Meanwhile, the Active Wave Absorption avoids reflections by generating a wave opposite of the reflected wave, thus cancelling it out.

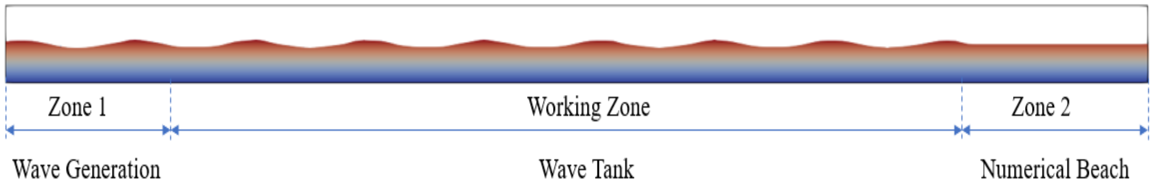

Figure 2.1: Numerical wave tank with wave generation (zone 1), wave tank (working zone) and absorption zone (zone 2/numerical beach).

2.3.2 Dirichlet Method

Dirichlet method generate waves in the inflow boundary by assigning fixed values for the free surface and the velocity. This method is the simplest, fastest and the first to be used in most models. However, it does not produce the highest quality waves due to the periodically changes of the motion of the free surface and the flow direction [26].

2.3.3 Relaxation Method

As mentioned earlier, there are three zones in NWT. The first zone (zone 1) includes the place where the waves are generated. The wave tank is the second zone. The waves of the second zone are dissipated with a numerical beach (zone 2). The generated waves using the relaxation method are moderated after every time step with analytical solutions and variables from the simulation [43]. The relaxation method in zone 1 is obtained using following expressions for pressure and velocity as such:

$$\begin{aligned} u_{relaxed} &= \Gamma(x)u_{analytical} + (1-\Gamma(x))u_{computational} \\ p_{relaxed} &= \Gamma(x)p_{analytical} + (1-\Gamma(x))p_{computational} \end{aligned} \tag{2.20}$$

In Wave generation zone, the computational values of horizontal and vertical velocity and the free surface are ramped up to the analytical values expected by the wave theory [26]. However, in the wave absorption zone, the computational values for the horizontal and vertical velocity and the free surface are gradually brought to zero and all the energy is dissipated to still water conditions [26]. The following expressions in zone 2 are obtained for pressure and velocity as such:

$$\begin{aligned} u_{relaxed} &= \Gamma(x)u_{computational} + (1-\Gamma(x))u_{analytical} \\ p_{relaxed} &= \Gamma(x)p_{computational} + (1-\Gamma(x))p_{analytical} \end{aligned} \tag{2.21}$$

2.3.4 Wave Reconstruction Method

In the numerical simulation, reproducing the time history of free surface elevation for irregular waves is still a challenging task. Irregular waves are generated based on the spectral parameters such as H_s, T_p ,either in a laboratory or field experiment. In most of the numerical models, these parameters are used as an input in the inlet boundary in order to mimic the experimental measurements. The results of the numerical models is required to be validated with experimental data in order to use them reliably for real-world applications.

In terms of energy spectra, the spectral parameters used as inputs in the numerical model will allow for a comparison of the energy spectra between the numerical and experimental over distance and time. However, a comparison of the free surface elevation time history is not possible. This is due to the randomness of these generated waves.

Therefore, the idea of the wave reconstruction method [42] is to enable the numerical model to generate irregular random waves which are exactly similar to those waves generated for instance in the wave board in a laboratory experiment, using decomposition technique. This technique decomposes the time series from an experimental data into its Fourier components so that phase, frequency and amplitude information is known. Therefore, this method enables the numerically reconstructed irregular free surface elevations during the wave transformation to be compared to the experimental data.

This reconstruction method coupled with Dirichlet inlet boundary condition is used in this study (see chapter 3). For more more information about this method, the reader can refer to [42].

2.4 Wave Types

2.4.1 Irregular Waves

Waves in nature, especially wind-generated waves, are not small in amplitude and show irregular character. Irregular character means that waves do not repeat themselves periodically in time and space with respect to wave height (H) and wave periods (T). When an irregular water surface elevation is measured, the resulting signal will be a random wave signal which can be thought of as being generated as the sum of many sinusoidal waves with different amplitudes, frequencies, and phases. This oscillatory random surface elevation can be formulated as Fourier series as follows:

$$\underline{\eta}(t) = \sum_{i=1}^{N} \underline{a_i}\ cos(2\pi f_i t + \underline{\alpha_i}) \tag{2.22}$$

where where $\underline{\eta}$ is the free surface elevation, N large number of frequencies, $underlinea_i$ wave amplitude, f_i wave frequency, and $\underline{\alpha_i}$ wave phase that belong to each component i. The underscores indicate that the variables are random. This approach is called the random phase/amplitude model [44]. The benefit of this model is that the wave spectral energy density can be constructed via Fourier analysis under the assumption that the surface elevation can be seen as a stationary Gaussian process. The reason of using the spectral energy density over the amplitude is because it gives a complete description of the surface elevation of waves in a statistical sense [44]. In a more mathematical way, spectral energy density can be expressed as a function of frequency $E(f)$ as follows:

$$E(f) = \lim_{\Delta f \to 0} \frac{1}{\Delta f} E\left\{ \frac{1}{2} \underline{a_i}^2 \right\} \tag{2.23}$$

where $\underline{a}$ is the amplitude of a harmonic component and Δf_i is the width of a random frequency interval. When the width of the frequency interval Δf_i approaches zero, a continuous distribution of the variance over the frequency interval is obtained. This distribution is known as the spectral energy density or variance density spectrum as shown in Eq. 2.23.

In coastal water, the nearshore wave transformation of the irregular waves including breaking can be very complex. This is due to the presences of the nonlinearities in the wave field [45]. Wave deformation including wave breaking in this region is preferably treated using individual wave analysis rather than spectral analysis described above [45]. This is due to the fact that the wave components in the frequency bandwidth do not break, while the real individual waves break in the time domain.

Zero-crossing method is a very well-known method that is used in the individual wave analysis to obtain individual wave heights and periods. Two types of zero-crossing can be distinguished: upward zero-crossings and downward zero-crossings. The latter is the most relevant for the breaking process. This is because the steep front of the wave during breaking is is included in the definition with downward crossings [44]. Figure 3 illustrates the wave height and wave period given by the definition of zero-down crossing method. After defining the individual waves of a wave record, breaking parameters can be obtained. Based on experimental studies, various formulas has been introduced and it is concluded that the individual waves of the irregular type breaks earlier than individual waves of a regular type with similar properties.

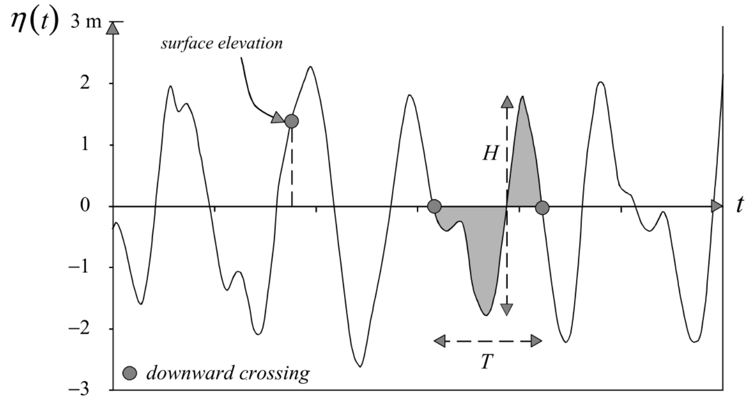

Figure 2.2: Wave height (H) and wave period (T) definition of the irregular surface elevation using the wave downward zero-crossings method [44].

Several formulas were proposed based on experimental studies and it was found that the individual waves composing the irregular wave breaks more easily earlier than a similar regular wave with the same properties [46].

In chapter 3, irregular waves is imposed in the REEF3D model using the reconstruction method (section 2.3.4) to simulate their behaviour and compare it with experimental data.

2.4.2 Fifth-Order Stokes Wave

When the waves are too steep or the water is too shallow, the linear wave theory is no longer valid and the spectrum no longer provides a complete statistical and physical description of the waves [44]. The degree of nonlinearity of waves is often determined by the Ursell number N_{Ursell}, which combines wave steepness and relative water depth as follows:

$$N_{Ursell} = \frac{H\lambda^2}{d^3} \tag{2.24}$$

where H is wave height, λ is wavelength and d water depth.

In classical nonlinear wave theories, each wave is treated individually and independently with a constant shape, amplitude and length [44]. Stokes (1847) was the first to develop a second-order approximation for waves of a finite height. Stokes's theory is limited to deep waters and some range of intermediate waters. Therefore, when the wave height increases, higher-order approximations are required in order to obtain a good representation of the waves.

In this study, a fifth-order Stokes wave is used. The analytical solution of this theory was developed by Fenton (1985)[47]. The Taylor expansion with the perturbation factor ($\pi H/\lambda$) is evaluated until the fifth power.According to this theory, relations for η, Φ, u, w are given by the following formulations:

$$\eta = \frac{1}{k}\sum_{n=1}^{5} \epsilon^n b_n \cos(n\theta) \tag{2.25}$$

in which:

$$\begin{aligned} b_1 &= 1 + \epsilon^2 B_{31} - \epsilon^4 (B_{53} + B_{55}) \\ b_2 &= B_{22} + \epsilon^2 B_{42} \\ b_3 &= -B_{31} + \epsilon^2 B_{53} \\ b_4 &= B_{44} \\ b_5 &= B_{55} \end{aligned} \tag{2.26}$$

$$\Phi = C_0\sqrt{\frac{g}{k^3}}\sum_{n=1}^{5}\epsilon^n a^n \cosh(nkz)\sin(n\theta) \tag{2.27}$$

in which:

$$\begin{aligned} a_1 &= A_1 + \epsilon^2 A_{31} + \epsilon^4 A_{51} \\ a_2 &= A_{22} + \epsilon^2 A_{42} \\ a_3 &= A_{33} + \epsilon^2 A_{53} \\ a_4 &= A_{44} \\ a_5 &= A_{55} \end{aligned} \tag{2.28}$$

$$u = C_0\sqrt{\frac{g}{k}}\sum_{n=1}^{5}\epsilon^n \; n \; a_n \cosh(nkz)\cos(n\theta) \tag{2.29}$$

$$w = C_0\sqrt{\frac{g}{k}}\sum_{n=1}^{5}\epsilon^n \; n \; a_n \sinh(nkz)\sin(n\theta) \tag{2.30}$$

Where u and w are the horizontal and vertical particle velocity components, while and the coefficients C_0, A_{ij}, B_{ij} are dimensionless functions of the water depth and wavelength. More details of this theory can be found in [47].

2.4.3 Wave Transformation

In the presence of an obstruction such as a submerged breakwater or floating breakwater, wave propagation will go through numerous physical processes involved in the wave transformation including wave shoaling, wave breaking, wave refraction, wave diffraction, wave reflection, wave transmission, wave-induced currents, creating waves with higher harmonic frequencies, etc [3]. In this study, however, only two dimensional studies will be performed. Hence, only wave breaking of irregular waves, wave transmission and wave reflection will be studied. Analysis of irregular waves has been discussed earlier in section 2.4.1. Generally, the incident wave height is attenuated by partially dissipating, partially reflecting and partially transmitting the incident wave. Hence,in the subsequent subsections, transmission and reflection of waves by submerged and floating breakwaters are described.

2.4.3.1 Wave Transmission

Transmission coefficient (K_t)are used to determine the height of the transmitted wave behind the breakwater. Transmission coefficient (K_t) is defined as a ratio between the incident wave height (H_i) and the transmitted wave height (H_t) (see Fig 2.3) and is expressed as follows:

$$K_t = \frac{H_t}{H_i} \tag{2.31}$$

In the presence of a submerged breakwater, transmission coefficient (K_t) is affected partly by wave related parameters (e.i. incident wave height, period, length and wave steepness) and partly by structurally related parameters (i.e. crest width and height, water depth, submergence depth, porosity, slope, etc.) [3]. Numerous laboratory experiments have been performed to quantify and formulate the transmission coefficients (K_t) behind the submerged breakwaters such as d'Angremond et al. (1996)[48], van der Meer et al. (2004)[49], Panizzo and Briganti. (2007)[50], Buccino and Calabrese. (2007)[51], Goda and Ahrens. (2008)[52], etc.

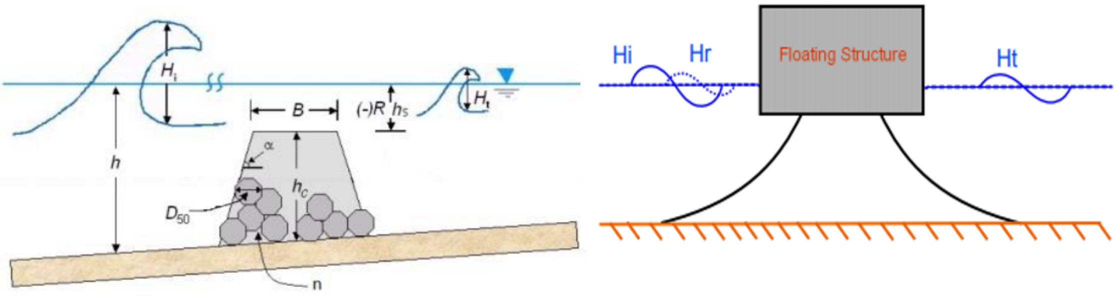

(a)   (b)

Figure 2.3: Wave interaction between submerged breakwater (a) [53] and floating breakwater (b) [54].

In the case of floating breakwaters, their efficiency and effectiveness are solely defined by the transmission coefficient (K_t). An extensive literature review on the research and development of floating breakwaters including can be found in this article [13].

2.4.3.2 Wave Reflection

Reflection is also another phenomenon in which part of the incident wave height is bounced back seaward the submerged or floating breakwater. The reflected wave height (H_r) is the product of the reflection coefficient (K_r) and the incoming wave height (H_i) (see Fig 2.3), where the reflection coefficient is expressed as follows:

$$K_r = \frac{H_r}{H_i} \tag{2.32}$$

For submerge breakwaters, the amount of the wave reflection somewhat depends on the porosity and the slope of the structure [3]. Also, the reflection coefficient decreases as the relative water depth. However, submerged structures are expected to have smaller reflection coefficients when compared to floating breakwater or non-overtopping breakwaters [55] due to the fact that more wave will be transmitted over the structure. Wave reflection, in case of floating breakwater, depends on the flexibility of the structure. Flexible floating breakwaters with more elastic deformation under wave action have smaller wave reflection than that of normal rigid floating [56].

Chapter 3

Irregular Wave Breaking on Irregular Topography

This chapter deals with the irregular wave propagation on an irregular bed topography (barred beach profile) that was performed originally by Boers [57] in a physical wave flume. The experimental data are compared with numerical results obtained using the open-source CFD model, REEF3D. This verification will show and prove the capability of REEF3D for capturing the nearshore hydrodynamics such shoaling and breaking on an irregular bed through the surf zone.

3.1 Experimental Set-up

Boers [57] performed experiments with irregular waves in the large physical wave flume at Delft University of Technology with dimensions of 40 m length, 0.8 m wide and 1.05 m high. These irregular waves were generated by the hydraulically driven piston-type wave board. Besides the wave board, the flume was equipped with a reflection compensation system to minimize re-reflections at the wave board from the nearshore reflected waves. The still water level during the experiments was set at 0.75 m with respect to the bottom of the flume. The bathymetry that resembled a mild-slope barred beach profile had a breaker bar and a surf zone trough with a flat bottom part extends from the toe of the slope to x = - 5 m where the wave board is located as illustrated in Figure 3.1.

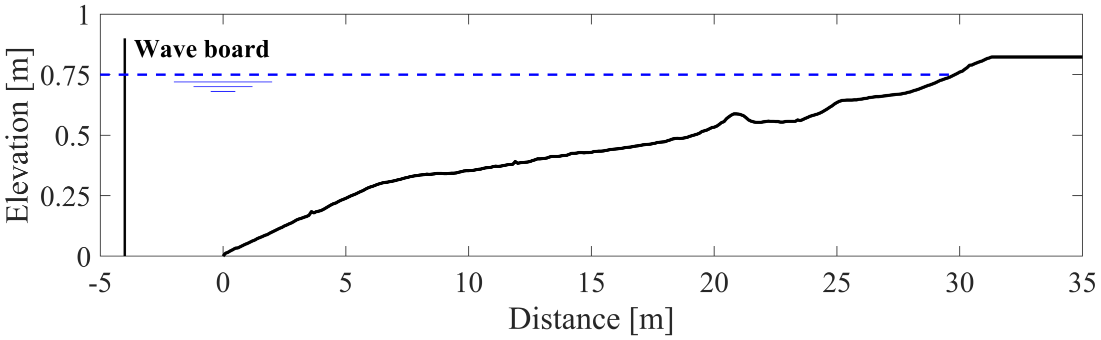

Figure 3.1: Boers (1996) Experimental setup [57].

Boers (1996) ran three different wave conditions with different significant wave heights H_{m0} and peak periods T_p as shown in the Table 3.1. Wave gauges and LDVs were used to obtain free surface elevation time series from 70 cross-shore locations sampled at 20 Hz. Besides the free surface elevation, velocities were measured at three different directions with a sampling frequency of 100 Hz.

Table 3.1: Wave parameters as used in the Boers (1996) experiment

Wave Parameters	H_s[m]	T_p [s]
A	0.157	2.05
B	0.206	2.03
C	0.103	3.33

3.2 Numerical Set-up

The numerical model REEF3D is applied to the Boers experimental cases to simulate the variation of the free surface elevation at different locations. A two-dimensional rectangular numerical wave tank (NWT) is used to simulate two selected experimental wave conditions. Dirichlet wave generation (DWG) and the active wave absorption (AWA) methods mentioned in chapter 2 are used to generate and absorb the waves in the numerical wave tank. The active absorption at the end of the tank generates a wave opposite to the reflected one which effectively cancels out the reflections. The numerical domain of the NWT is 36.3 m long and 1 m high. The water depth (d) is kept as in the experiment at 0.75 m.

In REEE3D, the irregular bed topography (Figure 3.2) is generated using a 'geo.dat' file with XYZ coordinates in ASCII format and then interpolated into a bathymetry in DIVEMesh.

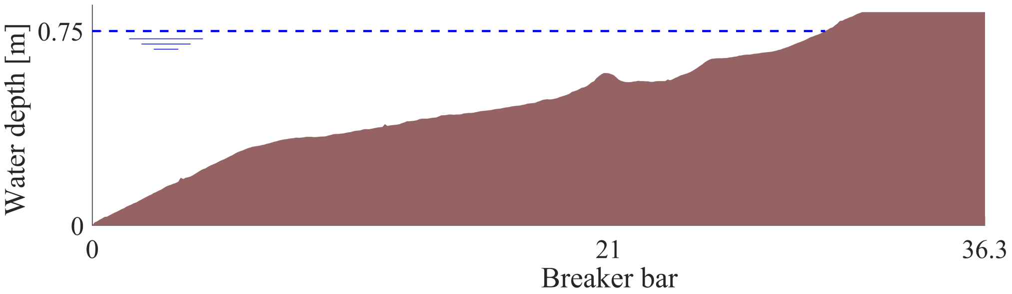

Figure 3.2: Numerical setup of Boers irregular bed in the Numerical Wave Tank

In this study, we considered two wave conditions to be simulated numerically. The first case (Case 1) features low steepness with a signicant wave height H_s = 0.103 m and and a peak period of T_p = 3.33 s . The second case (Case 2) features high steepness with H_s= 0.157 m and T_p = 2.05 s.

In this particular simulation, the waves are generated using free surface reconstruction technique (Section 2.3.4) for the irregular waves [42] at the left boundary. This technique precisely reproduces the wave amplitudes, wave frequencies, and wave phases of a time history of free surface elevation of an irregular wave train allowing the accurate numerical replication of the experimental free surface elevation.

3.3 Results

This section deals with the numerical results of Case 1 and Case 2 mentioned above. To demonstrate the ability of REEF3D model for capturing the hydrodynamic processes and the evolution of the irregular waves over the barred beach, both the spectral transformation of the wave energy $E(f)$ and the temporal variations of the instantaneous surface elevation (η) for the irregular wave breaking are presented and compared. The grid size (dx) is set to 0.01 m to capture the dominant features of wave breaking in the shoaling region and the surf zone.

Initially, the numerically computed time series of the free surface elevation obtained by the wave reconstruction method [42] is compared with the experimental data [57] at six selected wave gauges and presented in Figure 3.3 and Figure 3.4. For the waves featured with less steepness, an excellent agreement for all the wave gauges along the profile is achieved with only small differences in phase and amplitude appear for a few waves. Also, it is important to notice that the amplitudes and the shape of the less steep waves are well captured with a grid size of (dx) = 0.01 (see Figure 3.3). However, the steep waves are not well captured by the same grid size.

The Figs 3.4 highlight the result of using the grid size of $(dx)= 0.01$ for the steep waves. Although a good agreement is obtained for the first four wave gauges (see Figs 3.4 a,b,c,d), the last two wave gauges placed before and after the breaker bar is found to be less in agreement with the experimental data. The less agreement found with using this grid size can be due to the rapid and continuous breaking process by these steep waves which involve a quicker transformation of the wave geometry. Therefore, a finer grid size (i.e. $dx = 0.005$) is required to generate more accurate results that will not only agree well with the experimental results but also capture the dominant features of the breaking processes.

All in all, the numerical irregular free surface elevations versus time at different wave gauge locations during the wave transformation processes are in good agreement with the experimental time-series of the free surface elevation. However, there are some differences onshore the breaker bar after breaking, for high steep waves, that could be explained by the presence of the high-frequency waves reflected at the right boundary.

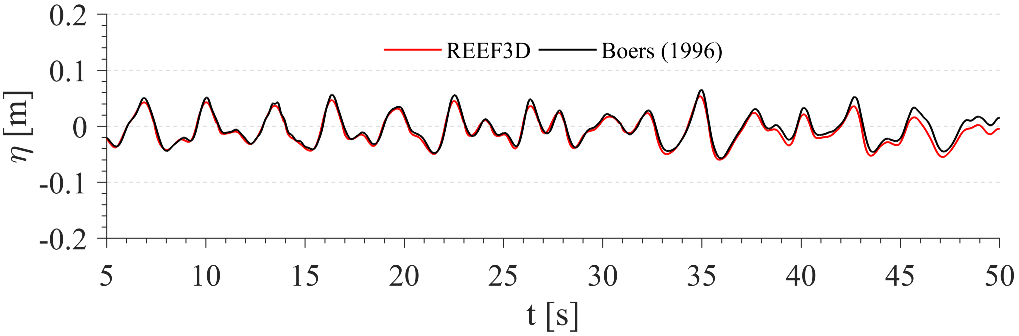

(a) WG at $x = 0$ m

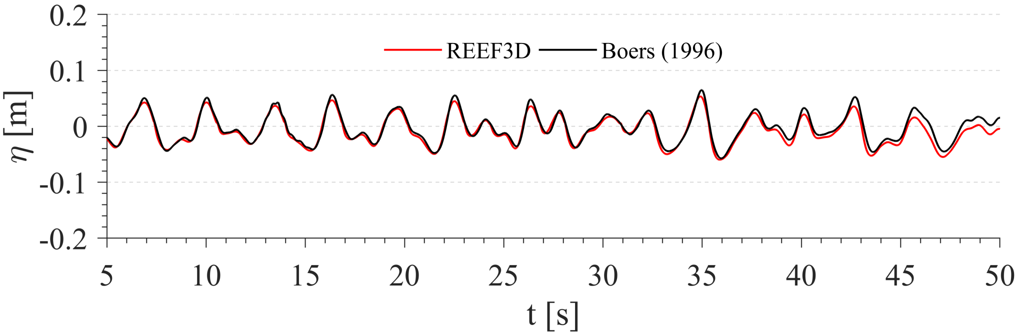

(b) WG at $x = 6$ m

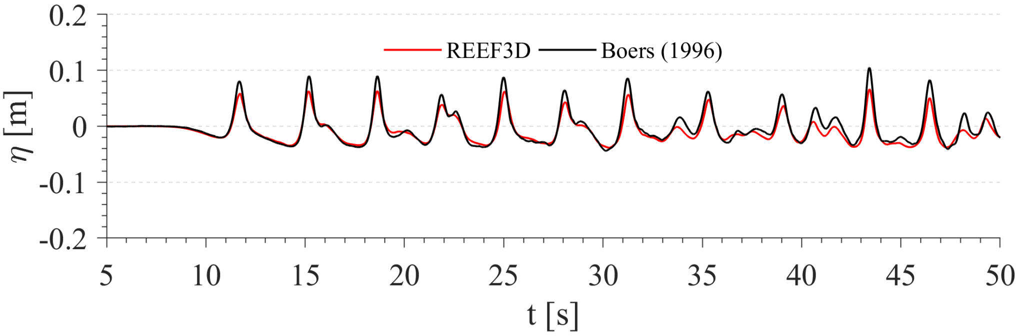

(c) WG at $x = 17.5$ m

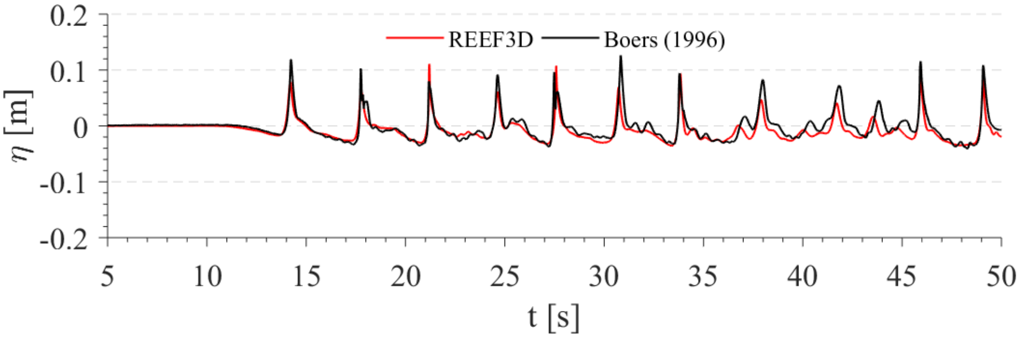

(d) WG at $x = 21.85$ m

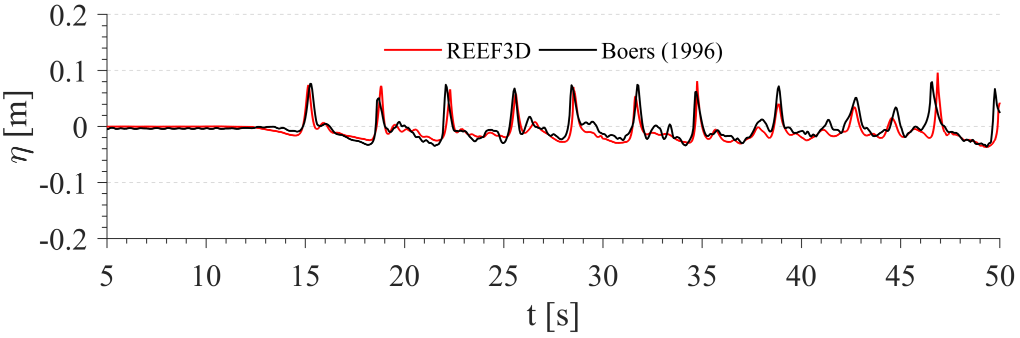

(e) WG at $x = 23$ m

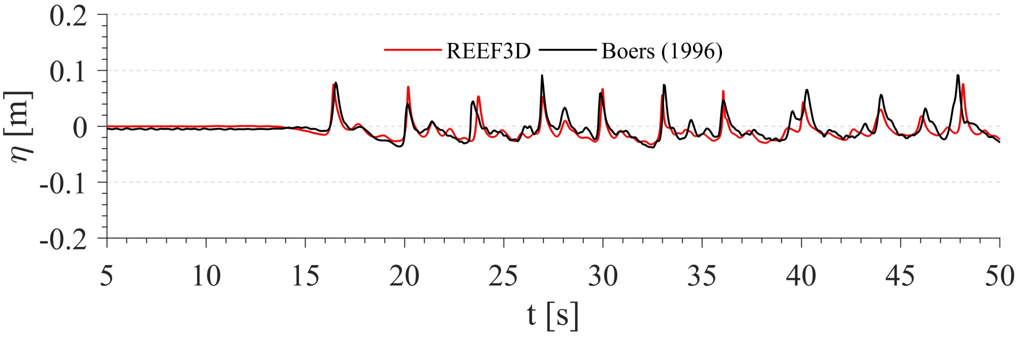

(f) WG at $x = 25$ m

Figure 3.3: Comparison of the experimental and numerical result of the less steep irregular wave signal ($H_s = 0.103$ m, $T_p = 3.33$ s) at six selected wave gauges over a bar-trough profile.

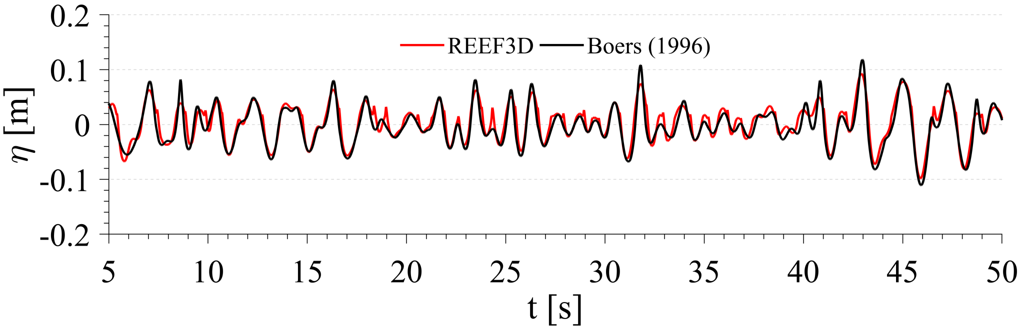

(a) WG at $x = 0$ m

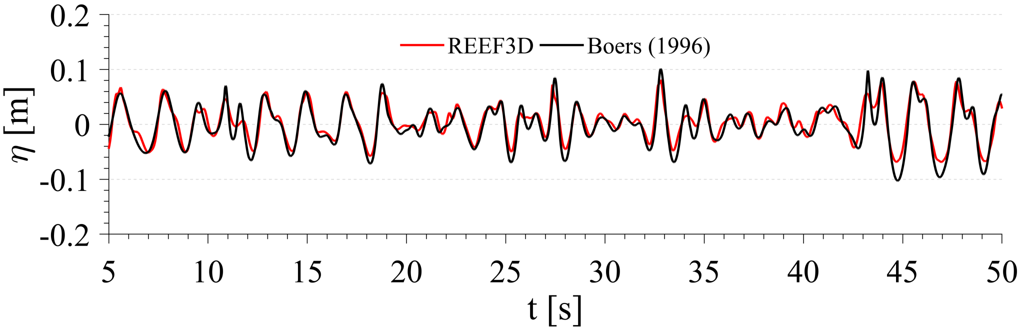

(b) WG at $x = 2$ m

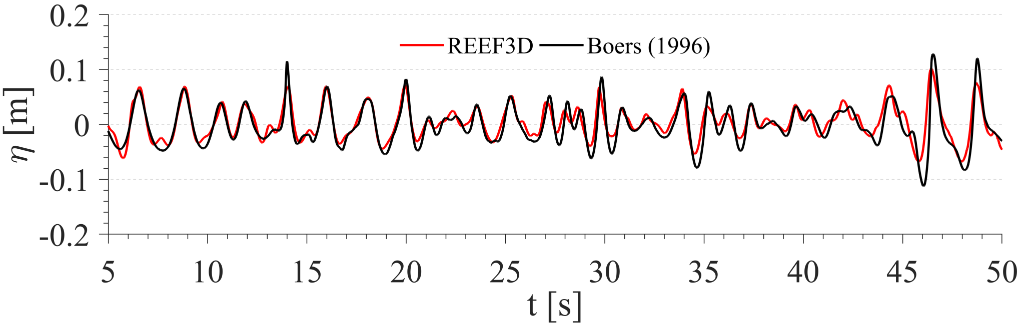

(c) WG at x = 4 m

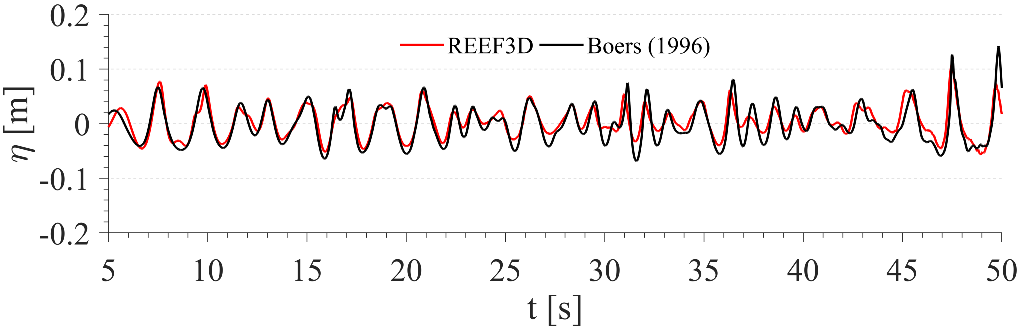

(d) WG at x = 6 m

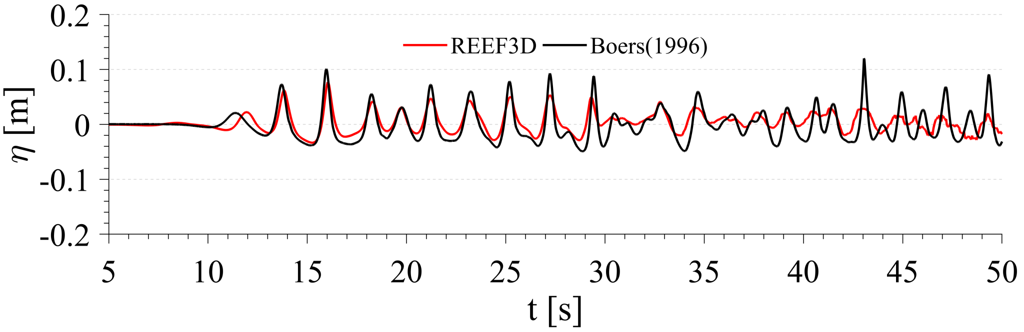

(e) WG at x = 17.5 m

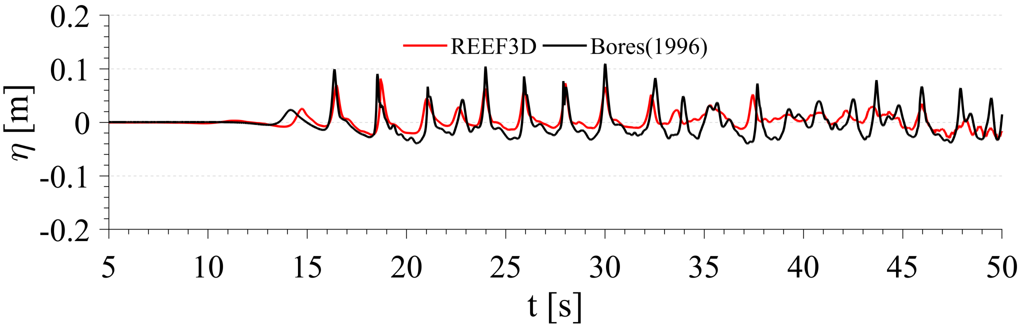

(f) WG at x = 21.85 m

Figure 3.4: Comparison of the experimental and numerical result of the steep irregular wave signal (H_s = 0.157 m, T_p = 2.06 s) at six selected wave gauges over a bar-trough profile.

Besides, the time series of the free surface elevation, spectral comparisons with the numerical and experimental data are made. The Figs 3.5 and 3.6 present the spatial evolution of the energy density spectrum of the surface elevation at different wave gauges. It is seen from those Figures that REEF3D model can successfully capture the dominant features of the attendant spectral evolution, both in the shoaling region and the surf zone.

In general, the spatial evolution of the energy density spectrum is characterized by a noticeable transformation from superharmonics to the subharmonics regions followed by transformation toward a broader spectral shape at the end of the numerical wave tank.

Over the initial section of the bed profile, there is a remarkable transformation of the energy density spectrum from the peak frequency to its higher harmonics (see Figs 3.5a,b and Figs 3.6a,b). Throughout the numerical wave tank, the energy spectra of the high steep waves is decreasing due to wave breaking as shown in Figure 3.6. In contrast, the low steep waves only start to break onshore of the breaker bar, x = 21.85 m (see Figure 3.5c), while waves shoal offshore the bar as seen by the small increase of high frequency energy, x = 15.5 m (see Figure 3.5b). There is, however, a noticeable difference in the energy density spectrum between the numerical and experimental results that could be due to the simplifications made during ensemble averaging used to generate these energy spectra.

Last but not least, numerical spatial snapshots of the relatively less steep waves are presented in Figure 3.7. The numerical results confirm the shoaling process offshore and on the breaker bar in (a). In (b) and (c), the waves are seen to be breaking onshore the breaker bar and on the foreshore respectively.

All in all, the correspondence between the numerical and experimental results for the wave surface elevation and their energy density wave spectra is arguably good.

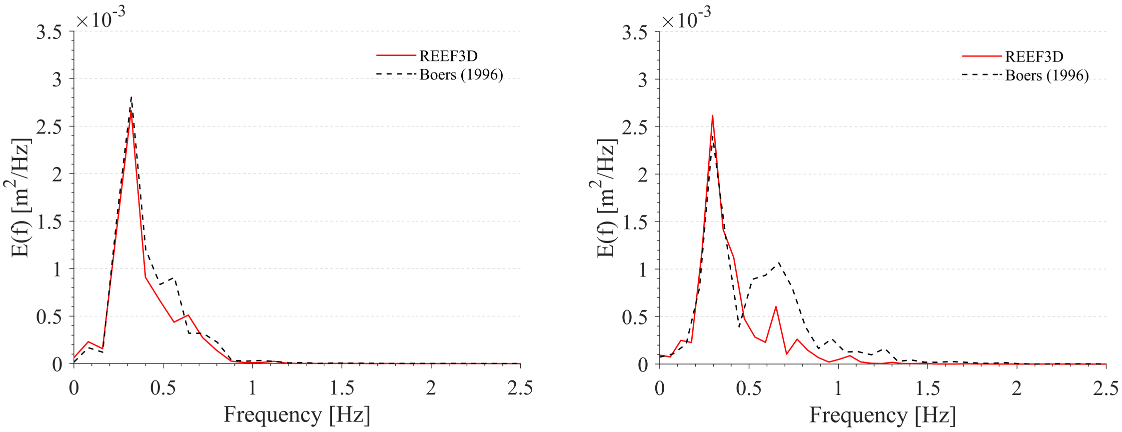

(a) WG at $x = 0$ m (b) WG at $x = 15.5$ m

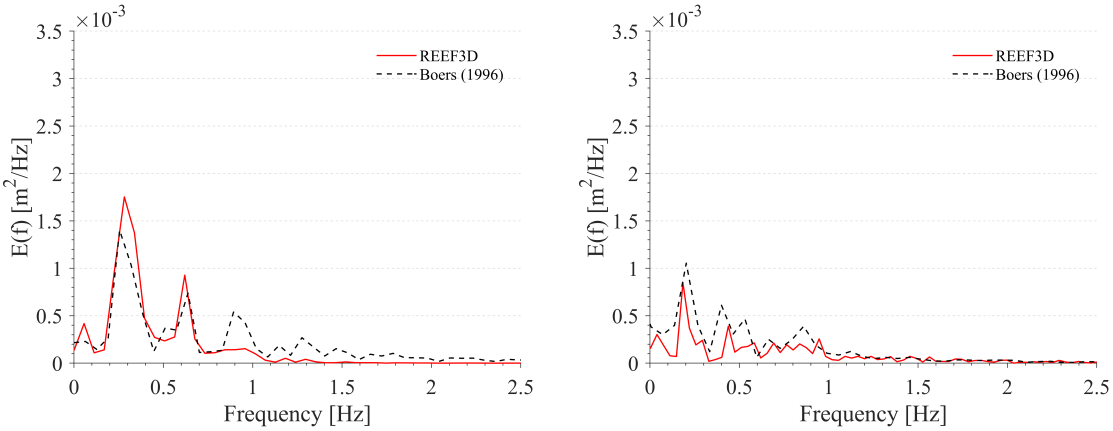

(c) WG at $x = 21.85$ m (d) WG at $x = 25$ m

Figure 3.5: Comparison of the numerical and experimental energy density spectra of surface elevation at different stations for the less steep irregular wave ($H_s = 0.103$ m, $T_p = 3.33$ s) over a bar-trough profile.

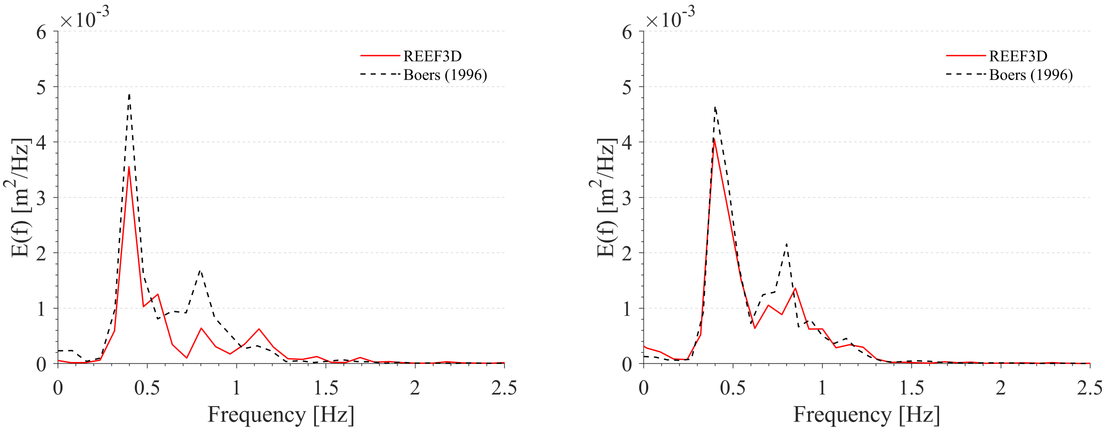

(a) WG at x = 0m (b) WG at x = 15.5 m

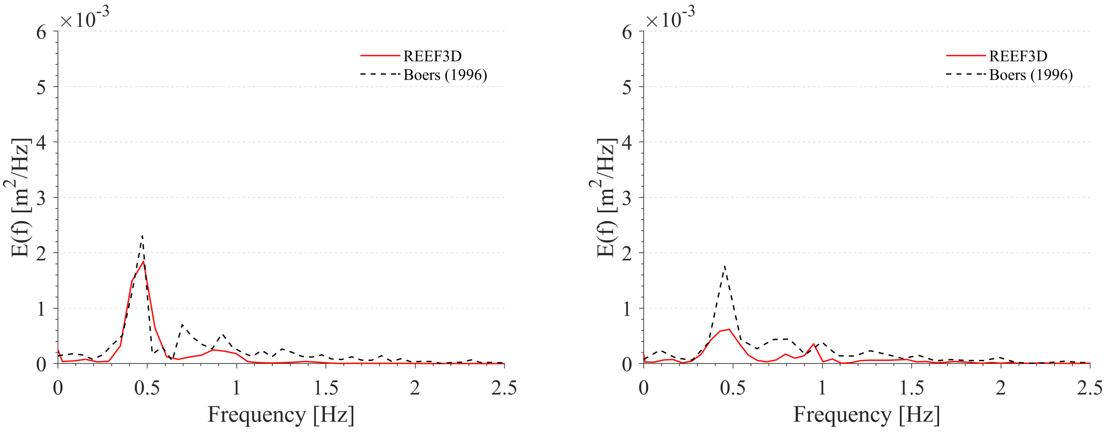

(c) WG at x = 21.85 m (d) WG at x = 25 m

Figure 3.6: Comparison of the numerical and experimental energy density spectra of surface elevation at different stations for the steep irregular wave (H_s = 0.157 m, T_p = 2.05 s) over a bar-trough profile.

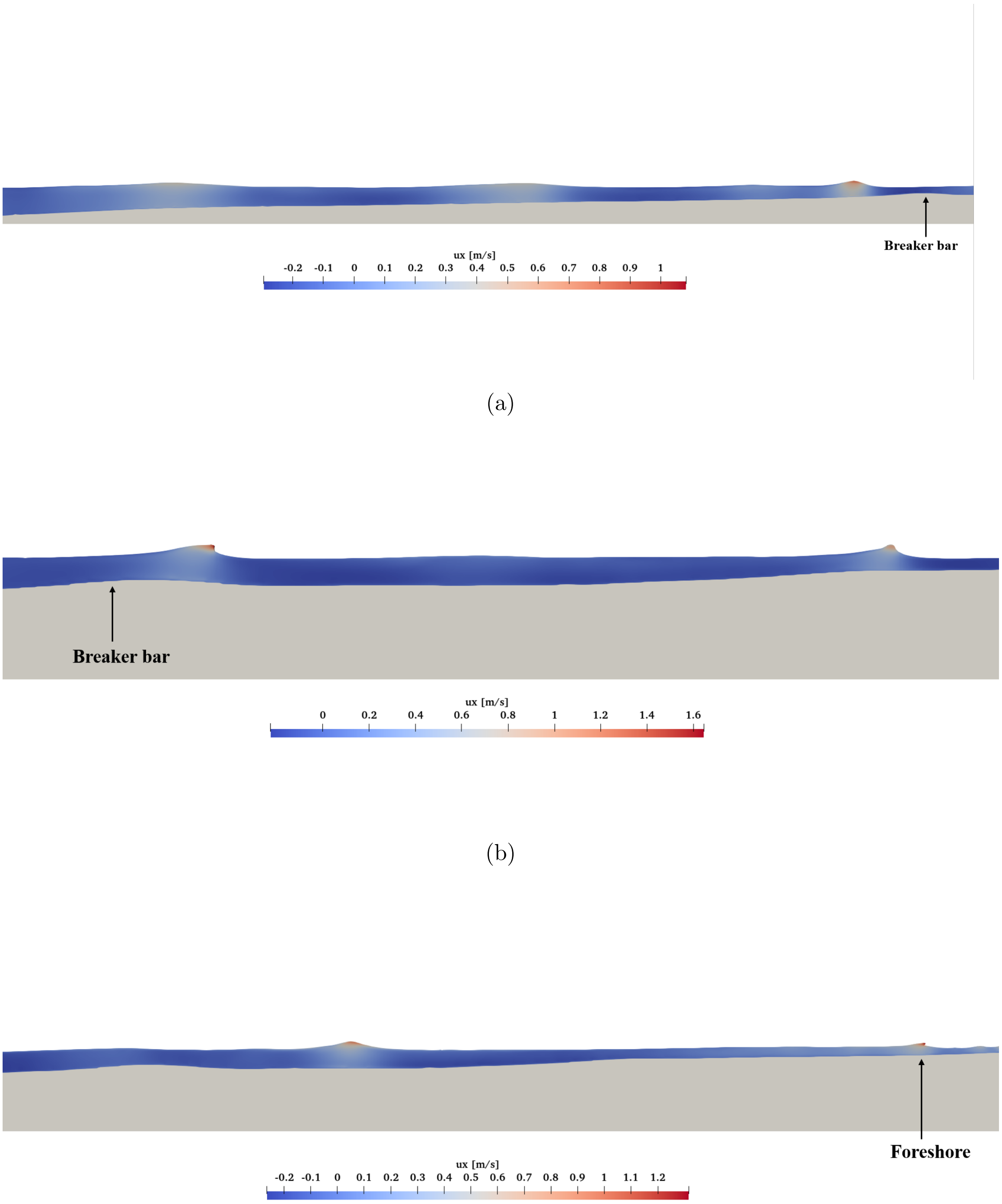

(a)

(b)

(c)

Figure 3.7: Less steep irregular wave ($H_s = 0.103$ m, $T_p = 3.33$ s): a) shoaling of the irregular waves b) breaking onshore the breaker bar c) breaking on the foreshore.

Chapter 4

Wave Interaction with a Submerged Porous Breakwater

In chapter 4, the wave reconstruction method was used to generate irregular waves which are identical to a wave signal close to the wave board, thus allowing for time series comparison of the free surface elevation. From this chapter, it is confirmed that the open-source CFD model REEF3D [26] can simulate well the behaviour of wave breaking on the natural irregular topography. In this chapter, we will validate the capability of REEF3D for simulating the wave behaviour interacting with a structure. This chapter will mainly focus on the simulation of wave–structure interactions with a submerged porous breakwater (SBW).

4.1 Validation of the Submerged Porous Breakwater

In this chapter, REEF3D is used to simulate the wave interaction with a submerged porous breakwater. At first, the wave interaction is validated by comparison with experimental data from Hieu and Tanimoto (2006) [58]. REEF3D model uses the Volume Averaged Reynolds Averaged Navier-Stokes (VRANS) equations formulated in section 1.4.1.3. These VRANS equations (Eq. 1.12 and Eq. 1.13) contain the resistance coefficients α and β that need to be specified. However, most of the works existing in the literature on the variation of resistance coefficients are based on various theoretical assumptions, physical experiments, and numerical calibrations. Therefore, the resistance coefficients are chosen to be $\alpha = 650$ and $\beta = 2.2$ based on a numerical validation study by Sasikumar et al. (2017) [25] that found the set of α and β coefficients to be very satisfactory.

4.1.1 Experimental Set-up

Hieu and Tanimoto (2006) performed an experimental study at the Hydraulic Laboratory of Saitama University, Japan [58]. The physical wave flume has dimensions of 18 m length, 0.4 m wide and 0.7 m high. The submerged breakwater is 0.33 m high, 1.16 m wide at the base, and 0.3 wide at the crest with a slope of 1:1.30. The submerged breakwater is placed at 10.5 m from the wavemaker. The breakwater is made of stone material with a mean diameter $d_{n50} = 0.025$ m and porosity $n = 0.45$ (see Fig 4.1). The incident wave height and period used in this experimental study are H = 0.092 m and T = 1.6 s, respectively. Wave gauges are used to obtain the free surface elevation time series from 38 wave gauge at three different locations, in the offshore side, lee side and on the submerged breakwater.

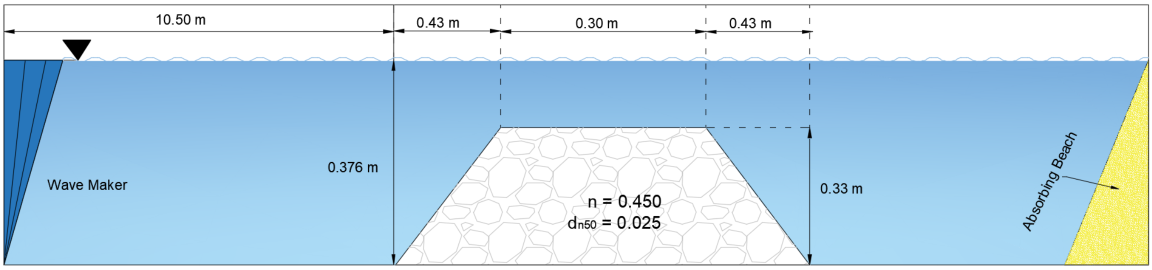

Figure 4.1: Experimental Set-up of the Submerged Porous Breakwater as tested by [58].

4.1.2 Numerical Set-up

A 2D numerical wave tank is used to simulate the experiment described above (see Sec.1.4.1.2) and the numerical results are compared with then the experimental data. The numerical model is set up based on the experimental study carried out by [58]. The numerical domain of NWT is 20 m long, 0.005 m wide and 0.8 m high (see Fig 4.2). A fifth-order Stokes waves with wave height, H = 0.092 m, wave period, T = 1.6 s and wavelength, $\lambda = 2.83$ m are generated with water depth, d = 0.376 m. In this study, the result from [59] using a REEF3D model, is used as a reference point. The study found out that a grid size of $dx = 0.005$ m yields good results with reasonable computational time. Hence, the same grid size is selected for computation.

Moreover, wave generation and absorption in the numerical wave tank is carried out using the relaxation method. In this method, the wave energy is dissipated by ramping the free surface down to the still water level, the velocity to the zero and the pressure to its hydrostatic distribution for still water condition. Besides, the reflected waves travelling towards the left boundary are absorbed with this method. Similarly, at the right boundary, an active absorption beach is imposed that generates a wave

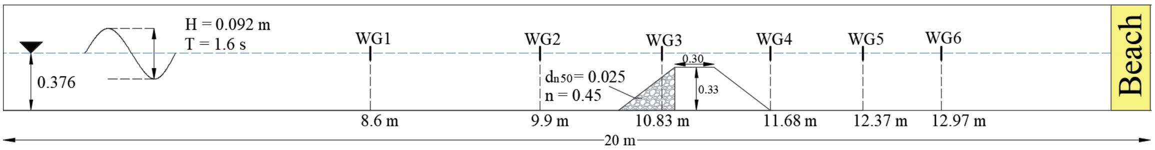

Figure 4.2: Numerical Set-up of the SBW used and the locations of the different wave-gauges.

opposite of the reflected wave, hence cancelling it out to ensure more representative results.

Figure 4.2 shows the numerical set-up used in the simulation. The free surface elevations are calculated, identically to the experiment, at three different locations; two wave gauges on the upstream side (WG1 and WG2), one wave gauge on the top of the seaward slope (WG3), one on the leeward toe (WG4), and two behind the submerged breakwater (WG5 and WG6).

4.1.3 Results

Figure 4.2 presents the comparison of the numerical results and the experimental data of the free surface elevation versus time at six different wave gauge locations. Generally, it is clear that the numerical results agree well with the experimental data. Both the wave amplitudes and wave phases are reproduced reasonably well in the numerical model.

Also, it is observed that the numerical model is capable of reproducing the features of the evolution and decomposition of the wave. This is seen from the wave signals in Figure 4.2b where wave shoal resulting in a sharp wave crest. Also, the detachment of the secondary waves is seen in Figure 4.2c which is accompanied by wave energy dissipation due to wave breaking. Therefore, it is seen deduced that REEF3D model is capable of simulating the waves on the downstream of the submerged breakwater in the presence of wave breaking process.

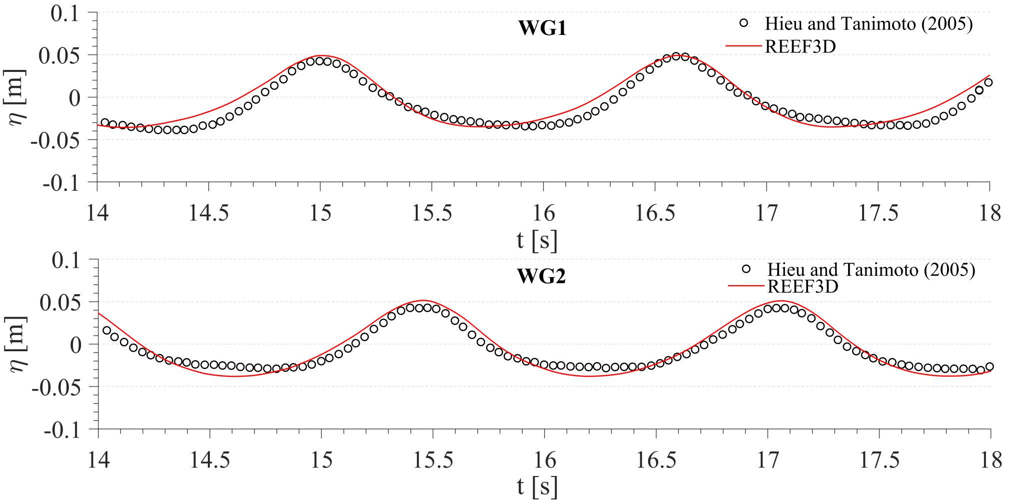

(a) WG1 at x = 8.6 m and WG2 at x = 9.9 m

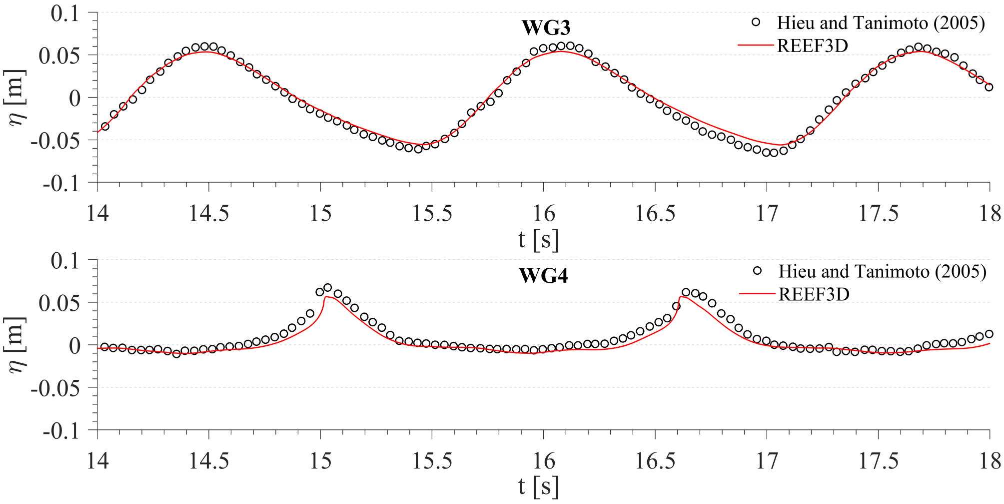

(b) WG3 at x = 10.83 m and WG4 at x = 11.68 m

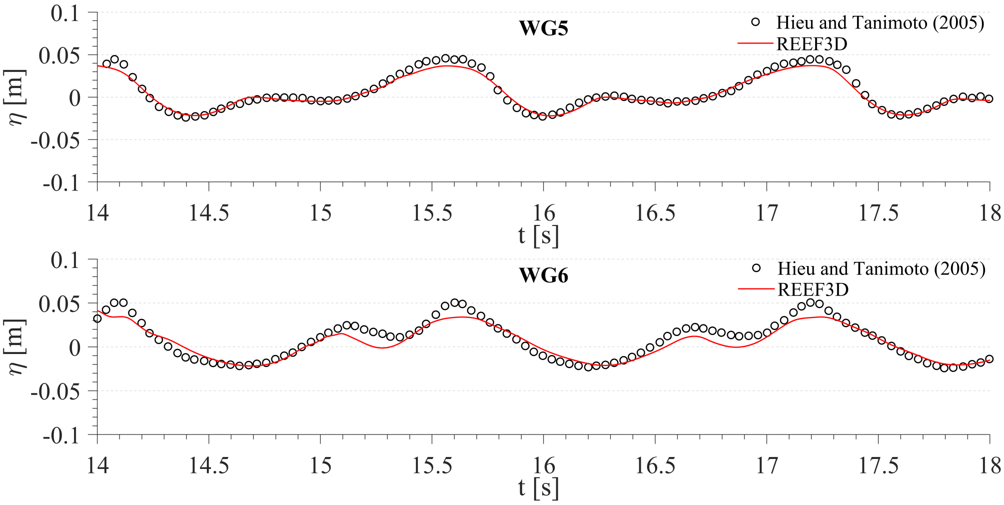

(c) WG5 at x = 12.37 m and WG6 at x = 12.97 m

Figure 4.2: Comparison of free surface elevations between the numerical and experimental results of SBW at six different wave gauges locations across NWT.

Root Mean Square Error (RMSE) is further used to confirm and quantify the degree of the accuracy of the numerical results compared to the experimental data. From Figure 4.3, it is clearly seen that the computed errors at all wave gauge locations are very small. This, in turn, implies a very good agreement between the numerical and the experimental free surface elevation. Finally, the very good agreement between the numerical results and the experimental data obtained in this study gives us confidence in the ability of the model on the simulation of wave interactions with porous structures using VRANS set of equations (Eq. 1.12 and Eq. 1.13) with the specified resistance coefficients (α and β) presented by [59].

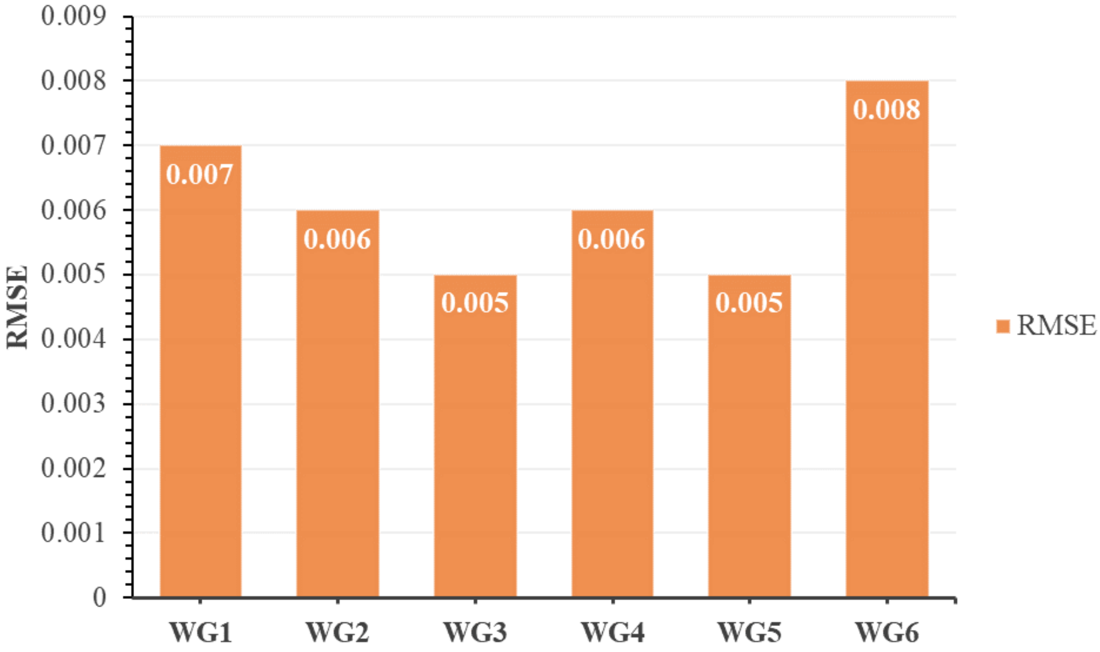

Figure 4.3: Comparison of accuracy between the numerical and experimental results at six different wave gauges locations using RMSE.

Figure 4.3 shows some snapshots of the wave propagation and transformation of the free surface in presence of porous submerged breakwater.

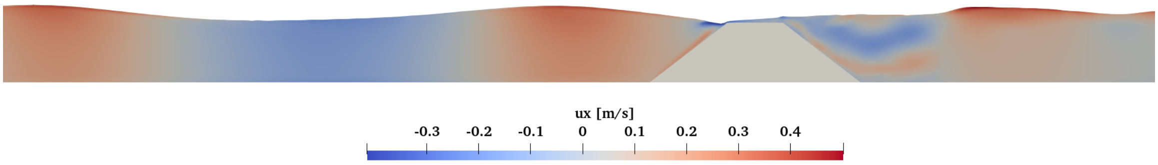

(a) Wave interact with the SBW

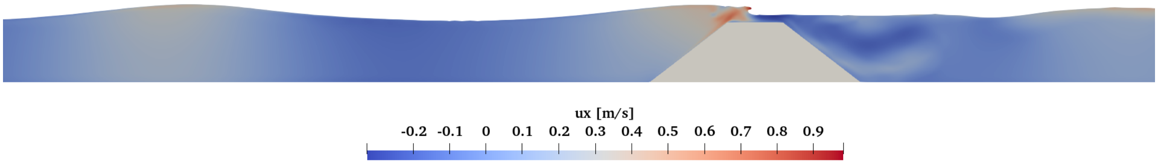

(b) Wave shoaling on the crest of the SBW

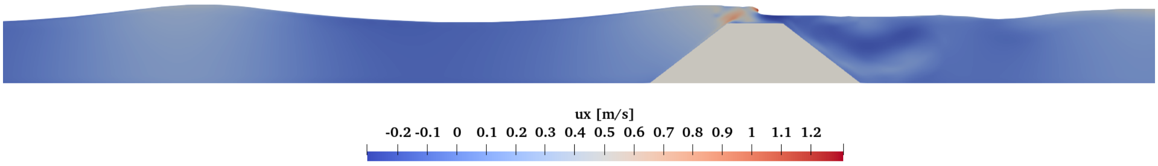

(c) Wave breaking on the crest of the SBW

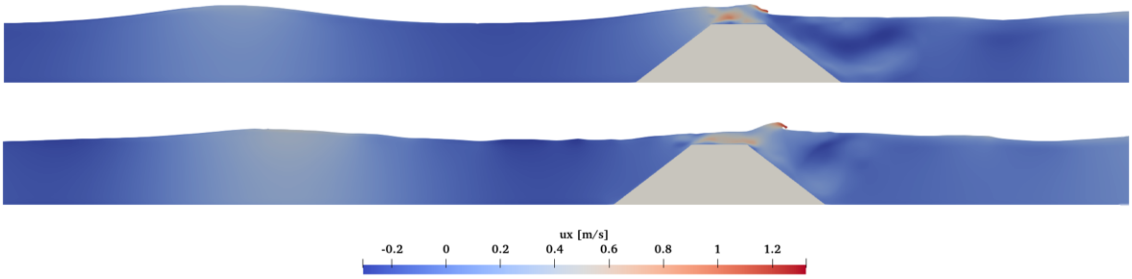

(d) Wave continues breaking on and after the crest and of the SBW

Figure 4.3: Snapshots of the wave interaction with the submerged porous breakwater.

Chapter 5

Wave Interaction with a Combined Breakwater System

This is chapter 5, REEF3D is used to simulate the wave interaction with a submerged porous breakwater (SBW). In this chapter, the validated model will be used to simulate the wave interaction with a combination of the Submerged Breakwater (SBW) and the Floating Breakwater (FBW).

5.1 Submerged Breakwater (SBW) and Floating Breakwater(FBW) Numerical Simulation

As discussed earlier in SECTION 1.5, the FBWs are only functional and economical in the presence of short waves. Practically, FBWs can successfully suppress these short waves if their length is greater than the wavelength of the incoming short waves. Typical values for wave periods and wavelengths in coastal water can be in the order of $10 - 100$ s and $10 - 1000$ m, respectively [44]. To effectively attenuate this larger wavelength by the FBW, a very large length is required to obtain a small wave transmission coefficient. This can be unfavourable in terms of cost, durability, and coastal aesthetics side. Hence, the wavelengths of these short waves need to be reduced in order to make the floating breakwater practically functional in wave attenuation.

Therefore, a combined system consisting of a submerged porous breakwater (SBW) and a floating breakwater (FBW) is investigated. The main function of the SBW is to induce wave breaking in order to decompose the incident wave into those of a shorter wavelength. In this study, the structurally related parameters of the submerged porous breakwater are kept the same as described in section 4.1.2, while varying configurations of the FBW are used. Three different cases are numerically simulated with three different distances from the lee side of the SBW to FBW. For each case, five different configurations related to the geometry of the FBW (see Table 5.1) are initially simulated.

Table 5.1: Floating breakwaters (FBWs) cases with various configurations.

Case	FBW length (L)	Distance between SBW and FBW
1	1.5λ 1.75λ 2.0λ 2.25λ 2.5λ	1λ
2	1.5λ 1.75λ 2.0λ 2.25λ 2.5λ	2λ
3	1.5λ 1.75λ 2.0λ 2.25λ 2.5λ	3λ

$^*\lambda$:wavelength

5.1.1 Case 1: FBW at 1λ from the SBW

This is the first case to be numerically simulated in order to investigate the effectiveness of such a combined system. As seen from Figure 5.1, the location and the configuration of the SBW are kept the same as in section 4.1.1. The FBW is located at one wavelength from the lee side of the SBW and it is considered to be moored such that it is restricted from motion under the influence of the waves. The numerical domain of NWT is 25 m long, 0.005 m wide and 0.8 m high with a water depth of d= 0.376 m. A fifth-order Stokes waves with wave height, H = 0.092 m, wave period, T = 1.6 s and wavelength, $\lambda = 2.83$ m are used. The wave generation and absorption in the numerical wave tank are exactly the same as described in section 4.1.2.

Four wave gauges are used to obtain the free surface elevation at four different locations (see Fig 5.1). WG1 and WG6 are placed upstream and downstream the SBW to measure the incident and transmitted waves respectively. Similarly, WG7 located just in front of the FBW is used to measure the incident waves on the FBW, while WG8 is used to measure the transmitted waves just behind the FBW.

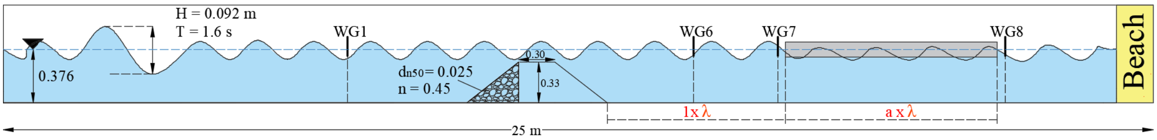

Figure 5.1: Numerical set-up of the NWT used for case 1 with four numerical wave gauges to measure the incident and transmitted waves in front and behind the SBW and the FBW respectively.

As labelled in Figure 5.1, $[a \times \lambda]$ stands for the different lengths of the FBW that will be simulated for this case. Figure 5.2 illustrates the details of the configurations of the FBW for case 1.

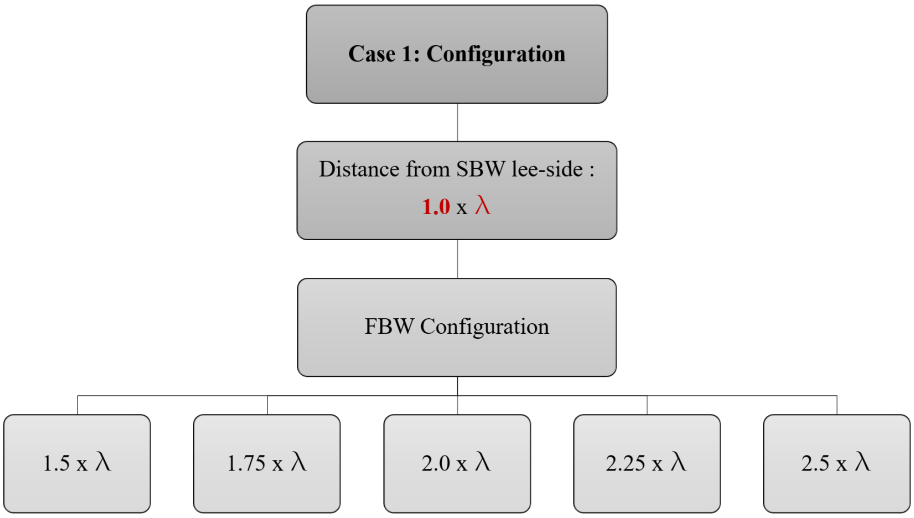

Figure 5.2: Floating breakwaters (FBWs) configurations used for case 1.

5.1.1.1 Configuration 1: FBW of length 1.5λ

This is the first configuration of case 1. The floating breakwater (FBW) is located at one wavelength from the lee side of the submerged breakwater (SBW) with a length of 1.5 times the wavelength.

It is seen in Figure 5.3a,b, and Figure 5.4a that the free surface elevation at WG1, WG6, and WG7 is slightly affected by the presence of the floating breakwater due to weak reflection. This same pattern in Figure 5.3a,b is almost observed in all the other configurations of case 1 with negligible deviations that will be presented in the following sections in terms of percentage of reduction of the free surface elevation/wave height. Owing to that, the incident and transmitted waves at WG1 and WG6 will not be presented in the remaining configurations to avoid repetition. Moreover, it is observed that the SBW alone reduces the incident wave height by approximately 49% on average for all the five configurations of case 1.

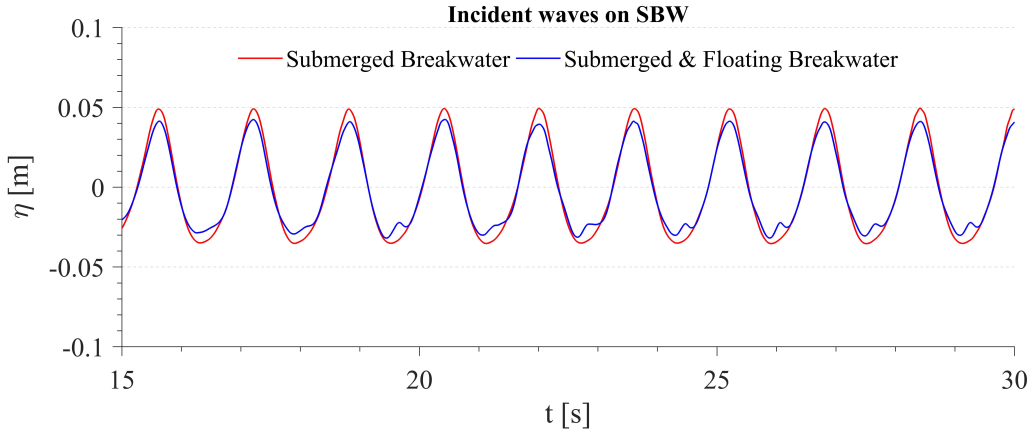

(a) Incident waves at WG1 placed at the upstream of the SBW with and without the FBW

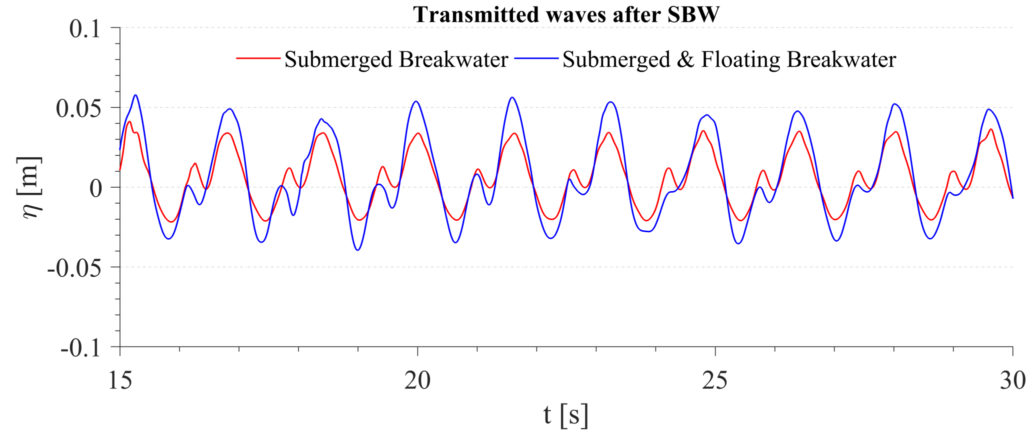

(b) Transmitted waves at WG6 placed at the downstream of the SBW with and without the FBW

Figure 5.3: Free surface elevation at WG1 and WG6 placed in front and behind the submerged breakwater with and without the floating breakwater on the lee side of the submerged breakwater.

Behind the FBW, the free surface elevation is largely damped out as shown in Figure 5.4b. The reduction of the incident wave height observed behind the FBW is approximately 91%. This means that the transmitted wave height across the combined submerged and floating breakwaters system is approximately 9% of the incident wave height.

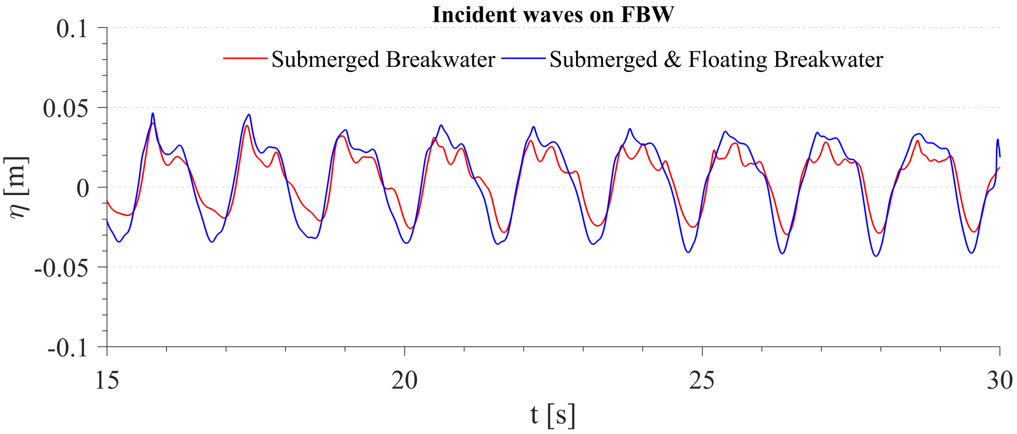

(a) Incident waves at WG7 placed just in front of the FBW with and without the FBW

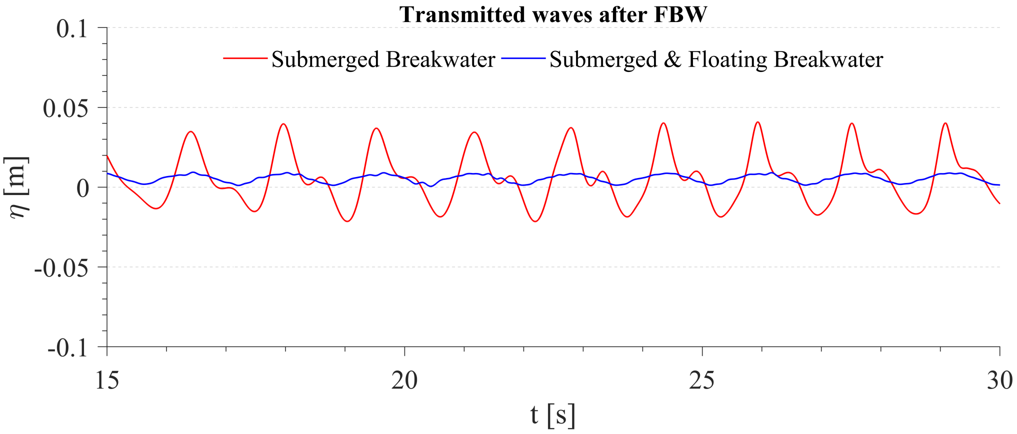

(b) Transmitted waves at WG8 placed just behind the FBW with and without the FBW

Figure 5.4: Free surface elevation at WG7 and WG8 placed just in front and behind the floating breakwater with and without the floating breakwater.

5.1.1.2 Configuration 2: FBW of length 1.75λ

The second configuration of case 1 represents the FBW with a length of 1.75 times the wavelength located at one wavelength from the lee side of the SBW.

The effect of the weak reflection is also observed in this configuration as shown in Figure 5.5a. Besides, it is seen in Figure 5.5b that the presence of the FBW significantly damps out the free surface elevations at WG8 that is located just behind the FBW. This large damping of the incident wave height across the combined submerged and floating breakwaters system accounts for roughly 93%. Hence, the transmitted wave height found behind the FBW is more or less 7% for this configuration.

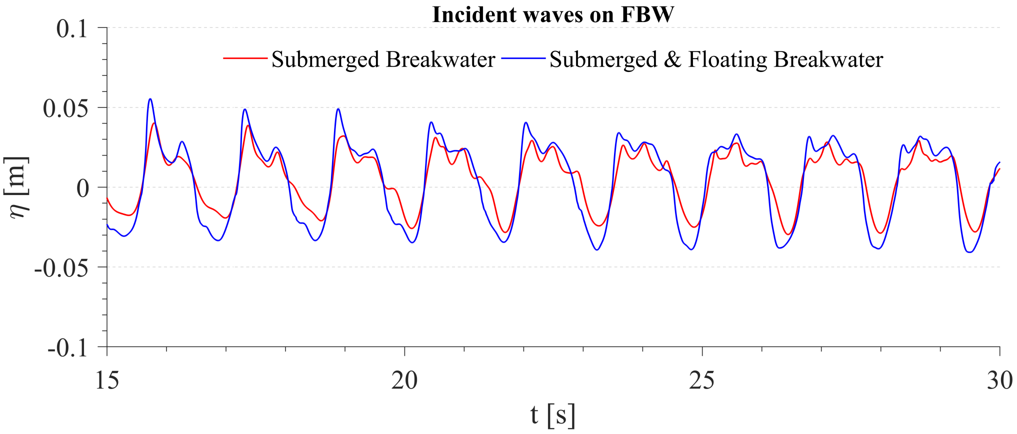

(a) Incident waves at WG7 placed jus in front of the FBW with and without the FBW

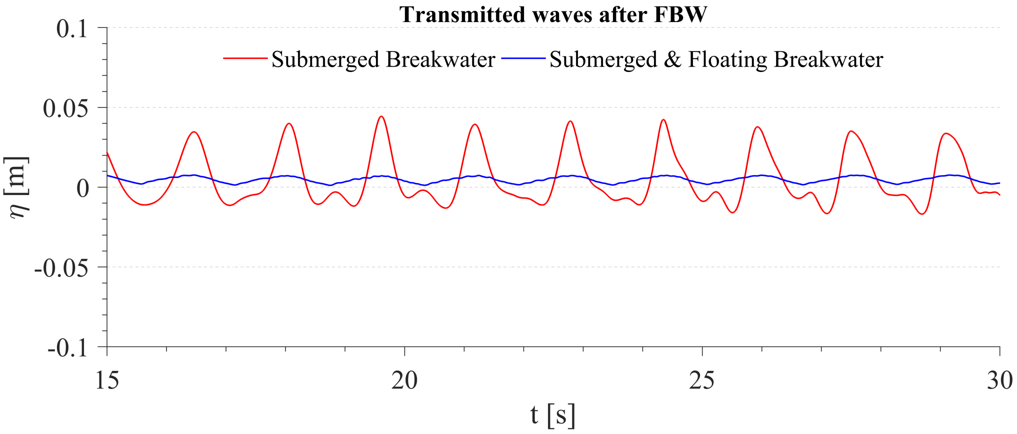

(b) Transmitted waves at WG8 placed just behind the FBW with and without the FBW

Figure 5.5: Free surface elevation at WG7 and WG8 placed just in front and behind the floating breakwater with and without the floating breakwater.

5.1.1.3 Configuration 3: FBW of length 2λ

Configuration 3 represents the FBW with a length of 2.0 times the wavelength which is located at one wavelength from the lee side of the SBW.

Similar to the previous configuration, the free surface is seen to be largely damped out in the presence of the floating breakwater as shown in Figure 5.6b. The transmitted wave height across the combined submerged and floating breakwaters system is approximately 6% of the incident wave height. Weak reflection effect is also seen in this configuration as shown in Figure 5.6a.

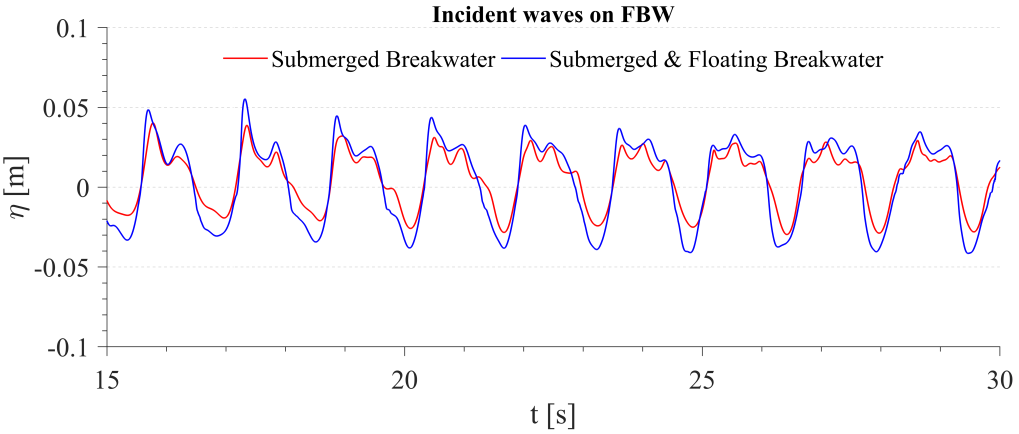

(a) Incident waves at WG7 placed jus in front of the FBW with and without the FBW

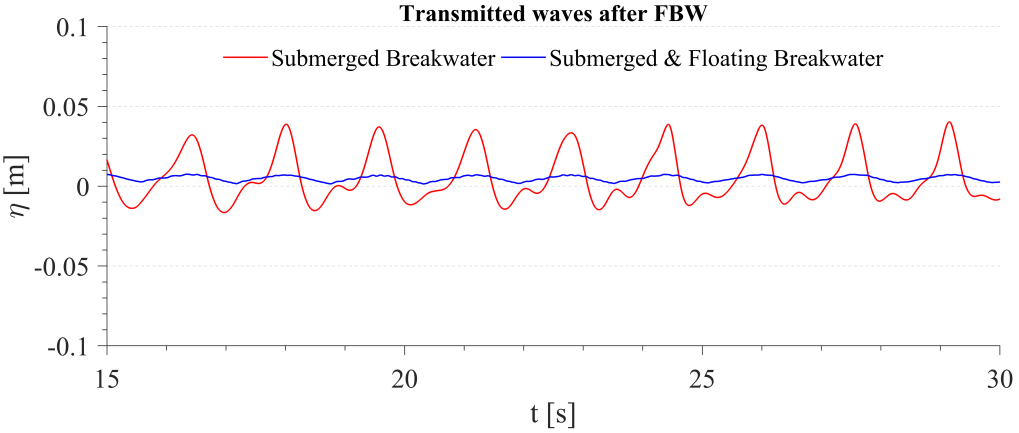

(b) Transmitted waves at WG8 placed just behind the FBW with and without the FBW

Figure 5.6: Free surface elevation at WG7 and WG8 placed just in front and behind the floating breakwater with and without the floating breakwater.

5.1.1.4 Configuration 4: FBW of length 2.25λ

This is the fourth configuration of case 1 represents the FBW with a length of 2.25 times the wavelength that is placed at one wavelength from the lee side of the SBW.

The effect of the weak reflection is also observed in this configuration as shown in Figure 5.8a. Furthermore, it is observed in Figure 5.8b that the presence of the FBW largely damps out the free surface elevations at WG8 which is located just behind the FBW. This large damping of the incident wave height across the combined submerged and floating breakwaters system accounts for roughly 80%. Hence, the transmitted wave height found behind the FBW is more or less 20% for this configuration. This result is relatively large in comparison to the previous configurations. This ,however, will be discussed in the discussion section (see section 5.1.4).

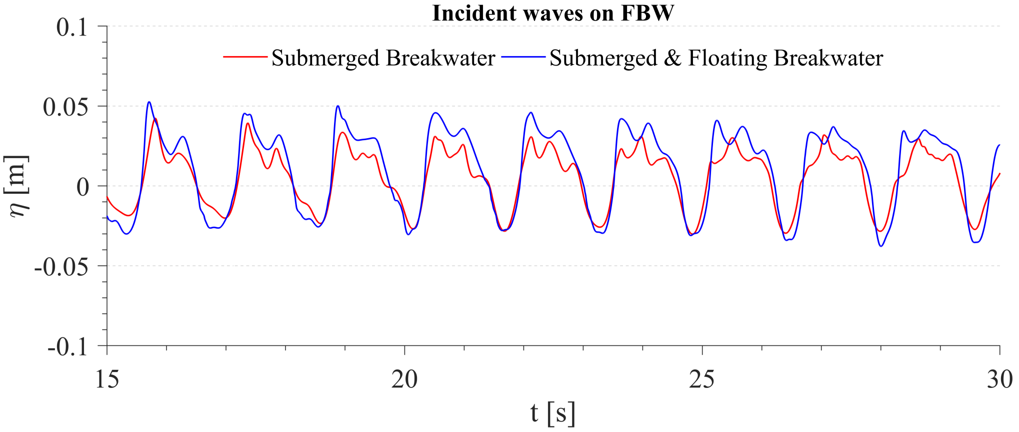

(a) Incident waves at WG7 placed jus in front of the FBW with and without the FBW

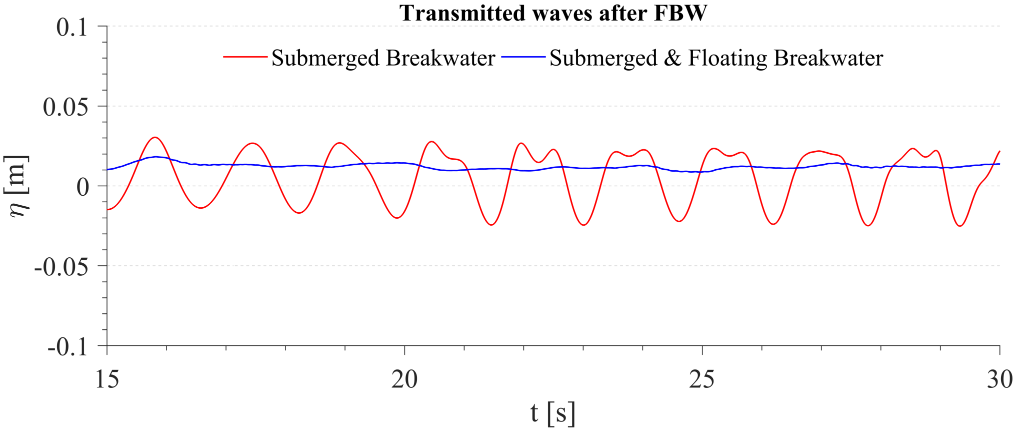

(b) Transmitted waves at WG8 placed just behind the FBW with and without the FBW

Figure 5.7: Free surface elevation at WG7 and WG7 placed just in front and behind the floating breakwater with and without the floating breakwater.

5.1.1.5 Configuration 5: FBW of length 2.5λ

This is the last configuration of case 1. The FBW is placed at one wavelength from the lee side of the SBW with a length of 2.5 times the wavelength.

The effect of the weak reflection is also observed in this configuration as shown in Figure 5.8a. In addition, it is clearly seen in Figure 5.8b that the presence of the FBW significantly damps out almost the free surface elevations at WG8 that is located just behind the FBW. This huge damping of the incident wave height across the combined submerged and floating breakwaters system accounts for roughly 96%. Therefore, the transmitted wave height found behind the FBW is approximately 4% for this configuration.

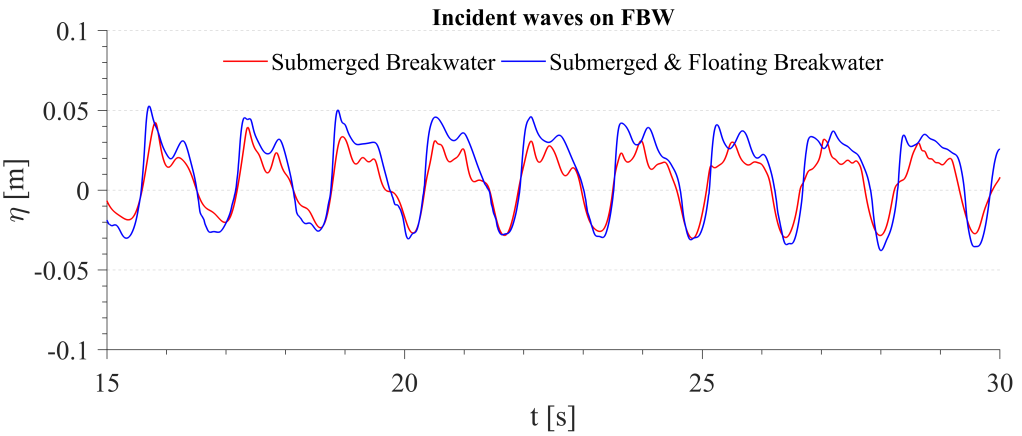

(a) Incident waves at WG7 placed jus in front of the FBW with and without the FBW

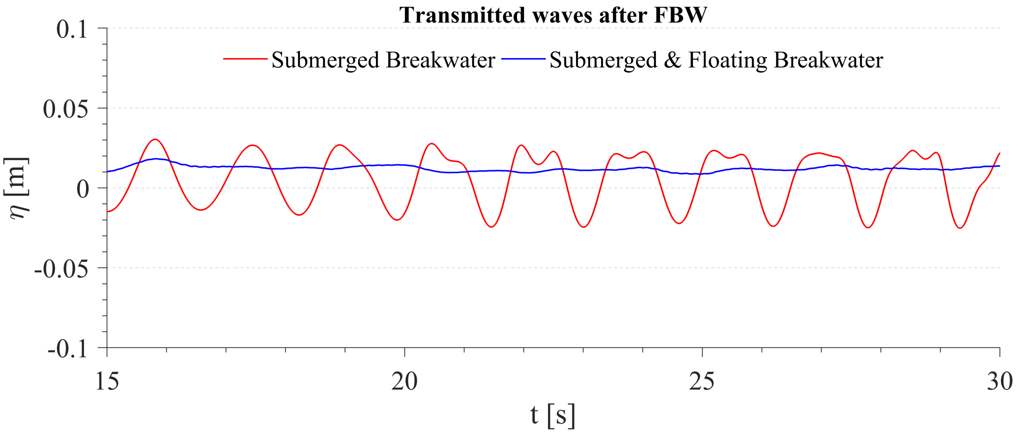

(b) Transmitted waves at WG8 placed just behind the FBW with and without the FBW

Figure 5.8: Free surface elevation at WG7 and WG8 placed just in front and behind the floating breakwater with and without the floating breakwater.

As discussed earlier, there are small deviations in terms of percentage reduction of the incident wave height after the SBW (see Fig 5.9a) and the FBW (see Fig 5.9b) for all the aforementioned configurations as illustrated in Figure 5.9. From Figure 5.9a, it can be deduced that the submerged breakwater (SBW) alone allows for a transmission of approximately 50% of the incident wave height averaged over all the configurations listed in the same Figure. However, the combined submerged and floating breakwaters system allows an average transmission of approximately 10%

(averaged over all the configurations listed in the same Figure) of the incident wave height.

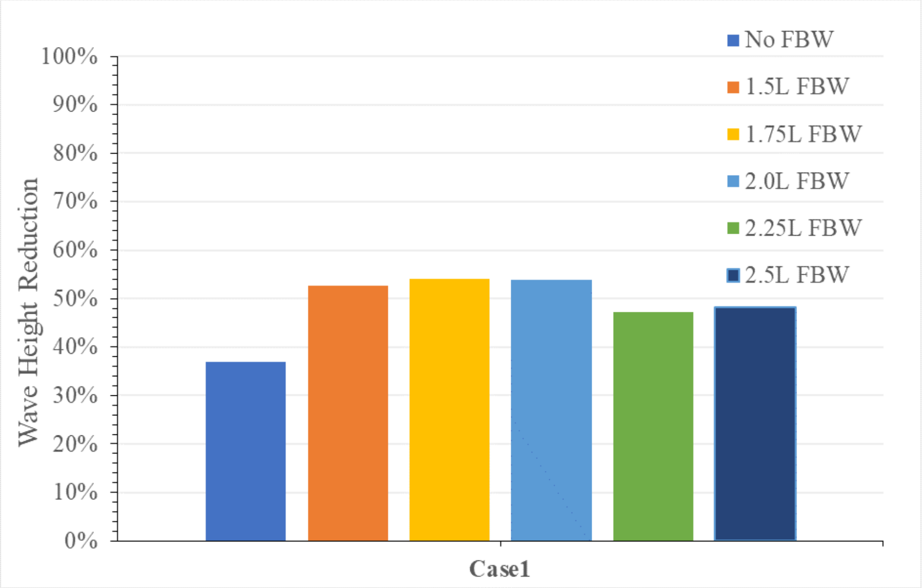

(a) Reduced wave height after the SBW with and without the FBW (L is the wavelength)

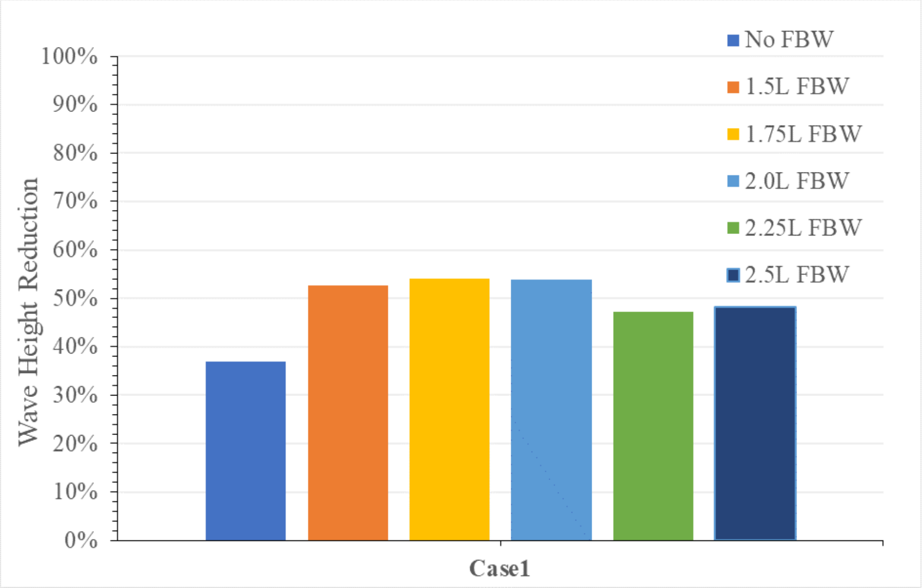

(b) Reduced wave height after the FBW with L is the wavelength)

Figure 5.9: Reduction of incident wave height after the SBW (a) and the FBW (b) in percentage.

Finally, the wave interaction with the combined submerged and floating breakwater system in the numerical wave tank is illustrated in Figure 5.10. As seen in this Figure, the thin floating breakwater is seen as a flat free surface due to its elongated dimensions.

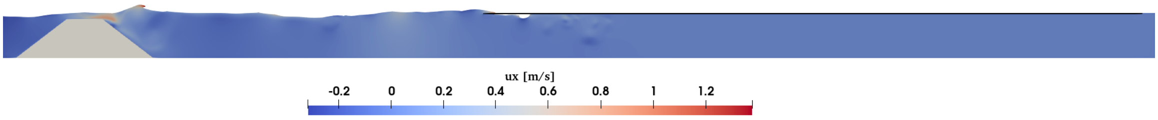

(a) Waves are breaking after the SBW

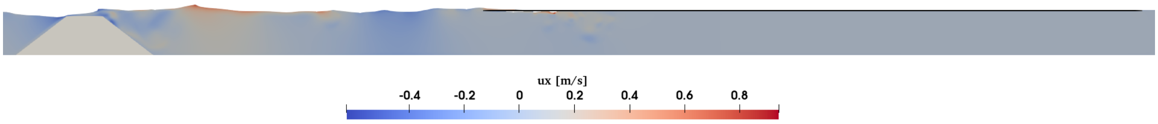

(b) Breaking waves interact with FBW

Figure 5.10: Wave interaction with the submerged porous breakwater (SBW) and the floating breakwater (FBW) placed at at 1λ on the lee side of the SBW.

5.1.2 Case 2: FBW at 2λ from the SBW

This is the second case to be investigated in the numerical wave tank. Figure 5.1 shows the location and the configuration of the SBW which is kept the same as in section 4.1.1. The FBW is located at two times the wavelength from the lee side of the SBW and it is considered to be moored such that it is restricted from motion under the influence of the waves. The numerical domain of NWT is 30 m long, 0.005 m wide and 0.8 m high with a water depth of d= 0.376 m. The wave type and its parameters and the wave generation and wave absorption method are the same as in case 1.

Similarly, four-wave gauges are used to obtain the free surface elevations at four different locations (see Fig 5.11). WG1 and WG6 are installed (at about the same distances shown in Figure 4.2) upstream and downstream the SBW to measure the incident and transmitted waves respectively. WG7 is placed just in front of the FBW to measure the incident waves on the FBW, while WG8 is placed just behind the FBW to measure the transmitted waves behind the FBW.

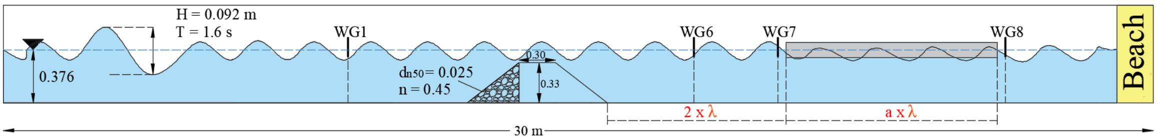

Figure 5.11: Numerical set-up of the NWT used for case 2 with four numerical wave gauges to measure the incident and transmitted waves in front and behind the SBW and the FBW respectively.

As labeled in Figure 5.11, $[a \times \lambda]$ stands for the different lengths of the FBW that will be simulated for this case. Figure 5.12 illustrates the details of these configurations of the FBW to be simulated for this case.

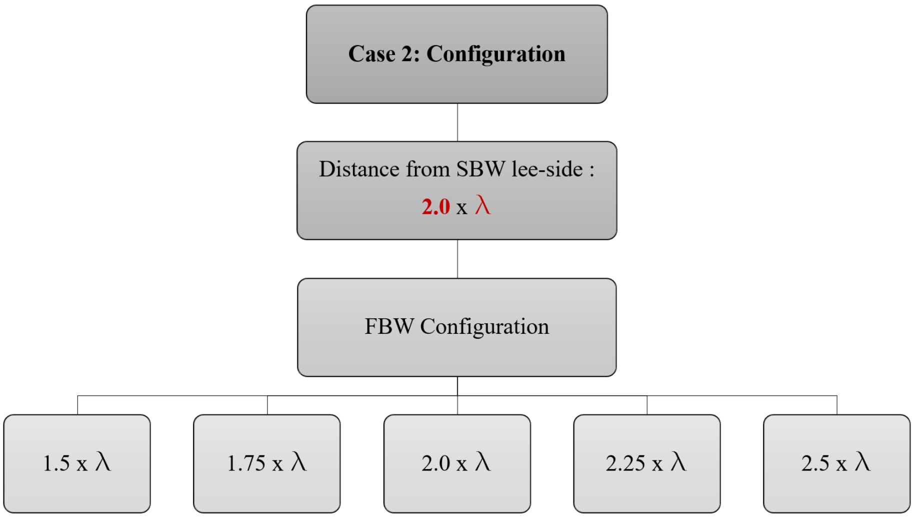

Figure 5.12: Floating breakwaters (FBWs) configurations used for case 2

5.1.2.1 Configuration 1: FBW of length 1.5λ

This is the first configuration of case 2. The floating breakwater (FBW) is placed at two times the wavelength from the lee side of the submerged breakwater (SBW) with a length of 1.5 times the wavelength.

It is clearly seen in Figure 5.13a,b, and Figure 5.14a that the free surface elevation at WG1, WG6, and WG7 is also slightly affected by the presence of the FBW due to some reflection. This same pattern in Figure 5.13a,b is more or less observed in all the other configurations of case 2. Some analysis will be presented in the following sections in terms of percentage of reduction of the free surface elevation/wave height. Owing to that, the incident wave at WG1 and the transmitted waves at WG6 will not be shown in the remaining configurations to avoid repetition. Furthermore, it is observed that the SBW alone reduces the incident wave height by approximately 40% on average for all the five configurations of case 2.

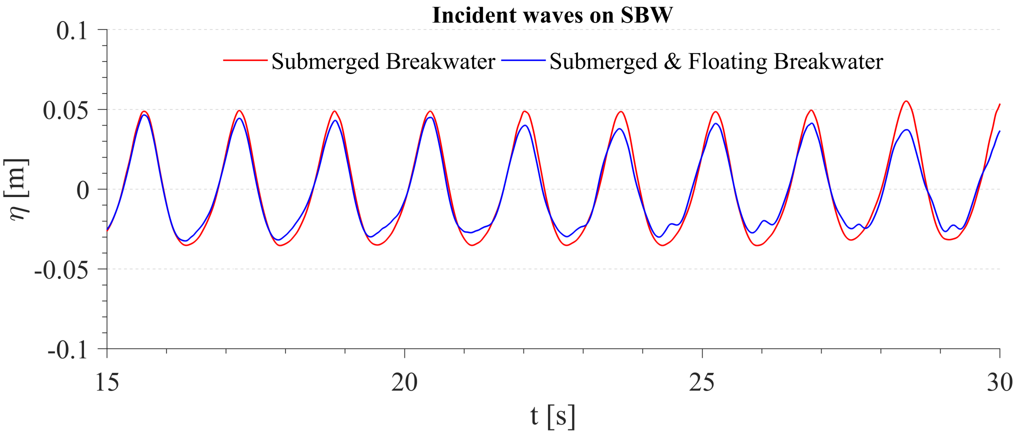

(a) Incident waves at WG1 placed at the upstream of the SBW with and without the FBW

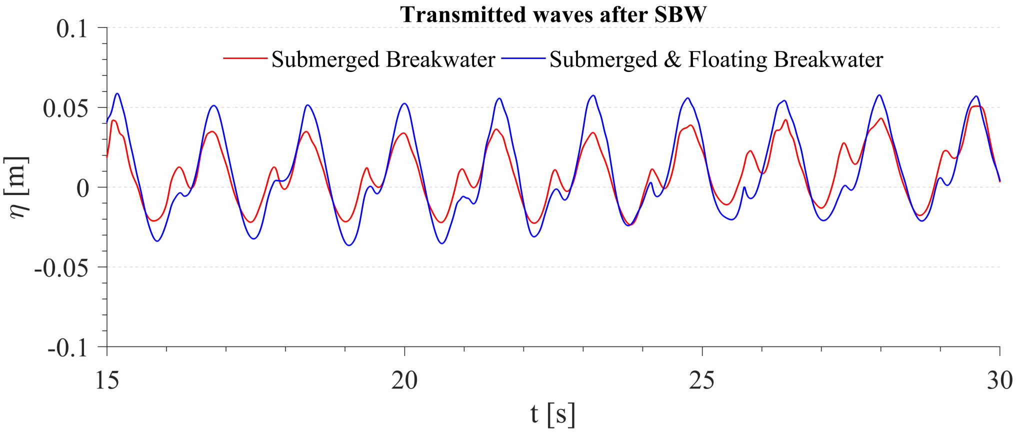

(b) Transmitted waves at WG6 placed at the downstream of the SBW with and without the FBW

Figure 5.13: Free surface elevation at WG1 and WG6 in front and behind the submerged breakwater with and without the floating breakwater on the lee side of the submerged breakwater.

Behind the FBW, the free surface elevation is largely damped out as shown in Figure 5.14b. The reduction of the incident wave height observed behind the FBW is approximately 73%. This means that the transmitted wave height across the combined submerged and floating breakwaters system is approximately 27% of the incident wave height.

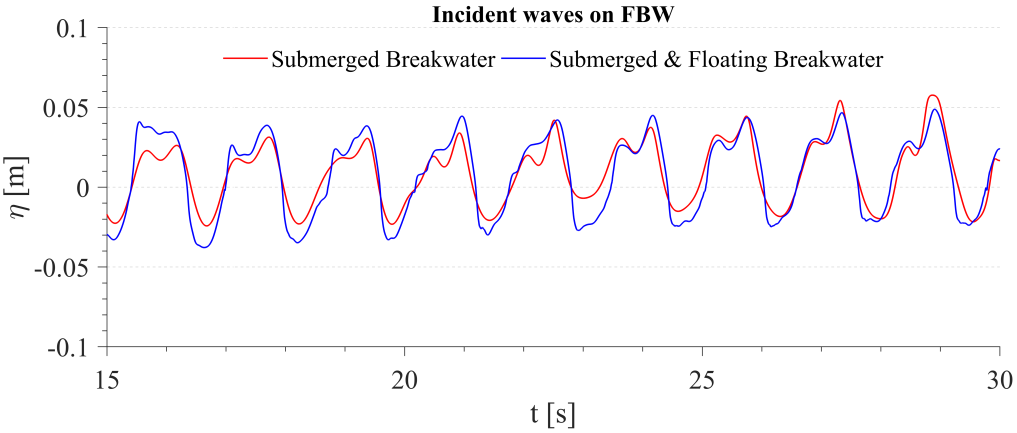

(a) Incident waves at WG7 placed just in front of the FBW with and without the FBW

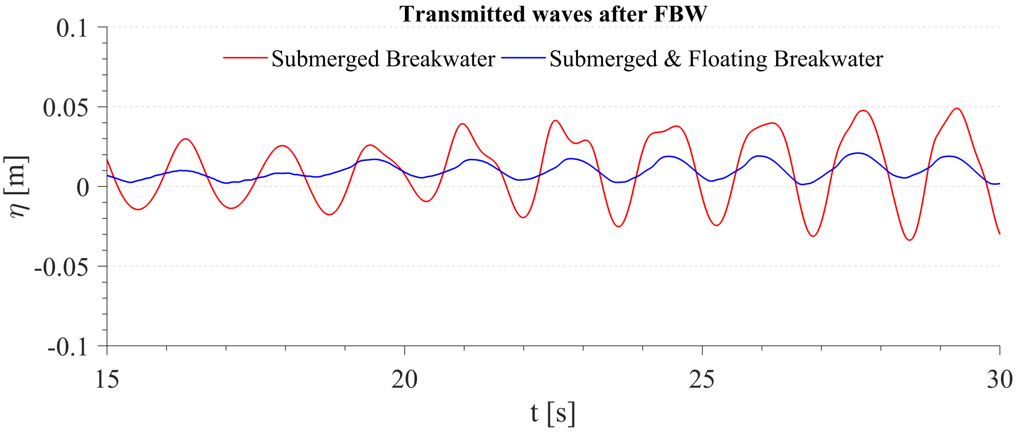

(b) Transmitted waves at WG8 placed just behind the FBW with and without the FBW

Figure 5.14: Free surface elevation at WG7 and WG8 placed just in front and behind the floating breakwater with and without the floating breakwater.

5.1.2.2 Configuration 2: FBW of length 1.75λ

Configuration 2 represents the FBW with a length of 1.75 times the wavelength located at two times the wavelength from the lee side of the SBW.

The effect of some reflection is also observed in this configuration as shown in Figure 5.15a. Furthermore, it is observed in Figure 5.15b that the presence of the FBW significantly damps out the free surface elevations at WG8 way larger than the previous configuration. This large damping of the incident wave height across the combined submerged and floating breakwaters system accounts for approximately 94%. Hence, the transmitted wave height found behind the FBW is approximately 6% for this configuration.

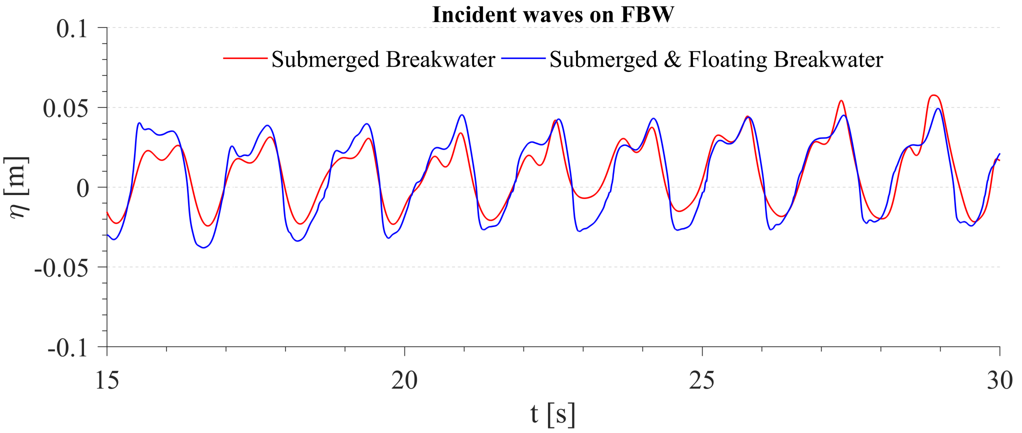

(a) Incident waves at WG7 placed just in front of the FBW with and without the FBW

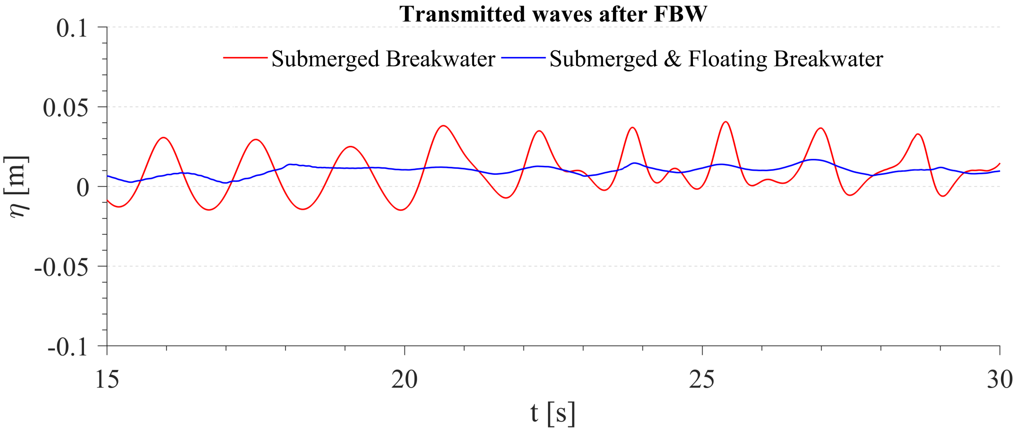

(b) Transmitted waves at WG8 placed just behind the FBW with and without the FBW

Figure 5.15: Free surface elevation at WG7 and WG8 placed just in front and behind the floating breakwater with and without the floating breakwater.

5.1.2.3 Configuration 3: FBW of length 2λ

The third configuration of case 2 represents the FBW with a length of 2.0 times the wavelength that is located at two times the wavelength from the lee side of the SBW.

Similar to the previous configurations, the free surface is seen to be largely damped out in the presence of the floating breakwater as shown in Figure 5.16b. The transmitted wave height across the combined submerged and floating breakwaters system is approximately 14% of the incident wave height. Weak reflection is also seen in this configuration as shown in Figure 5.16a.

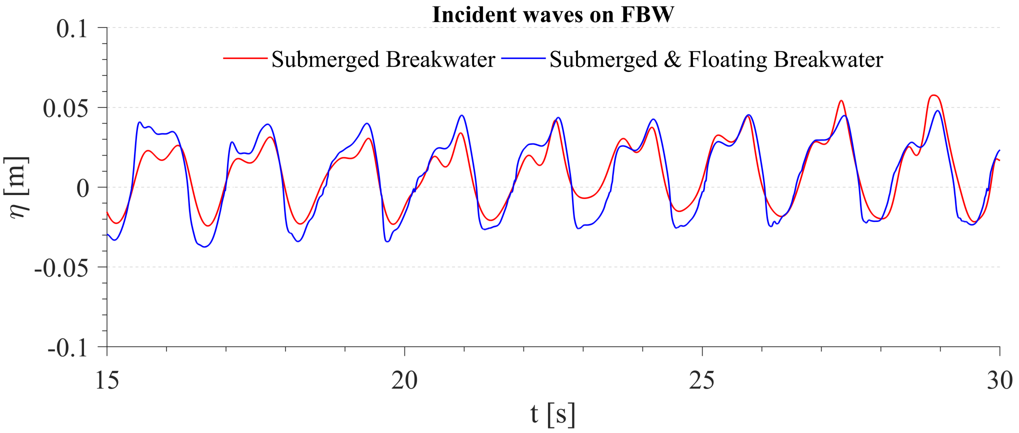

(a) Incident waves at WG7 placed just in front of the FBW with and without the FBW

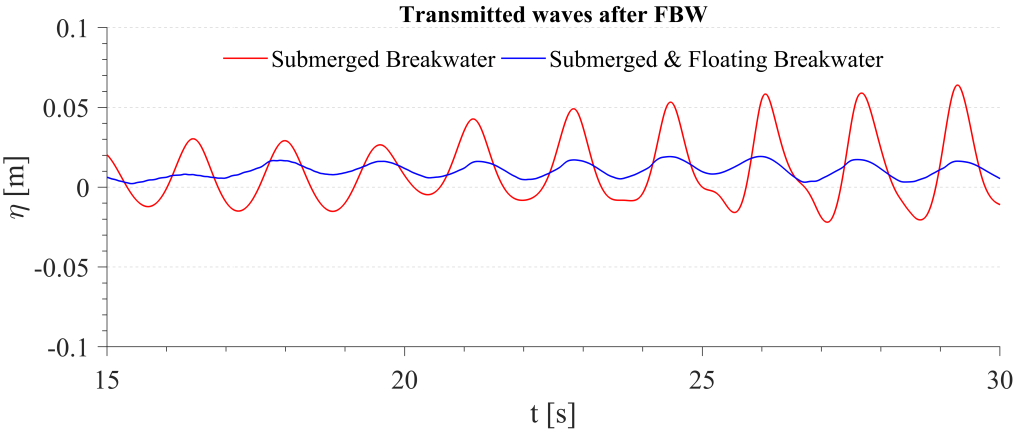

(b) Transmitted waves at WG8 placed just behind the FBW with and without the FBW

Figure 5.16: Free surface elevation at WG7 and WG8 placed just in front and behind the floating breakwater with and without the floating breakwater.

5.1.2.4 Configuration 4: FBW of length 2.25λ

Fourth configuration of case 2 represents the FBW with a length of 2.25 times the wavelength that is located at two times the wavelength from the lee side of the SBW.

The effect of the weak reflection is also noticed in this configuration as shown in Figure 5.17a. Furthermore, it is observed in Figure 5.7b that the presence of the FBW also far greatly damps out the free surface elevations at WG8. This large damping of the incident wave height across the combined submerged and floating breakwaters system accounts for roughly 95%. Hence, the transmitted wave height found behind the FBW is only 5% for this configuration. The transmitted waves of configuration 2 and this configuration are relatively the lowest in comparison to the other configurations of case 2. This, however, will be discussed in the discussion section (see section 5.1.4). .

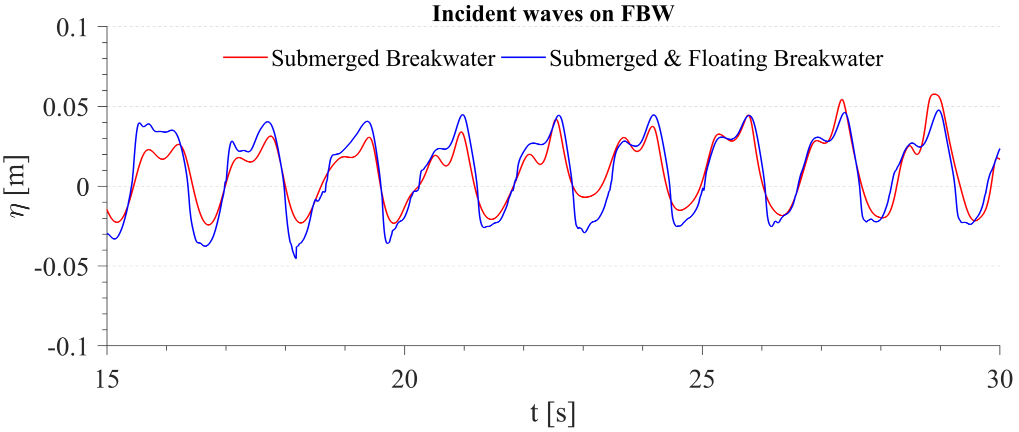

(a) Incident waves at WG7 placed just in front of the FBW with and without the FBW

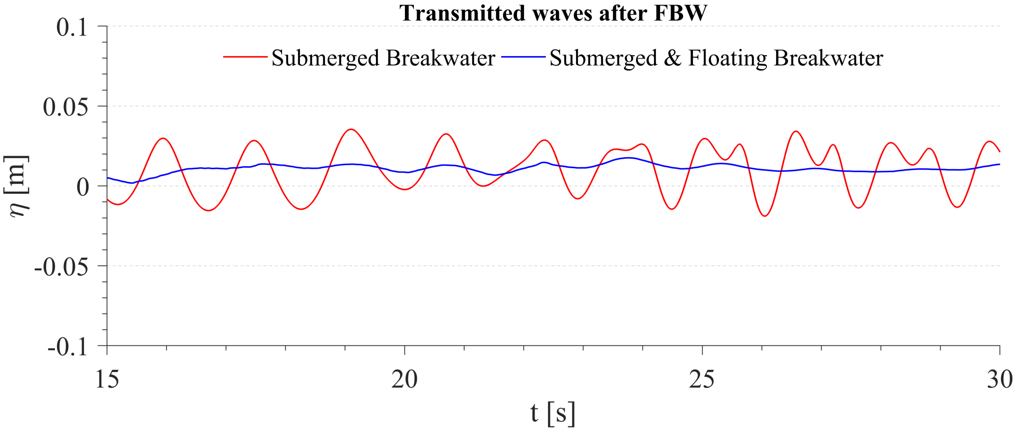

(b) Transmitted waves at WG8 placed just behind the FBW with and without the FBW

Figure 5.17: Free surface elevation at WG7 and WG8 placed just in front and behind the floating breakwater with and without the floating breakwater.

5.1.2.5 Configuration 5: FBW of length 2.5λ

The fifth configuration of case 2 is the last one. Similarly, the floating breakwater (FBW) is located at two times the wavelength from the lee side of the submerged breakwater (SBW) with a length of 2.5 times the wavelength.

The effect of the weak reflection is also observed in this configuration as shown in Figure 5.18a. In addition, it is clearly seen in Figure 5.18b that the presence of the FBW significantly damps out the free surface elevations at WG8. This large damping of the incident wave height across the combined submerged and floating breakwaters system accounts for roughly 92%. Therefore, the transmitted wave height found behind the FBW is approximately 6% for this configuration.

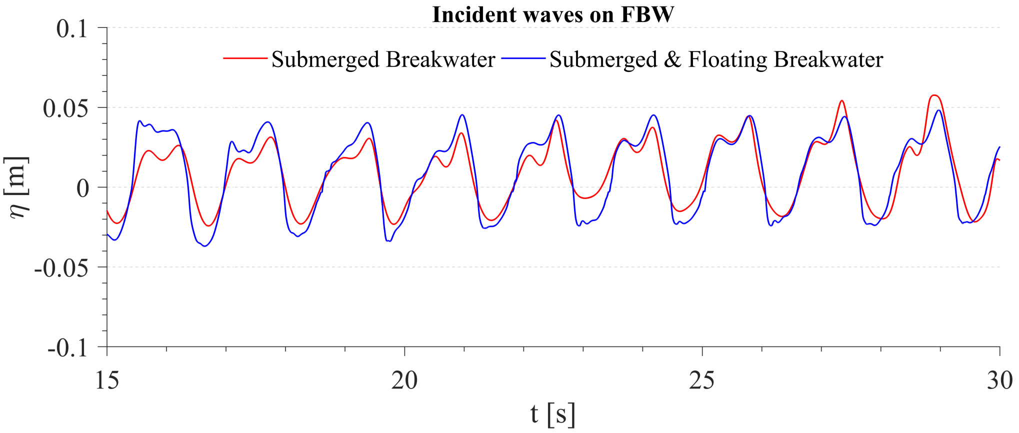

(a) Incident waves at WG7 placed just in front of the FBW with and without the FBW

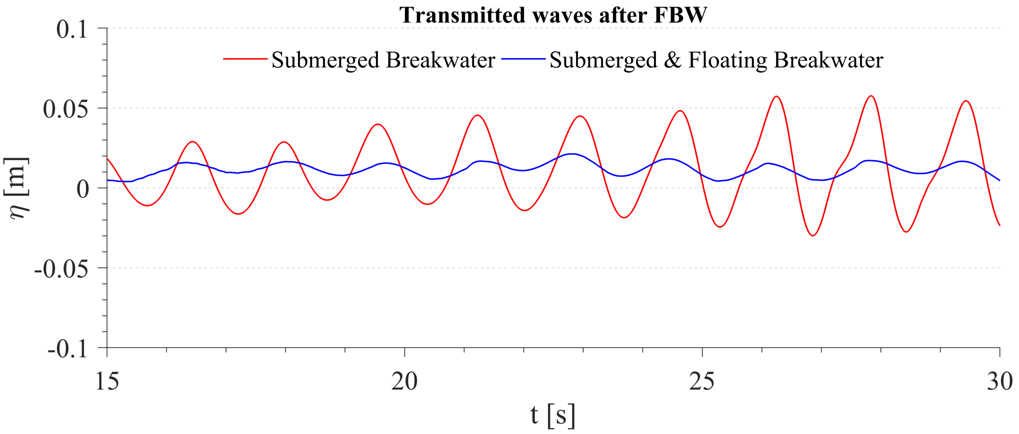

(b) Transmitted waves at WG8 placed just behind the FBW with and without the FBW

Figure 5.18: Free surface elevation at WG7 and WG8 placed just in front and behind the floating breakwater with and without the floating breakwater.

As mentioned earlier, there are some deviations in terms of percentage reduction of the incident wave height after the SBW (see Fig 5.19a) and the FBW (see Fig 5.19b) for all the aforementioned configurations as illustrated in Figure 5.19. It can be concluded from Figure 5.19a that the submerged breakwater (SBW) alone allows for a transmission of approximately 60% of the incident wave height averaged over all the configurations listed in the same Figure. However, the combined submerged and floating breakwaters system allows for transmission of approximately 12% on average of the incident wave height.

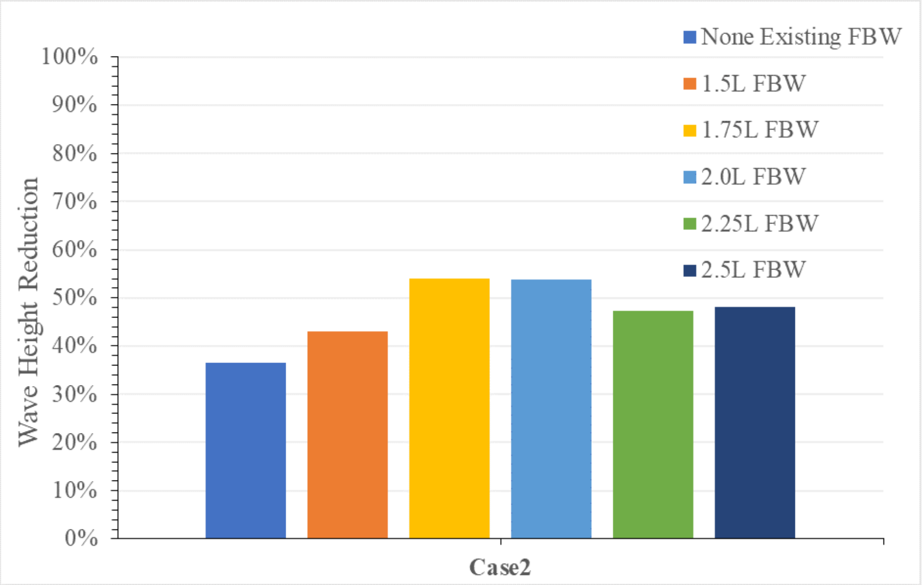

(a) Reduced wave height after the SBW with and without the FBW (L is the wavelength)

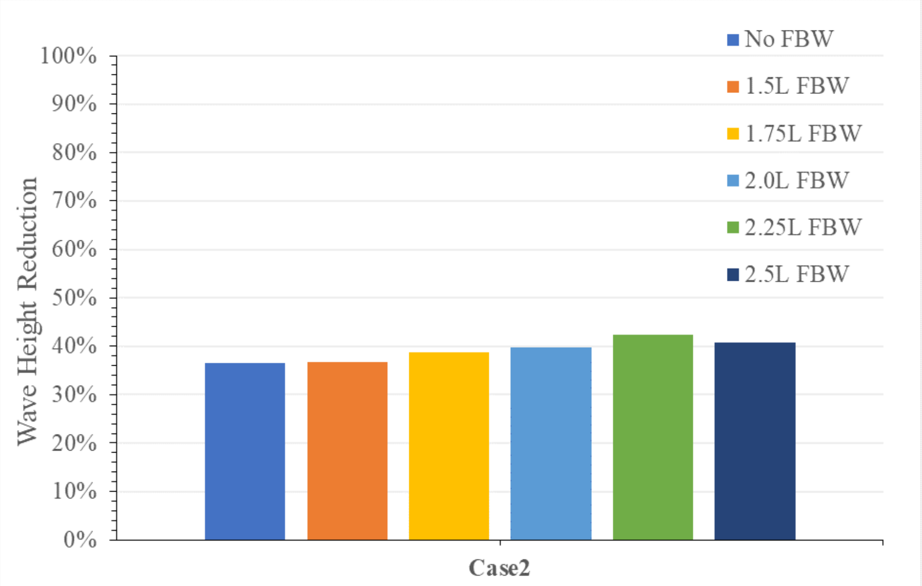

(b) Reduced wave height after the FBW with L is the wavelength)

Figure 5.19: Reduction of incident wave height after the SBW (a) and the FBW (b) in percentage.

Finally, the wave interaction with the combined submerged and floating breakwater system in the numerical wave tank is illustrated in Figure 5.20. As seen in this Figure, the thin floating breakwater is seen as a flat free surface due to its elongated dimensions.

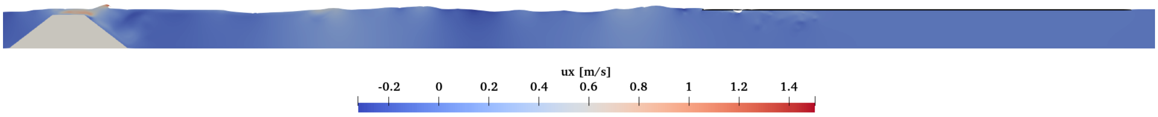

(a) Waves are breaking after the SBW

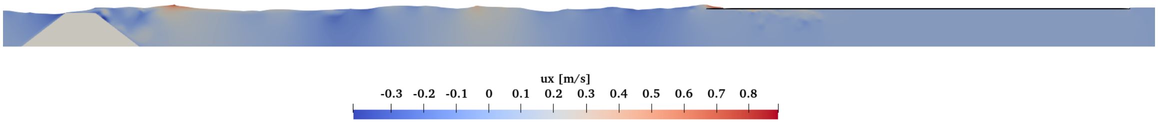

(b) Breaking waves interact with FBW

Figure 5.20: Wave interaction with the submerged porous breakwater (SBW) and the floating breakwater (FBW) placed at 2λ on the lee side of the SBW.

5.1.3 Case 3: FBW at 3λ from the SBW

This is the third case to be numerically simulated in order to investigate the effectiveness of such a combined system. As seen from Figure 5.1, the location and the configuration of the SBW are kept the same as in section 4.1.1. The FBW is placed at three times the wavelength from the lee side of the SBW and it is considered to be moored such that it is restricted from motion under the influence of the waves. The numerical domain of NWT is 30 m long, 0.005 m wide and 0.8 m high with a water depth of d= 0.376 m. The wave type and its parameters are the same as in case 1. Also, the wave generation and wave absorption method.

Similarly to the previous cases, four-wave gauges are used to obtain the free surface elevations at four different locations (see Fig 5.21). WG1 and WG6 are installed (at about the same distances shown in Figure 4.2) upstream and downstream the SBW to measure the incident and transmitted waves respectively. WG7 is placed just in front of the FBW to measure the incident waves on the FBW, while WG8 is placed just behind the FBW to measure the transmitted waves behind the FBW.

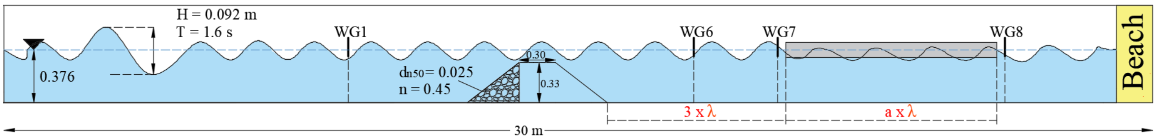

Figure 5.21: Numerical set-up of the NWT used for case 3 with four numerical wave gauges to measure the incident and transmitted waves in front and behind the SBW and the FBW respectively.

As labeled in Figure 5.21, $[a \times \lambda]$ stands for the different lengths of the FBW that will be simulated for this case. Figure 5.22 illustrates the details of these configurations of the FBW to be simulated for this case.

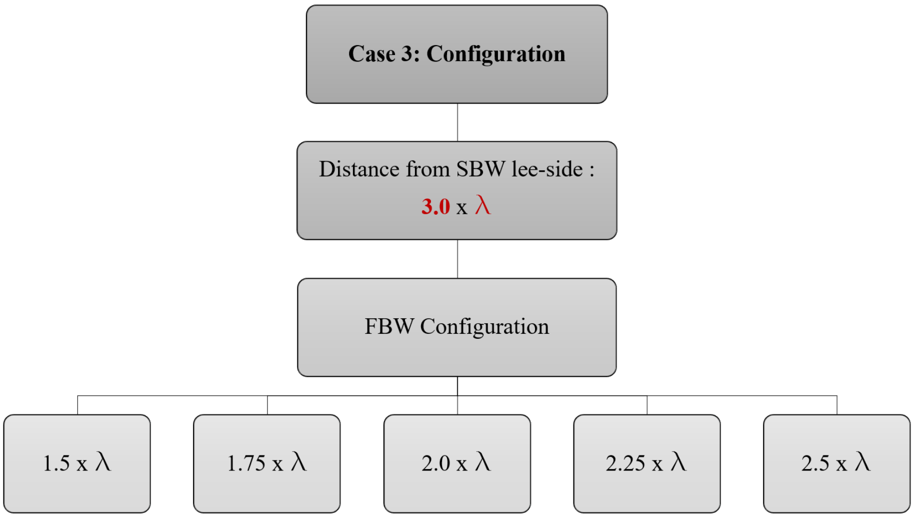

Figure 5.22: Floating breakwaters (FBWs) configurations used for case 3

5.1.3.1 Configuration 1: FBW of length 1.5λ

This is the first configuration of case 3. The floating breakwater (FBW) is placed at three times the wavelength from the lee side of the submerged breakwater (SBW) with a length of 1.5 times the wavelength.

It is distinctly seen in Figure 5.23a,b, and Figure 5.23a that the free surface elevation at WG1, WG6, and WG7 is also partly affected by the presence of the FBW due to some reflection. Like the previous cases, the same pattern in Figure 5.23a,b is more or less observed in all the other configurations of case 2. Some analysis will be presented in the following sections in terms of percentage of reduction of the free surface elevation/wave height. Because of that, the incident wave at WG1 and the transmitted waves at WG6 will not be shown in the remaining configurations to avoid repetition. Further, it is observed that the SBW alone reduces the incident wave height by approximately 41% on average for all the five configurations of case 3.

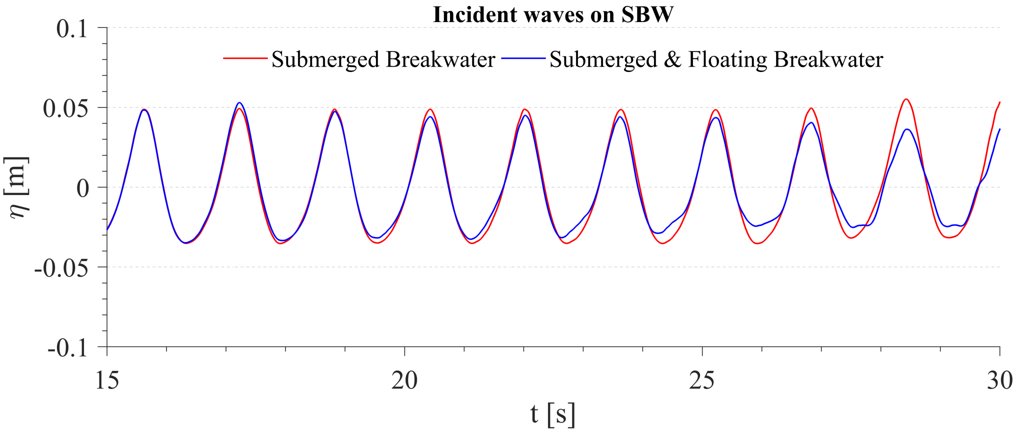

(a) Incident waves at WG1 placed at the upstream of the SBW with and without the FBW

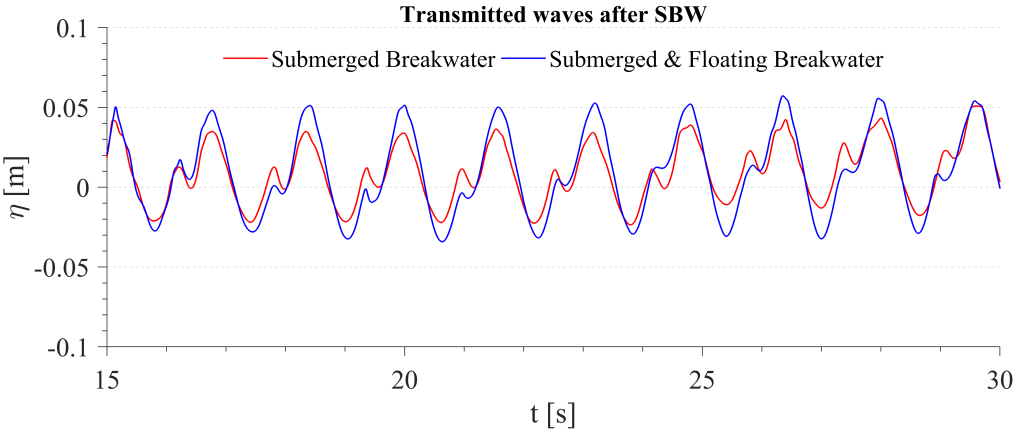

(b) Transmitted waves at WG6 placed at the downstream of the SBW with and without the FBW

Figure 5.23: Free surface elevation at WG1 and WG6 in front and behind the submerged breakwater with and without the floating breakwater on the lee side of the submerged breakwater.

Behind the FBW, the free surface elevation is largely damped out as shown in Figure 5.24b. The reduction of the incident wave height observed behind the FBW is approximately 81%. This means that the transmitted wave height across the combined submerged and floating breakwaters system is approximately 19% of the incident wave height.

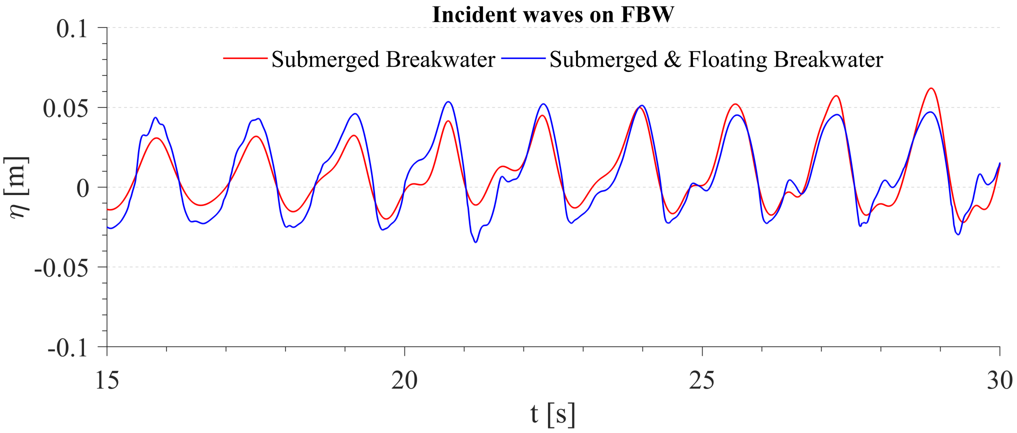

(a) Incident waves at WG7 placed just in front of the FBW with and without the FBW

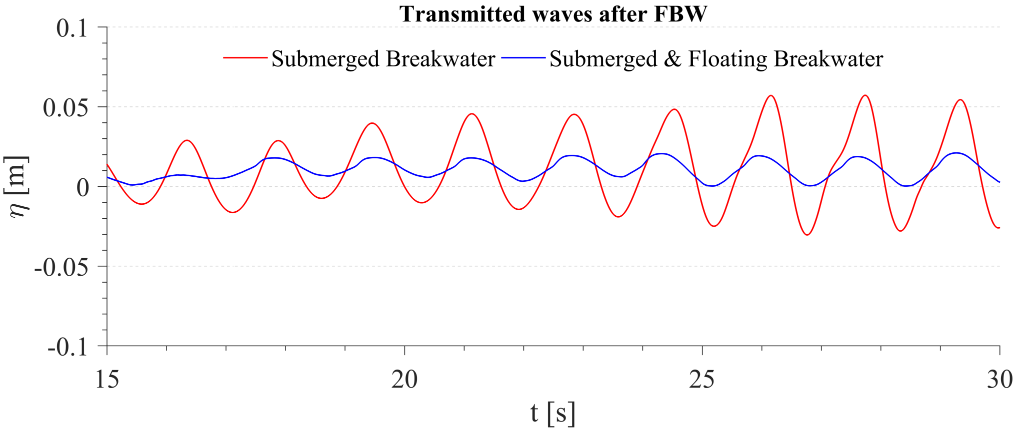

(b) Transmitted waves at WG8 placed just behind the FBW with and without the FBW

Figure 5.24: Free surface elevation at WG7 and WG8 placed just in front and behind the floating breakwater with and without the floating breakwater.

5.1.3.2 Configuration 2: FBW of length 1.75λ

Configuration 2 represents the FBW with a length of 1.75 times the wavelength located at three times the wavelength from the lee side of the SBW.

The effect of the weak reflection is also observed in this configuration as shown in Figure 5.25a. In addition, it is seen in Figure 5.25b that the presence of the FBW significantly damps out the free surface elevations at WG8 much larger than the former configuration. This large damping of the incident wave height across the combined submerged and floating breakwaters system accounts for approximately 96%. Hence, the transmitted wave height found behind the FBW is only 6% for this configuration.

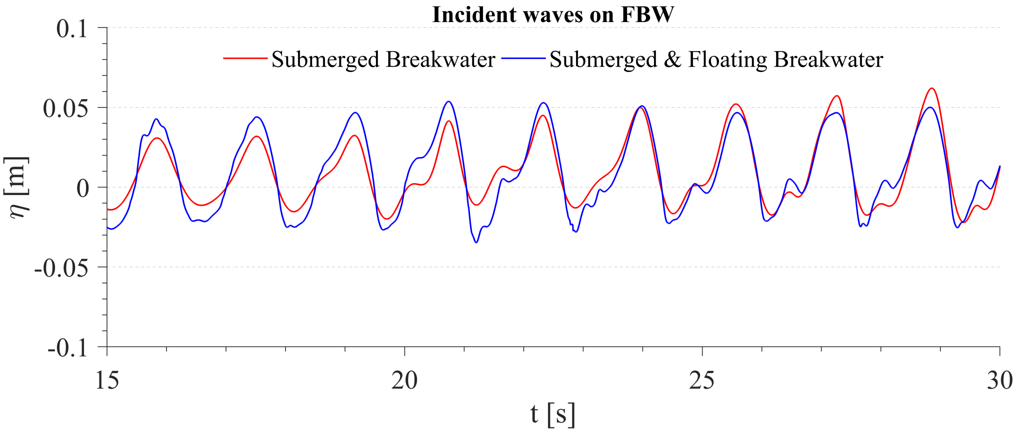

(a) Incident waves at WG7 placed just in front of the FBW with and without the FBW

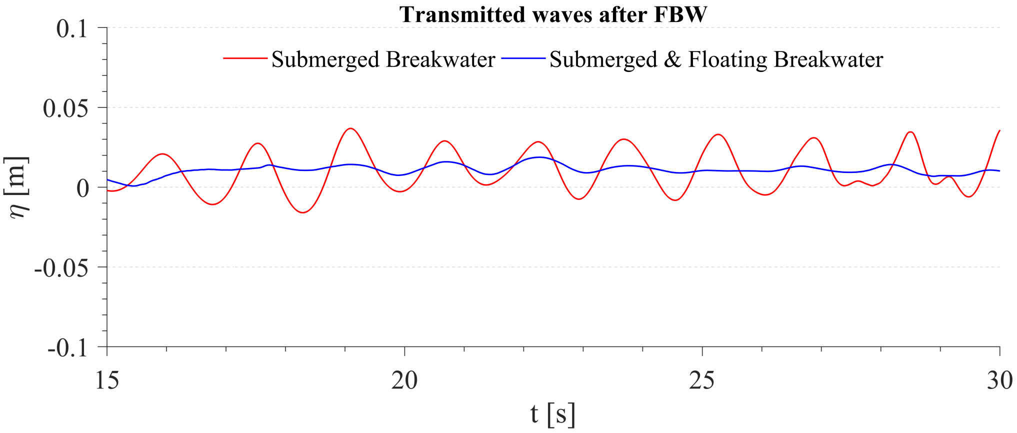

(b) Transmitted waves at WG8 placed just behind the FBW with and without the FBW

Figure 5.25: Free surface elevation at WG7 and WG8 placed just in front and behind the floating breakwater with and without the floating breakwater.

5.1.3.3 Configuration 3: FBW of length 2λ

The third configuration represents the FBW with a length of 2.0 times the wavelength located at three times wavelength from the lee side of the SBW.

Similar to the previous configuration 2, the free surface is seen to be significantly damped out in the presence of the floating breakwater as shown in Figure 5.26b. The transmitted wave height across the combined submerged and floating breakwaters system is about 7% of the incident wave height. Further, some reflection effect is also seen in this configuration as shown in Figure 5.26a.

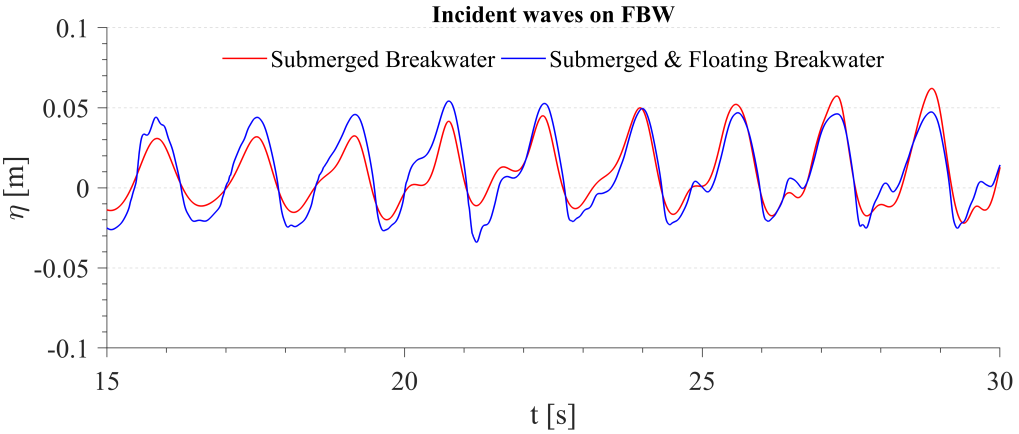

(a) Incident waves at WG7 placed just in front of the FBW with and without the FBW

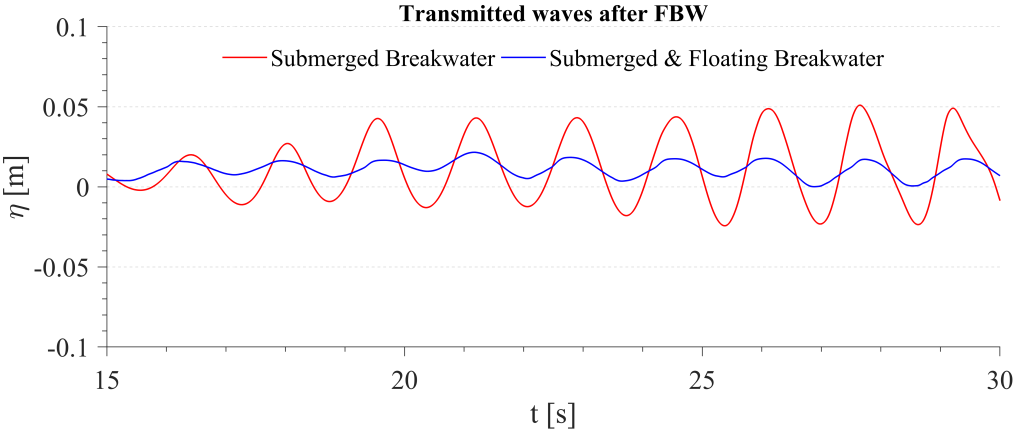

(b) Transmitted waves at WG8 placed just behind the FBW with and without the FBW

Figure 5.26: Free surface elevation at WG7 and WG8 placed just in front and behind the floating breakwater with and without the floating breakwater.

5.1.3.4 Configuration 4: FBW of length 2.25λ

This is the fourth configuration of case 3 which represents the FBW with a length of 2.25 times the wavelength that is located at three times the wavelength from the lee side of the SBW.

The effect of the weak reflection is also noticed in this configuration as shown in Figure 5.27a. Furthermore, it is seen in Figure 5.27b that the presence of the FBW also far greatly damps out the free surface elevations at WG8 which is more or less similar to the second configuration of case 3. This large damping of the incident wave height across the combined submerged and floating breakwaters system accounts for approximately 96%. Thus, the transmitted wave height found behind the FBW is only 4% for this configuration. The transmitted waves of this configuration and configuration 2 are relatively the lowest in comparison to the other configurations of case 3. This, however, will be discussed in the discussion section (see section 5.1.4).

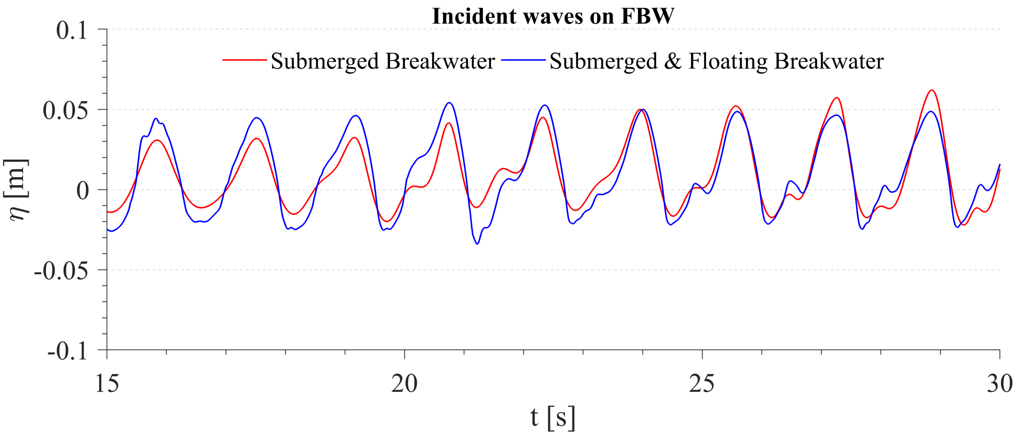

(a) Incident waves at WG7 placed just in front of the FBW with and without the FBW

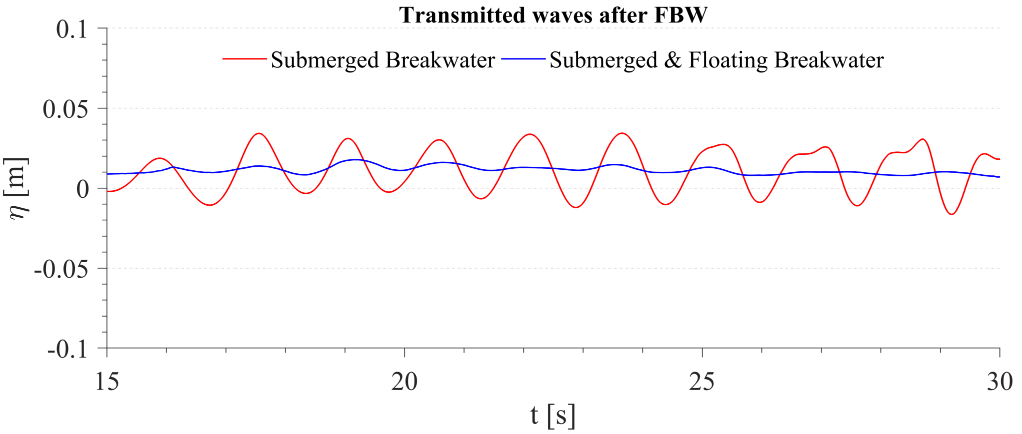

(b) Transmitted waves at WG8 placed just behind the FBW with and without the FBW

Figure 5.27: Free surface elevation at WG7 and WG8 placed just in front and behind the floating breakwater with and without the floating breakwater.

5.1.3.5 Configuration 5: FBW of length 2.5λ

This is the last configuration of case 3. The floating breakwater (FBW) is located at three times the wavelength from the lee side of the submerged breakwater (SBW) with a length of 2.5 times the wavelength.

Similar to the previous configuration, the free surface is seen to be greatly damped out in the presence of the floating breakwater as shown in Figure 5.28b. The transmitted wave height across the combined submerged and floating breakwaters system is about 8% of the incident wave height. This means that 92% of the incident wave height across this combined system has successfully died out. Besides, some weak reflection effect is also seen in this configuration as shown in Figure 5.28a.

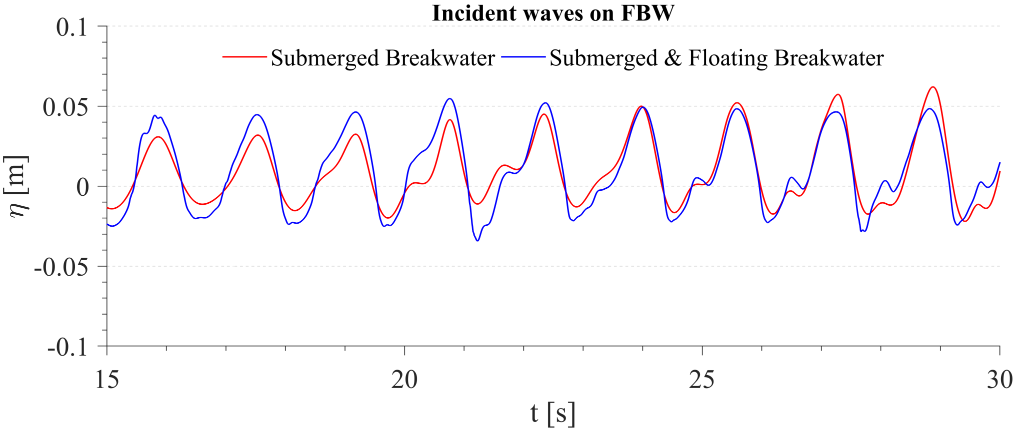

(a) Incident waves at WG7 placed just in front of the FBW with and without the FBW

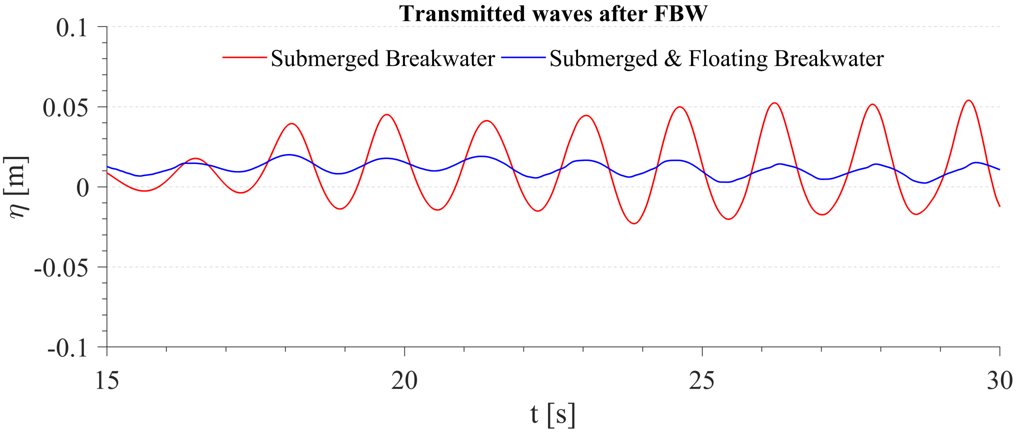

(b) Transmitted waves at WG8 placed just behind the FBW with and without the FBW

Figure 5.28: Free surface elevation at WG7 and WG8 placed just in front and behind the floating breakwater with and without the floating breakwater.

There are some deviations in terms of percentage reduction of the incident wave height after the SBW (see Fig 5.29a) and the FBW (see Fig 5.29b) for all the aforementioned configurations as illustrated in Figure 5.29 as mentioned earlier. From Figure 5.29a, it can be deduced that the submerged breakwater (SBW) alone allows for a transmission of approximately 60% of the incident wave height averaged over all the configurations listed in the same Figure. However, the combined submerged and floating breakwaters system allows for a transmission of approximately 8% on average of the incident wave height.

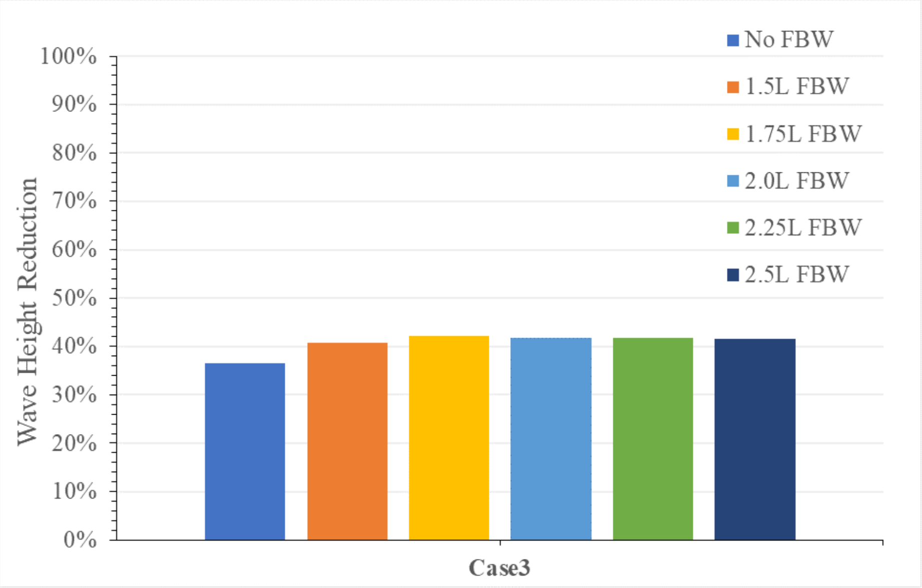

(a) Reduced wave height after the SBW with and without the FBW (L is the wavelength)

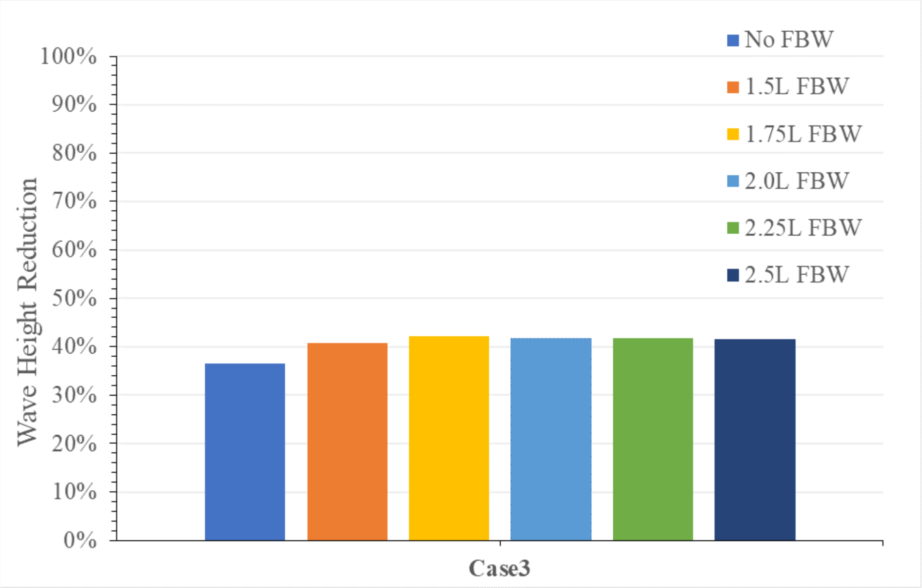

(b) Reduced wave height after the FBW with L is the wavelength)

Figure 5.29: Reduction of incident wave height after the SBW (a) and the FBW (b) in percentage.

Finally, the wave interaction with the combined submerged and floating breakwater system in the numerical wave tank is illustrated in Figure 5.30. As seen in this Figure, the thin floating breakwater is seen as a flat free surface due to its elongated dimensions.

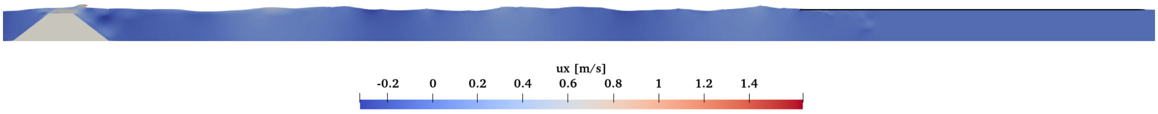

(a) Waves are breaking after the SBW

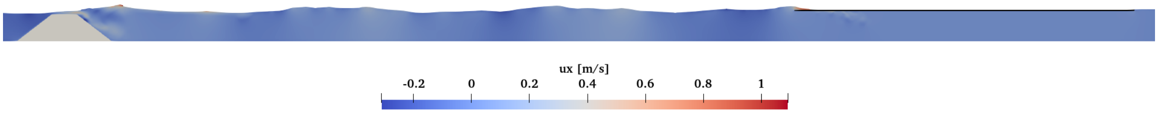

(b) Breaking waves interact with FBW

Figure 5.30: Wave interaction with the submerged porous breakwater (SBW) and the floating breakwater (FBW) placed at 3λ on the lee side of the SBW.

5.1.4 Discussion on the Wave Transmission across the Combined System

In this section, the incident and the transmitted wave height for the combined system of the breakwaters are presented individually for each subsystem with more focus on the transmission coefficients behind the FBW.

5.1.4.1 Incident vs. Transmitted wave Height

In the previous sections, the free surface elevation and the percentage reduction of the incident wave height on SBW and FBW are presented separately to illustrate the effect of the different configurations of the FBW for the three cases described in section 5.1. However, in this section, the bulk effect for each case is presented and discussed.

The incident wave height on the SBW subsystem for all the three cases is close to the value of the original wave height ($H_s = 0.092$ m) imposed in the numerical model as shown in Figure 5.31a. The reason behind this observation might be due to some reflection caused by the SBW subsystem. This reflection, in this case, results in a partially destructive interference with the incoming wave which yields a partially damped incident wave height. Furthermore, the pattern of the incident wave height suffers some deformation. This might be due to the presence of the FBW which can produce some reflection as well. As shown in Figure 5.31a , it is observed that the larger the FBW length the more deformed the pattern becomes. Also, the effect of the distance between these two subsystem breakwaters on the incident wave height can be seen (see Fig 5.31a). The largest effect can be seen in the trend of the incident wave height of case 1 and it is gradually reduced with the increase of this distance.

With regard to the transmitted wave height after the SBW, Figure 5.31b clearly shows a distinct reduction of the incident wave height (Fig 5.31a) with more than 40% on average. On the other hand, the trend of the transmitted wave for the three different cases shows some fluctuation. This could be due to the complex the wave transformation processes behind the SBW and also due to the presences of destructive/constructive wave interference caused by some wave reflection by the FBW.

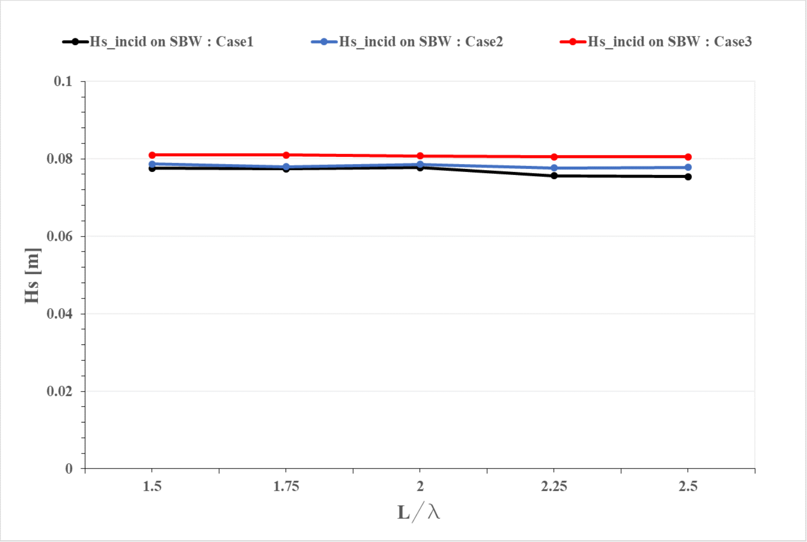

(a) Incident wave on the SBW subsystem

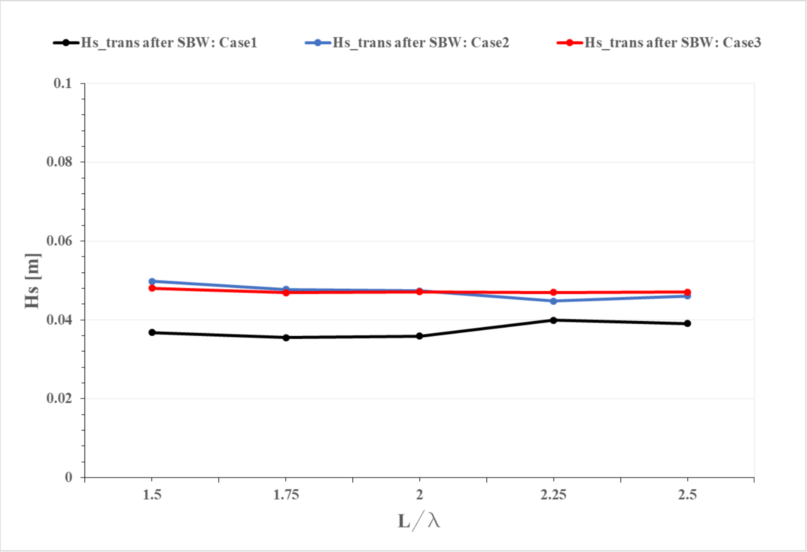

(b) Transmitted wave after the SBW subsystem

Figure 5.31: Incident and Transmitted wave height across the submerged breakwater subsystem for the three cases.

Figure 5.32 illustrates the incident and the transmitted waves across the floating breakwater subsystem. Interestingly, Figure 5.32b shows a remarkable reduction of more than 90% , on average, of the incident wave height for this combination. Finally, the fluctuations and the deformities of the incident and transmitted wave height observed in Figure 5.32 can be argued with the same reasoning mentioned above.

These results obtained in Figure 5.31 and Figure 5.32 demonstrate the ability of REEF3D to capture not only the wave breaking on and after the SBW which is featured by the reduction of the incoming wave height (see Fig 5.31b and and Fig 5.32b), but also the complex nonlinear interactions between the primary and the secondary waves after the SBW which is featured by backward energy transfer leading to an increase of the wave height in front of the FBW (see Fig 5.32a).

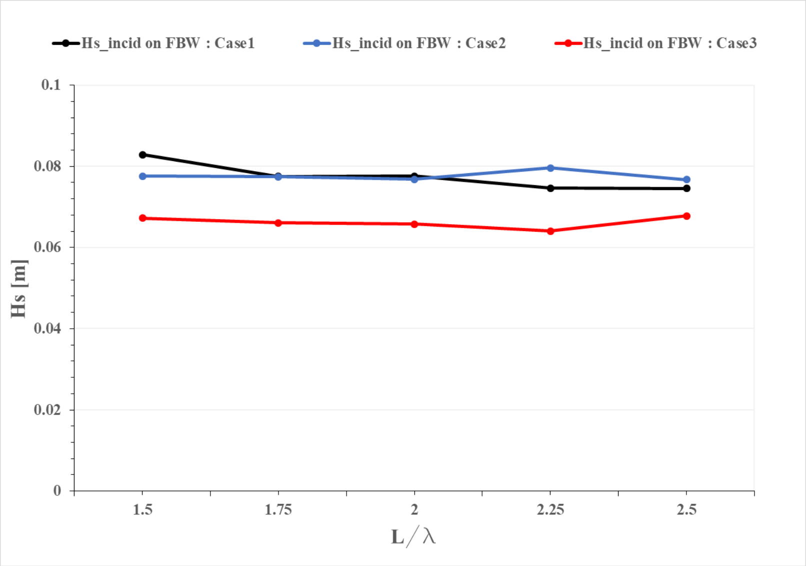

(a) Incident wave on the FBW subsystem

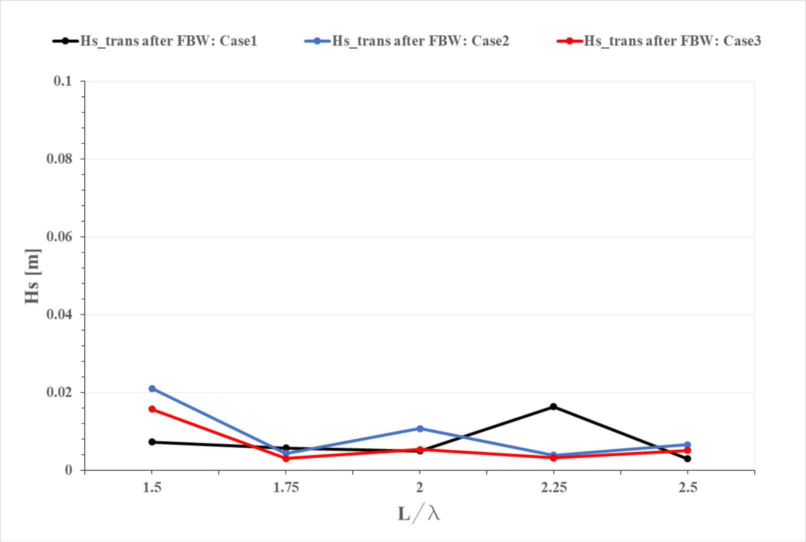

(b) Transmitted wave after the FBW subsystem

Figure 5.32: Incident and Transmitted wave height across the floating breakwater subsystem for the three cases.

5.1.4.2 Transmission coefficient

Technically, the efficiency of the floating breakwater is often quantified by their wave transmission coefficients. Therefore, the transmission coefficient versus the ratio of FBW length to wavelength (L/λ) is investigated. Generally, all the cases yield an effective wave transmission coefficient ($K_t < 0.5$) except for 1.5 FBW ratio of case 3 as shown in Figure 5.33.

In addition, Figure 5.33 reveals some interesting features can be summed up as follows:

- The effect of the distance between the SBW and the FBW subsystems can be clearly seen in Figure 5.33; the larger the distance (i.e. case 3 with the largest distance) the larger the wave transmission coefficient (K_t) and vice versa.
- Although the overall trend of the wave transmission coefficient (K_t) in Figure 5.33 suffers from some fluctuations, the effect of the FBW subsystem length can still be observed to some extent. The reason behind these fluctuations in Figure 5.33 has to do with the presence of some reflections in the overall signal caused by the FBW subsystem which, in turn, disturb the overall trend of the wave transmission coefficient for each case. Nonetheless, an interesting fact can be concluded from Figure 5.33 as such; for all the three cases, the FBWs with the ratio of FBW length to wavelength (L/λ) equals 1.75 and 2.5 yields the lowest wave transmission coefficient (K_t) for all the three cases.

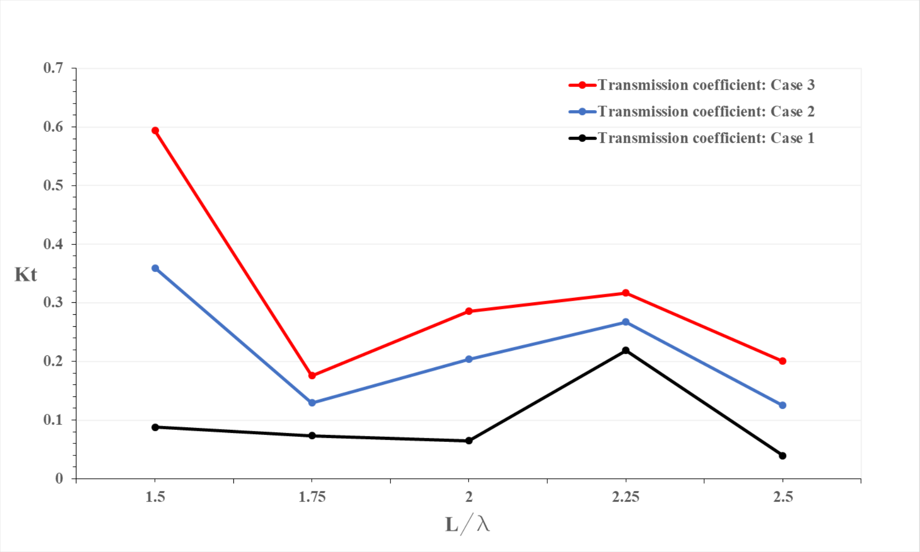

Figure 5.33: Transmission coefficients vs. the ratios of FBW length to wavelength (L/λ) for the three cases.

5.1.4.3 Sensitivity analysis on the Optimum Configuration

In the design of Floating Breakwaters, the ratio of FBW length to wavelength (L/λ) has to be 2 or larger to achieve small wave transmission coefficient (i.e. $K_t < 0.5$) behind the FBWs (see Fig 1.3). However, in this study, it was found out that a ratio of 1.75 (see Fig 5.33) can result in a very small wave transmission coefficient as discussed in section 5.1.4.2.

However, this result raises the question of how accurate this 1.75 ratio can be. To answer that, a sensitivity analysis is carried out. Before going to the details, the accuracy of the obtained wave transmission coefficients in Figure 5.33 is further investigated.

To the best of the researchers' knowledge, no experimental data in the literature are available to make a comparison for such breakwaters combination. Therefore, the mean and the standard deviation for each incident and transmitted wave signal for all the five different configurations of each case is calculated. On average, a standard deviation of 0.021 is calculated for the incident wave height on the FBW for all the three cases, while a standard deviation of 0.005 is obtained for the transmitted wave height after the FBW for all the three cases. As shown in Figure 5.33, the shaded areas show the upper and the lower bands based on these standard deviations calculated for each case's configuration. For Figure 5.34a and Figure 5.34b, it is clearly seen that the scatter around the mean is relatively small compared to the scatter of Figure 5.33c.

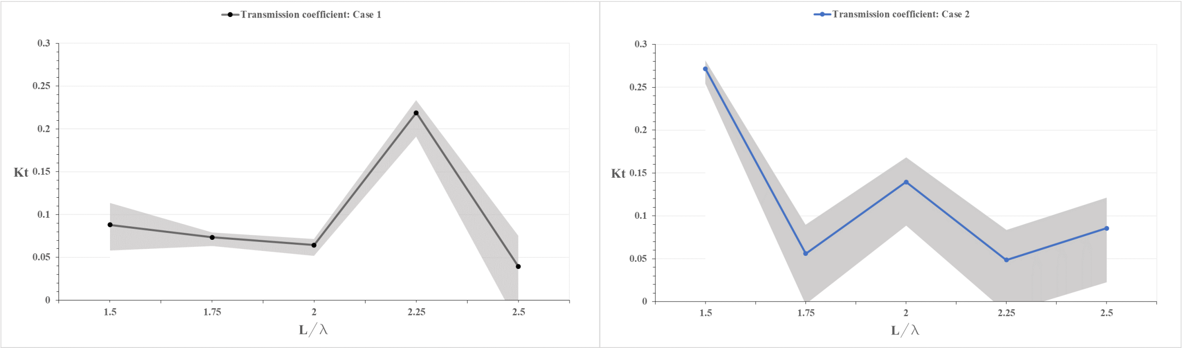

(a) The wave transmission coefficient of Case 1 (b) The wave transmission coefficient of Case 2

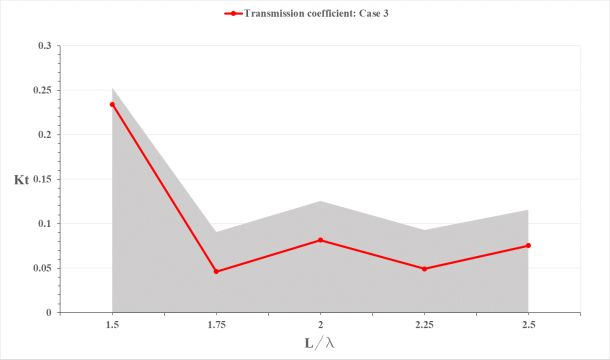

(c) The wave transmission coefficient of Case 3

Figure 5.33: The accuracy of the wave transmission coefficient signal obtained for the three cases using REEF3D.

In order to evaluate either 1.75 ratio of L/λ is optimum for all the cases or not, a sensitivity analysis is carried out on a lower ratio of L/λ (i.e. 1.6). K_t values are determined for this scenario and it was observed that the transmission coefficients at 1.75 are still lower for all the cases as clearly shown in Figure 5.34.

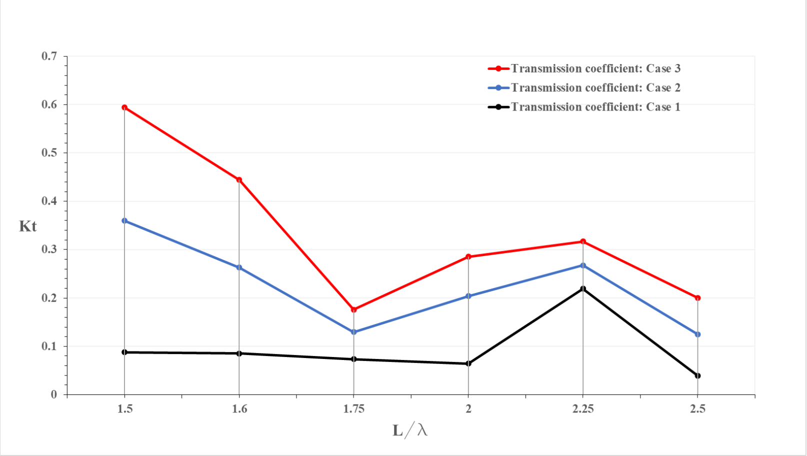

Figure 5.34: Transmission coefficients vs. the ratios of FBW length to wavelength (L/λ) for the three cases.

To sum up, this study uses the open-source CFD model REEF3D to simulate the interaction of regular waves with the Submerged Porous Breakwater (SBW) in combination with the Floating Breakwater (FBW). It is concluded that an effective reduction of more than 90% of the incident wave height can be achieved for this combined breakwaters system. Besides, it is found out that 1.75 FBW length to wavelength (L/λ) ratio produces a very low transmission coefficient (K_t). Further, an effective distance of 1-2 wavelength between the SBW and the FBW subsystems can also result in lower transmission coefficients (K_t).

Chapter 6

Conclusions and Recommendations

6.1 Conclusions

The aim of this thesis is to simulate the interaction of irregular and regular waves with a barred beach profile and submerged porous breakwater in combination with a floating breakwater using the open-source CFD model, REEF3D. This CFD model is based on the RANS equations coupled with the level set method and the $k - \omega$ turbulence model.

First, the simulation of irregular wave breaking over a mild-slope barred beach profile which has a breaker bar and a surf zone trough is validated in chapter 3. The wave reconstruction method is used to generate irregular waves that are identical to a wave signal close to the wave board. Two irregular wave cases are simulated. Their numerical results are verified against the experimental data. The comparisons provide a good agreement between the computed results and the experimental data, showing that REEF3D model is capable of capturing the dominant features of the evolution of the wave breaking process, both in the shoaling region and the surf zone.

In chapter 4, the simulation of regular wave interaction with a submerged porous breakwater (SBW) is performed. The simulation is conducted using the numerical model REEF3D which uses the Volume-averaged Reynolds-averaged Navier-Stokes (VRANS) equations to resolve the porous flow. The numerical model is first validated for wave interaction with a submerged porous structure using experimental data. Comparisons for the free surface elevation between the numerical results and the experimental data show a good match with very small RMSE values. Besides, the evolution of flow through the porous media have been correctly modelled, confirming that the model is capable of simulating a complex wave interaction with porous structures.

Finally, the validated model from chapter 4 is then used to simulate the regular wave interaction with a combination of the submerged breakwater and the floating breakwater in chapter 5. Three different cases are investigated with three different distances from the lee side of the submerged porous breakwater (SBW) to the floating breakwater (FBW). For each case, five different configurations related to the geometry of the FBW are simulated. It is found out that an effective reduction of more than 90%, on average, of the incident wave height, can be achieved for this combined breakwaters system. This means that a transmission coefficient (K_t) of less than 10% is calculated across this combination. Besides, it is arguably demonstrated that FBW length to wavelength (L/λ) ratio of 1.75 produces a very low transmission coefficient (K_t) with an effective distance of 1-2 wavelength between the SBW and the FBW subsystems. This, in return, demonstrates the potentiality to provide a solution for more calm conditions in the coastal zones without spoiling the landscape of the coastal developments.

6.2 Recommendations

The study presented in this thesis shows that REEF3D can be applied to various problems such as shoaling and breaking of irregular waves in the coastal zone, regular wave interaction with a submerged porous breakwater and the interaction of regular waves with a submerged porous breakwater in combination with a floating breakwater with promising results.

The focus of this research was mainly to investigate the possibility of using the combination of a submerged porous breakwater with a floating breakwater as an innovative coastal protection system that can provide adequate calm conditions in the coastal zones with minimum visual impact. However, many simplifications are made throughout this study. Therefore, it is recommended to perform further research to address the following issues:

- In the present study, regular waves were used in the numerical simulations. However, waves, in reality, are irregular in real sea state. Therefore, the irregular wave generation and the corresponding wave interaction with the aforementioned coastal structures need to be studied.
- The effect of the relative submergence parameter (freeboard/incident wave height), the relative width parameter (crest-width /wavelength), the effect of the porosity and the slope of the breakwater parameters, and wave steepness parameter

(H_i/gT^2) were not studied in this research. However, these structure-wave related parameters can greatly influence the wave transmission coefficient. Therefore, it is of great importance to further investigate these parameters to understand their relative effect on wave transmission.

- The effect of the wave reflection was clearly seen on the magnitude of the wave transmission coefficients as discussed in previous sections. Therefore, it is recommended to further the present study to investigate the extent of the wave reflection signal on the transmitted waves.
- The simulation of the combination of the submerged porous breakwater with the floating breakwater is performed in a 2D Numerical Wave Tank (NWT). In this case, the three-dimensional effects such as diffraction of waves around the floating breakwater are not considered. This diffraction can either reinforce waves or cancel them out, resulting in a complex wave pattern. Therefore, it is recommended to investigate the magnitude of diffraction on the transmitted waves.
- The floating breakwater was simulated as a thin flat plate. The influence of the anchoring system including the six degrees of freedom and the mooring forces was not studied. Therefore, it is recommended to study such effect in order to model the bulk effects of a full-wave spectrum on the wave transmission.

Bibliography

[1] M. D. Safari *et al.*, "A short review of submerged breakwaters", in *MATEC Web of Conferences*, EDP Sciences, vol. 203, 2018, p. 01 005.

[2] L. Z. Hales, "Floating breakwaters: State-of-the-art literature review.", Coastal Engineering Research Centre Fort Belvoir Va, Tech. Rep., 1981.

[3] A. Sharifahmadian, *Numerical Models for Submerged Breakwaters: Coastal Hydrodynamics and Morphodynamics.* Butterworth-Heinemann, 2015.

[4] S. Kuznetsov and Y. Saprykina, "Combination of submerged structures and floating breakwater for coastal protection", in *Coastal Structures 2011: (In 2 Volumes)*, World Scientific, 2013, pp. 48–58.

[5] G. J. Schiereck, *Introduction to bed, bank and shore protection.* CRC Press, 2017.

[6] M. R. A. Van Gent, "Stationary and oscillatory flow through coarse porous media", *Communications on hydraulic and geotechnical engineering, No. 1993-09*, 1993.

[7] M. Van Gent, "Porous flow through rubble-mound material", *Journal of waterway, port, coastal, and ocean engineering*, vol. 121, no. 3, pp. 176–181, 1995.

[8] I. J. Losada, J. L. Lara, and M. del Jesus, "Modeling the interaction of water waves with porous coastal structures", PhD thesis, American Society of Civil Engineers, 2016.

[9] B. Jensen, N. G. Jacobsen, and E. D. Christensen, "Investigations on the porous media equations and resistance coefficients for coastal structures", *Coastal Engineering*, vol. 84, pp. 56–72, 2014.

[10] A. Sasikumar, A. Kamath, O. Musch, A. E. Lothe, and H. Bihs, "Numerical study on the effect of a submerged breakwater seaward of an existing breakwater for climate change adaptation", in *ASME 2018 37th International Conference on Ocean, Offshore and Arctic Engineering*, American Society of Mechanical Engineers, 2018, V07AT06A027–V07AT06A027.

[11] C. K. Sollitt and R. H. Cross, “Wave transmission through permeable breakwaters”, in *Coastal Engineering 1972*, 1973, pp. 1827–1846.

[12] M. del Jesus, J. L. Lara, and I. J. Losada, “Three-dimensional interaction of waves and porous coastal structures: Part i: Numerical model formulation”, *Coastal Engineering*, vol. 64, pp. 57–72, 2012.

[13] J. Dai, C. M. Wang, T. Utsunomiya, and W. Duan, “Review of recent research and developments on floating breakwaters”, *Ocean Engineering*, vol. 158, pp. 132–151, 2018.

[14] M. Fousert, J. Vrijling, W. Molenaar, and J. van Kessel, “Floating breakwater, theoretical study of a dynamic wave attenuating system”, in *Coastal Structures 2007: (In 2 Volumes)*, World Scientific, 2009, pp. 339–350.

[15] A. Kamath, M. Alagan Chella, H. Bihs, and Ø. A. Arntsen, “Energy transfer due to shoaling and decomposition of breaking and non-breaking waves over a submerged bar”, *Engineering Applications of Computational Fluid Mechanics*, vol. 11, no. 1, pp. 450–466, 2017.

[16] E. L. Grotle, H. Bihs, and V. Æsøy, “Experimental and numerical investigation of sloshing under roll excitation at shallow liquid depths”, *Ocean Engineering*, vol. 138, pp. 73–85, 2017.

[17] N. Ahmad, H. Bihs, A. Kamath, and Ø. A. Arntsen, “Three-dimensional cfd modeling of wave scour around side-by-side and triangular arrangement of piles with reef3d”, *Procedia Engineering*, vol. 116, pp. 683–690, 2015.

[18] N. Ahmad, H. Bihs, D. Myrhaug, A. Kamath, and Ø. A. Arntsen, “Numerical modeling of breaking wave induced seawall scour”, *Coastal Engineering*, vol. 150, pp. 108–120, 2019.

[19] N. Ahmad, H. Bihs, D. Myrhaug, A. Kamath, and Ø. A. Arntsen, “Numerical modelling of pipeline scour under the combined action of waves and current with free-surface capturing”, *Coastal Engineering*, vol. 148, pp. 19–35, 2019.

[20] H. Bihs, A. Kamath, M. A. Chella, and Ø. A. Arntsen, “Extreme wave generation, breaking, and impact simulations using wave packets in reef3d”, *Journal of Offshore Mechanics and Arctic Engineering*, vol. 141, no. 4, p. 041 802, 2019.

[21] A. Aggarwal, H. Bihs, D. Myrhaug, and M. A. Chella, “Characteristics of breaking irregular wave forces on a monopile”, *Applied Ocean Research*, vol. 90, p. 101 846, 2019.

[22] A. Kamath, H. Bihs, M. A. Chella, and Ø. A. Arntsen, “Cfd simulations of wave propagation and shoaling over a submerged bar”, *Aquatic Procedia*, vol. 4, pp. 308–316, 2015.

[23] M. A. Chella, H. Bihs, and D. Myrhaug, "Characteristics and profile asymmetry properties of waves breaking over an impermeable submerged reef", *Coastal Engineering*, vol. 100, pp. 26–36, 2015.

[24] H. Bihs and A. Kamath, "A combined level set/ghost cell immersed boundary representation for floating body simulations", *International Journal for Numerical Methods in Fluids*, vol. 83, no. 12, pp. 905–916, 2017.

[25] A. Sasikumar, H. Bihs, A. Kamath, O. Musch, and Ø. A. Arntsen, "Numerical investigation of wave kinematics inside berm breakwaters with varying berm geometry using reef3d", in *ASME 2017 36th International Conference on Ocean, Offshore and Arctic Engineering*, American Society of Mechanical Engineers, 2017, V07AT06A035–V07AT06A035.

[26] H. Bihs, A. Kamath, M. A. Chella, A. Aggarwal, and Ø. A. Arntsen, "A new level set numerical wave tank with improved density interpolation for complex wave hydrodynamics", *Computers & Fluids*, vol. 140, pp. 191–208, 2016.

[27] R. Courant, E. Isaacson, and M. Rees, "On the solution of nonlinear hyperbolic differential equations by finite differences", *Communications on Pure and Applied Mathematics*, vol. 5, no. 3, pp. 243–255, 1952.

[28] C. Johnson, *Numerical solution of partial differential equations by the finite element method*. Courier Corporation, 2012.

[29] Y. Morinishi, T. S. Lund, O. V. Vasilyev, and P. Moin, "Fully conservative higher order finite difference schemes for incompressible flow", *Journal of computational physics*, vol. 143, no. 1, pp. 90–124, 1998.

[30] G.-S. Jiang and C.-W. Shu, "Efficient implementation of weighted eno schemes", *Journal of computational physics*, vol. 126, no. 1, pp. 202–228, 1996.

[31] C.-W. Shu, "Essentially non-oscillatory and weighted essentially non-oscillatory schemes for hyperbolic conservation laws", in *Advanced numerical approximation of nonlinear hyperbolic equations*, Springer, 1998, pp. 325–432.

[32] C.-W. Shu and S. Osher, "Efficient implementation of essentially non-oscillatory shock-capturing schemes, ii", in *Upwind and High-Resolution Schemes*, Springer, 1989, pp. 328–374.

[33] A. Harten, B. Engquist, S. Osher, and S. R. Chakravarthy, "Uniformly high order accurate essentially non-oscillatory schemes, iii", in *Upwind and high-resolution schemes*, Springer, 1987, pp. 218–290.

[34] R. Courant, K. Friedrichs, and H. Lewy, "On the partial difference equations of mathematical physics", *IBM journal of Research and Development*, vol. 11, no. 2, pp. 215–234, 1967.

[35] D. A. Wilcox, "Simulation of transition with a two-equation turbulence model", *AIAA journal*, vol. 32, no. 2, pp. 247–255, 1994.

[36] A. J. Chorin, "Numerical solution of the navier-stokes equations", *Mathematics of computation*, vol. 22, no. 104, pp. 745–762, 1968.

[37] D. Naot and W. Rodi, "Calculation of secondary currents in channel flow", *Journal of the Hydraulics Division*, vol. 108, no. 8, pp. 948–968, 1982.

[38] R. D. Falgout, J. E. Jones, and U. M. Yang, "The design and implementation of hypre, a library of parallel high performance preconditioners", in *Numerical solution of partial differential equations on parallel computers*, Springer, 2006, pp. 267–294.

[39] H. A. Van der Vorst, "Bi-cgstab: A fast and smoothly converging variant of bi-cg for the solution of nonsymmetric linear systems", *SIAM Journal on scientific and Statistical Computing*, vol. 13, no. 2, pp. 631–644, 1992.

[40] M. Sussman, P. Smereka, and S. Osher, "A level set approach for computing solutions to incompressible two-phase flow", *Journal of Computational physics*, vol. 114, no. 1, pp. 146–159, 1994.

[41] D. Peng, B. Merriman, S. Osher, H. Zhao, and M. Kang, "A pde-based fast local level set method", *Journal of computational physics*, vol. 155, no. 2, pp. 410–438, 1999.

[42] A. Aggarwal, C. Pákozdi, H. Bihs, D. Myrhaug, and M. Alagan Chella, "Free surface reconstruction for phase accurate irregular wave generation", *Journal of Marine Science and Engineering*, vol. 6, no. 3, p. 105, 2018.

[43] J. Larsen and H. Dancy, "Open boundaries in short wave simulations—a new approach", *Coastal Engineering*, vol. 7, no. 3, pp. 285–297, 1983.

[44] L. H. Holthuijsen, *Waves in oceanic and coastal waters.* Cambridge university press, 2010.

[45] M. Mizuguchi, "Individual wave analysis of irregular wave deformation in the nearshore zone", in *Coastal Engineering 1982*, 1982, pp. 485–504.

[46] K. Iwata and T. Sawaragi, "Wave deformation in the surf zone", *Memoirs of rhe Faculty of Engineering, Nagoya University*, vol. 34, no. 2, pp. 239–283, 1982.

[47] J. D. Fenton, "A fifth-order stokes theory for steady waves", *Journal of waterway, port, coastal, and ocean engineering*, vol. 111, no. 2, pp. 216–234, 1985.

[48] K. d'Angremond, J. W. Van Der Meer, and R. J. De Jong, "Wave transmission at low-crested structures", in *Coastal Engineering 1996*, 1997, pp. 2418–2427.

[49] J. W. Van Der Meer, R. Briganti, B. Wang, and B. Zanuttigh, "Wave transmission at low-crested structures, including oblique wave attack", in *Coastal Engineering Conference*, ASCE American Society of Civil Engineers, vol. 29, 2004, p. 4152.

[50] A. Panizzo and R. Briganti, "Analysis of wave transmission behind low-crested breakwaters using neural networks", *Coastal Engineering*, vol. 54, no. 9, pp. 643–656, 2007.

[51] M. Buccino and M. Calabrese, "Conceptual approach for prediction of wave transmission at low-crested breakwaters", *Journal of waterway, port, coastal, and ocean engineering*, vol. 133, no. 3, pp. 213–224, 2007.

[52] Y. Goda and J. P. Ahrens, "New formulation of wave transmission over and through low-crested structures", in *Coastal Engineering 2008: (In 5 Volumes)*, World Scientific, 2009, pp. 3530–3541.

[53] T. Wamsley, H. Hanson, and N. C. Kraus, "Wave transmission at detached breakwaters for shoreline response modeling", Engineer Research, Development Center Vicksburg MS Coastal, and Hydraulics Lab, Tech. Rep., 2002.

[54] A. C. Biesheuvel, "Effectiveness of floating breakwaters: Wave attenuating floating structures", 2013.

[55] A. Mahmoudi, H. Hakimzadeh, M. J. Ketabdari, N. Cartwright, and M. Vaghefi, "Experimental study on wave transmission and reflection at impermeable submerged breakwaters", *International Journal of Coastal and Offshore Engineering*, vol. 1, no. 3, pp. 19–27, 2017.

[56] L. Cheng, C. Fen, Y. Li, and W. Jiang, "Experimental study on a new type floating breakwater", in *Proceedings of the 7th International Conference on Asian and Pacific Coasts*, 2013, pp. 24–26.

[57] M. Boers, "Simulation of a surf zone with a barred beach; part 1: Wave heights and wave breaking", *Oceanographic Literature Review*, vol. 4, no. 44, p. 292, 1997.

[58] P. D. Hieu and K. Tanimoto, "Verification of a vof-based two-phase flow model for wave breaking and wave–structure interactions", *Ocean engineering*, vol. 33, no. 11-12, pp. 1565–1588, 2006.

[59] A. Kamath, A. Sasikumar, and H. Bihs, "Numerical study of wave interaction with a submerged porous breakwater in combination with a floating breakwater", *Coastal Engineering Proceedings*, vol. 1, no. 36, p. 38, 2018.

Khaled Damdam

A Combined Breakwater System

NTNU
Norwegian University of
Science and Technology